copy 1

A HIGH PERFORMANCE LASER-EXCITED INTERFEROMETER FOR MEASURING ELECTRON DENSITIES

by

Lynn Warren Funk

B.Sc., University of Manitoba, 1965
M.Sc., University of Manitoba, 1968

A Thesis Submitted in Partial Fulfilment
of the Requirements for the Degree of
Doctor of Philosophy
in the Department of
Physics

We accept this thesis as conforming to the
required standard

The University of British Columbia
August, 1971

In presenting this thesis in partial fulfilment of the requirements for an advanced degree at the University of British Columbia, I agree that the Library shall make it freely available for reference and study. I further agree that permission for extensive copying of this thesis for scholarly purposes may be granted by the Head of my Department or by his representatives. It is understood that copying or publication of this thesis for financial gain shall not be allowed without my written permission.

Department of Physics

The University of British Columbia
Vancouver 8, Canada

Date 20 Feb. 1972

ABSTRACT

Significant improvements in several aspects of laser-excited interferometer design have been included in this instrument. The device utilizes plasma-limiting quartz tubes, and a concentric resonator design, to greatly simplify interferometry in the presence of transverse gradients of refractive index, and improve beam overlap.

The techniques of fractional fringe shift interferometry in the time domain are incorporated, and provide order-of-magnitude improvements in sensitivity ($\int N_e d\ell \gtrsim 5 \times 10^{15}$ cm^{-2}) and temporal resolution ($\Delta\tau \sim \pm 25$ nsec.). Electronic circuitry provides a direct, continuous readout of electron density.

Measurements have been made on a Z-pinch discharge which are impossible in any other way, confirming the usefulness of the discharge as a spectroscopic source, and revealing details of the pinch mechanism.

TABLE OF CONTENTS

TABLE OF CONTENTS (cont'd.)

LIST OF FIGURES

LIST OF FIGURES (cont'd.)

LIST OF TABLES

ACKNOWLEDGEMENTS

I would like to express my sincere appreciation to Dr. F.L. Curzon, for his guidance and encouragement during the course of this experiment.

I would like to acknowledge the technical assistance of D.G. Sieberg and J. Aazam-Zanganeh. Special thanks are due to D.M. Camm, a fellow graduate student, who graciously allowed me to draw on his electronics and computing experience. The contribution of T. Matthews, through his work in the data reduction, is gratefully acknowledged. The measurements of current and magnetic field appear in this thesis through the generosity and diligence of J. Pachner.

The financial support of the Atomic Energy Control Board of Canada is gratefully acknowledged.

I. INTRODUCTION

The Z-pinch discharge is formed between two plane electrodes in a discharge vessel with cylindrical geometry. In this configuration, current flows initially in a thin shell on the inner boundary of the discharge vessel. Once a current path is established in this shell, the current, $\underline{j}$, grows until the azimuthal magnetic field, B, associated with it, is sufficiently large that the $\underline{j} \times \underline{B}$ forces acting on the current begin to drive it radially inward. This is the beginning of the collapse phase. The collapse continues until the current sheet has been brought to rest, near, or on the discharge axis. This is termed the "pinch", and it is from this effect that the device gets its name.

The Z-pinch discharge has been the object of considerable scrutiny since it was first introduced as a potential fusion reactor. Some of that interest has been generated by the mechanics of the formation and collapse of the current sheet which gives it its name. But, more significant perhaps, some of the interest has been directed toward using the discharge as a spectroscopic source.

The advantages of the Z-pinch as a spectroscopic source are many. Most important, it is one of the few devices in which large plasmas of high density and temperature can be formed. This makes it useful for laboratory studies of many plasmas of astrophysical interest which are difficult or impossible to study in any other way. Almost as important is the fact that the device is relatively inexpensive, rugged, and produces plasmas with a very high degree of reproducibility. Finally, its dynamics are generally well understood.

Sadly, however, up to this time it has been impossible to utilize the linear pinch discharge as a calibrated spectroscopic source, because no diagnostic techniques existed for the accurate determination of those plasma parameters (i.e. the electron density and temperature) upon which spectroscopic measurements are based.

It was the objective of this research, therefore, to devise a measuring system which would allow determination of electron density to an accuracy sufficient to permit the calibration of the pinch discharge as a spectroscopic source. This objective has been achieved. The starting point from which the desired diagnostic probe was developed is the laser-excited Fabry-Perot interferometer, which will hereafter be referred to as the laser interferometer or just as the interferometer.

The introduction of the plasma into the interferometer changes the optical path length between the resonator mirrors, by reason of the dependence of plasma refractive index on electron density. The resulting changes in the interferometer fringe patterns are used to reveal the electron density. The basic interferometer can be made to have a good high frequency response and so appears suited to diagnostics of pulsed discharges like the Z-pinch in which the electron density is varying rapidly. There are, however, many limitations to be overcome before the interferometer can be made capable of the precision measurements we will demand of it.

These problems and their solutions form the bulk of the thesis. The first problem to be overcome is the inherent instability of conventional interferometers against gradients in electron density normal to the resonator axis. The elimination

of this unsatisfactory feature by reducing the plasma length and improving the resonator geometry forms the basis of Chapter II.

The most important limitation on the sensitivity of the interferometer lies in its inability to resolve changes in the phase of the output signal of less than π. This limitation makes it very difficult to observe slow changes of electron density. In addition the basic interferometer gives no indication of the sign of the change in electron density. The overcoming of these limitations by application of the techniques of fractional fringe shift interferometry in the time domain are described in the first part of Chapter III.

Finally, the output of a conventional Fabry-Perot interferometer requires a good deal of analysis, before the electron density can be extracted from the fringe patterns. The utilization of the fractional fringe shift techniques, however, encourages the use of automatic data analysis. The output of an interferometer incorporating these techniques consists of a burst of high frequency oscillations, in which the effect of the changing electron density appears as a frequency modulation. An electronic circuit has been constructed to perform the necessary frequency demodulation in real-time, providing an output voltage which is at all times directly proportional to the electron density in the resonator.

This, then, is the significant contribution of these investigations. The author has developed a direct-recording high sensitivity, high resolution diagnostic device for the measurement of electron densities. The device retains the high frequency response which is the chief advantage of laser-excited interferometers.

As was outlined earlier, the justification for the work is the calibration of the Z-pinch as a spectroscopic source, and measurements were made on a typical Z-pinch discharge to demonstrate the capabilities of the diagnostic device.

The description of the plasma source is found in Chapter IV, and the outline of the experimental procedures, presentation of data, and a discussion of sources of error is found in Chapter V. An analysis of the results and a discussion of a model for a portion of the collapse phase can be found in Chapter VI. A summary of the important results, and some suggestions for future research are found in Chapter VII.

Two Appendices, dealing with the details of the electronic circuitry, and a third Appendix, estimating the contribution of HeI transitions to the change in refractive index, conclude the thesis.

II The Optical Resonator

II.1 Introduction

The optical resonator used in this experiment is of the Fabry-Perot type. In principle, Mach-Zehnder and Michelson interferometers have somewhat better time resolution. However, the Fabry-Perot interferometer has the great merits of simple construction and easy alignment, and since resolution times better than 10^{-8} sec. are not required, the choice was made to continue the evolution of the Fabry-Perot interferometer developed at this Plasma Physics Laboratory.[1,2]

This chapter will deal with the basic principles governing the operation of such a device, and with some of the drawbacks and difficulties which are encountered when it is used to measure electron densities in a z-pinch.

It will be seen that of the four serious problems enumerated, two are intrinsic to the resonator, while two are associated with the particular experimental arrangement. The responses made to overcome the latter will be discussed in some detail, and the work done to alleviate the former will be presented in Chapter III.

II.2 Conventional Fabry-Perot Design Limitations

The limitations of a conventional Fabry-Perot soon became apparent when it was used to measure electron density in the collapse phase of a Z-pinch.

The schematic of Fig. II-1(a) shows the essential features of an idealized Fabry-Perot interferometer, and illustrates the method used to apply the device to the measurement of electron densities in a time-dependent plasma.

Introduction of the plasma into the resonant cavity alters n, the index of refraction. This, in turn varies the phase difference between the emergent beams (1 and 2 in Fig. II-1), thereby modulating the beam intensity observed by the photomultiplier.

As is well known, the electron density is related to the index of refraction by the relation:

$$n^2 = 1 - \frac{e^2 N_e}{m_e \varepsilon_o \omega^2} \qquad (2.1)$$

where n is the refractive index, e is the electronic charge, m_e is the electronic mass, ε_o is the dielectric permittivity of free space, ω is the frequency of the radiation which is used to probe the plasma (in this case the frequency of the 6328Å transition in neon, 3×10^{15} sec^{-1}), and N_e is the electron density. Equation (2.1) is valid for the values of ω far away from any characteristic frequency of the plasma, including collision frequencies, plasma frequencies or atomic transitions.

Knowledge of the plasma geometry, and of the way in which the electron density varies along the resonator axis, can be combined with the change in output intensity of the resonator to yield the electron density.

Fig. II-1 <u>Idealized Fabry-Perot</u>

(a) conventional plane - plane resonator, showing the effect of transverse gradients in electron density.

(b) cross section of laser beams at point A, showing separation of beams having different numbers of transits (beams 1 and 2).

(c) dependence of transmittance (T) on change of phase, ϕ, for Fabry-Perot interferometer.

M_1, M_2 - laser cavity mirrors

M_2, M_3 - resonator cavity mirrors (both plane in the conventional interferometer.)

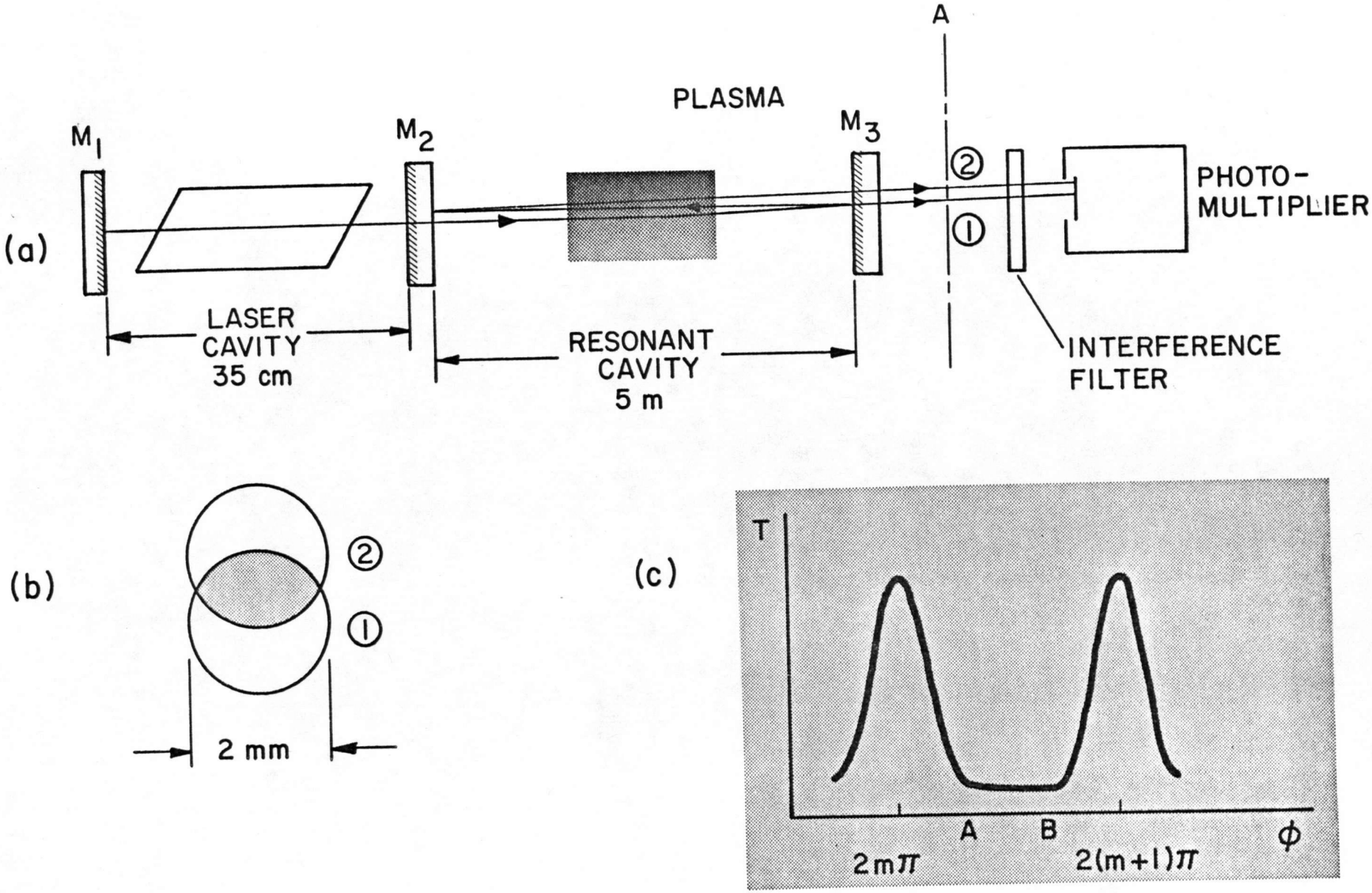
(a)
M1
M2
PLASMA
M3
A
②
①
PHOTO-
MULTIPLIER
LASER
CAVITY
35 cm
RESONANT
CAVITY
5 m
INTERFERENCE
FILTER
(b)
②
①
2 mm
(c)
T
A
B
φ
2mπ
2(m+1)π

In a Z-pinch, N_e is best measured by passing the resonator axis parallel to, but not necessarily coincident with, the pinch axis, because along such directions N_e is constant along the line of sight. This greatly simplifies interpretation of the experimental results. For a further discussion of this feature, see Sec. V-2.

Figure II-1(a) reveals some of the fundamental limitations of the device. These are discussed below:

(a) Extraneous optical path length variation

It is clearly essential that changes in $\int n d\ell$ be due to the changing electron density and not to mechanical movement of the two mirrors M_2 and M_3 with respect to one another. Fortunately, the equipment used in this experiment has a characteristic oscillation period and amplitude which results in an output modulation at approximately 1 KHz (see Fig. II-2). Since the discharge duration is 50 μsec., of which only the first 20 μsec. is of interest, phase changes due to mechanical vibration during the observation period may be ignored.

(b) Beam deflection

It is assumed that the light beams reflected between M_2 and M_3 overlap. When overlap is poor (see Fig. II-1(b)), the calculated electron density is not readily related to the existing density along either beam path. Furthermore, since the two beams can only interfere where they overlap, poor overlap reduces the degree of modulation possible. Complete beam overlap can be assured if the beams are always normally incident on the mirrors. It is clear that the laser beam will be refracted

Fig. II-2 <u>Mechanical Vibrations</u>

This diagram is an enlargement of a photo taken of the output of PM2, showing the effect of mechanical vibrations. Vertical Sensitivity = 250 m V./div.
Sweep Speed = 10 msec./div.

(a) ground level

(b) the laser output with the resonator detuned

(c) the laser output with the resonator tuned

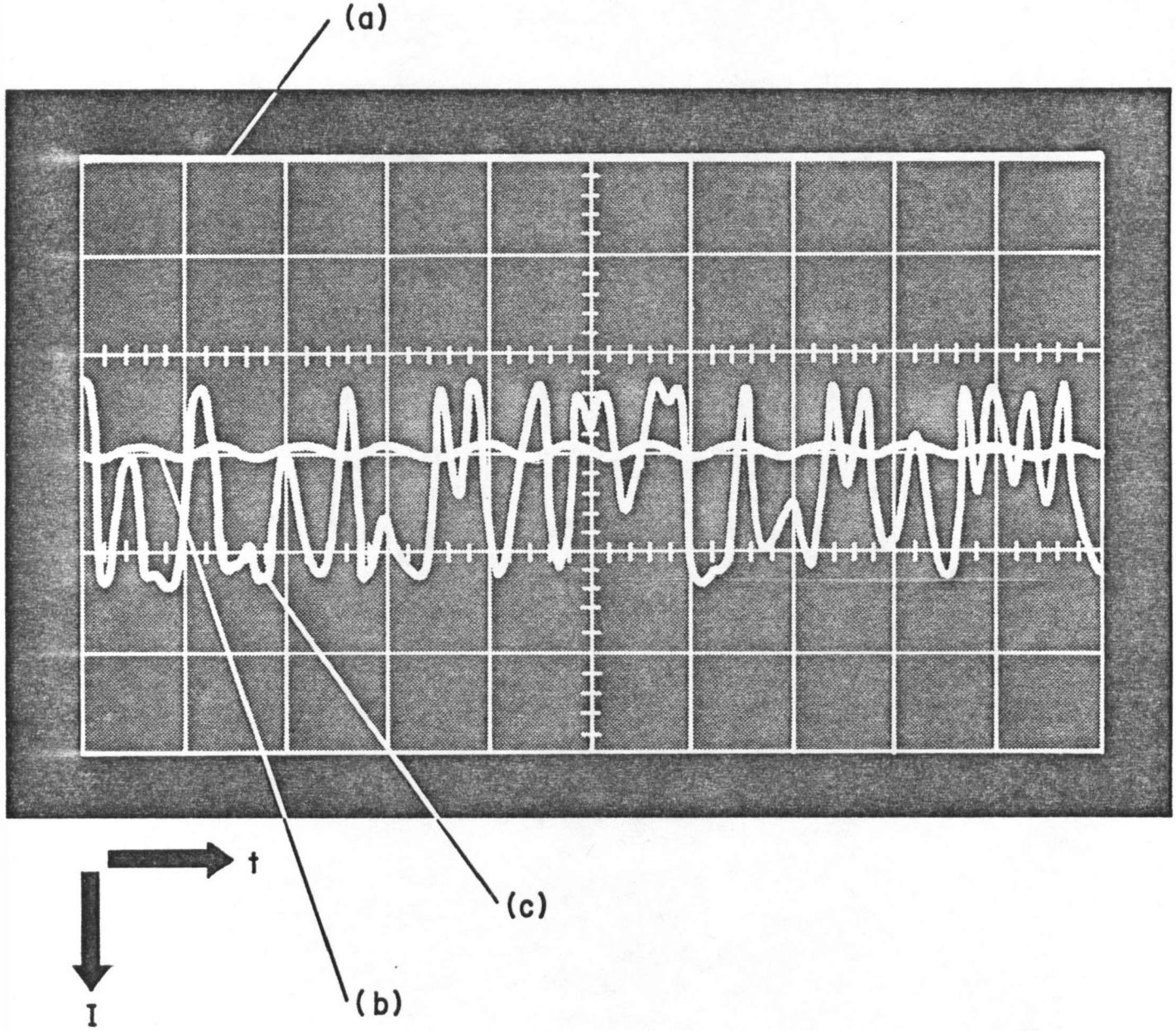
(a)
t
I
(b)
(c)

by gradients in electron density normal to its direction of propagation. If M_2 and M_3 are plane mirrors, the resonator stops working even for a very small beam deflection (for a 5 m. long resonator and a 2 mm. wide beam, the cutoff angle is 0.10 mrad.).

(c) Dependence of transmission on path length

The dependence of the transmission of a simple Fabry-Perot interferometer on optical path length is illustrated in Fig. II-1 (c). This dependence is far from linear. The result is that the phase is only known well at the points of peak transmission. In addition, the transmission is found to be dependent on cavity losses and the rate of change of cavity length [4] [5].

(d) The sign of dN_e/dt

The device illustrated in Fig. II-1(a) provides no indication of the sign of the change in $\int n d\ell$ and hence on the sign of dN_e/dt.

To recapitulate, the four chief limitations of conventional Fabry-Perot design as applied to the problems of electron density measurement are:

a) Structural instability
b) Isntability against transverse dN_e/dr
c) Non-uniform dependence of the transmissivity change on optical path length change.
d) Uncertainty in the sign of dN_e/dt.

These factors are considered in more detail below.

II.3 Structural Instability

Intensity modulations in the resonator output due to mechanical vibrations are at too low a frequency to interfere directly with the measurement of plasma electron density. This fact was established in Sec. II.2(a). However, they make the phase of the system at the start of a measurement uncertain. The effect of this is illustrated in Fig. II-1(c).

Consider the situation which arises if the resonator is located at point A on this diagram. Assuming that the electron density will go from zero to some positive value, $\Delta\int n d\ell$ will be negative, and the intensity will respond immediately to the changing phase. If the resonator were to start from B, however, the electron density and the phase of the system could change substantially before the transmissivity of the resonator would respond.

Since one can use only the peaks in the transmissivity as benchmarks for the phase in calculating the electron density, one is left with an uncertainty of $\pm \pi$ in the phase change required to produce the first observed peak in the transmitted intensity. Since the total phase change observed during a run is 10π or less, this contributes quite a sizeable error to the peak electron density measurement.

The lack of mechanical rigidity has one beneficial side effect. The fluctuations in output intensity due to mechanical vibrations are used to simplify the initial alignment procedure (see Sec. V.1).

II.4 Transverse Gradients in Electron Density

As was outlined earlier, a gradient in electron density normal to the resonator axis is also a gradient in the index of refraction which deflects the beam passing through it.

The magnitude of the deflection depends on the size of the gradient and the path length of the beam in the plasma. Given the geometry of the Z-pinch discharge and the advantages of aligning the interferometer parallel to the axis of symmetry of the discharge, there is little that can be done about the magnitude of the gradient.

However, the length of plasma in the resonator can be shortened by the quartz tubes shown in Fig. II-3.[2] The laser beam passes through the tubes, and as the discharge column collapses, a length of plasma is intercepted between their ends.

The separation of the tubes can be adjusted to limit the amount of refraction so that it can be handled by the mirror system.

A plane-plane mirror configuration, however, can accept only a very small angular deviation of the beam (for our system, 0.1 mrad.). (see Fig. II-4(a)). A plano-spherical mirror system[2] can accommodate much larger angles, but only if the refraction can be localized. The use of the quartz tubes to reduce the plasma length fulfills this condition. If the gradient of electron density is uniform along the ray, and if the angle of refraction is sufficiently small, refraction can be considered to be occurring at a point in the centre of the plasma. We shall refer to this point as the refraction point (denoted in Fig. II-3, as R.P.). If the interferometer exit mirror, M_3, is spherical, with its centre of curvature at this point, any ray

Fig. II-3 Conventional Fabry-Perot showing orientation of Quartz Tubes

M_1, M_2, M_3 - plane mirrors

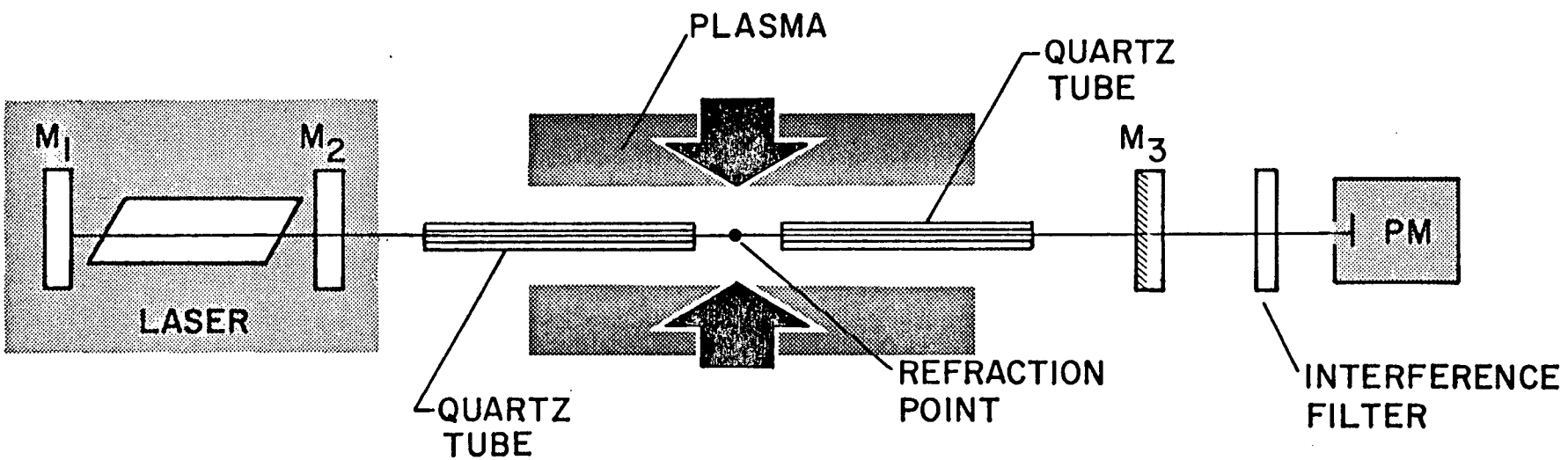
PLASMA
QUARTZ TUBE
M_1
M_2
M_3
PM
LASER
QUARTZ TUBE
REFRACTION POINT
INTERFERENCE FILTER

Fig. II-4 Optical Resonators

(a) Conventional plane-plane mirror configuration, including plasma to show effect of refraction by transverse gradients in electron density. The cross-section of output beams in plane A demonstrates beam overlap.

(b) Plano-spherical mirror configuration. The cross-sectional view shows poor overlap of beams 1 and 2, with poor interference as a result.

(c) Concentric mirror configuration. Correctly aligned, the overlap of beams 1 and 2 should be exact, as shown in cross-section A.

Interference occurs only where beams 1 and 2 overlap.

M_2, M_3 - partially transmitting mirrors.
L - converging lens.

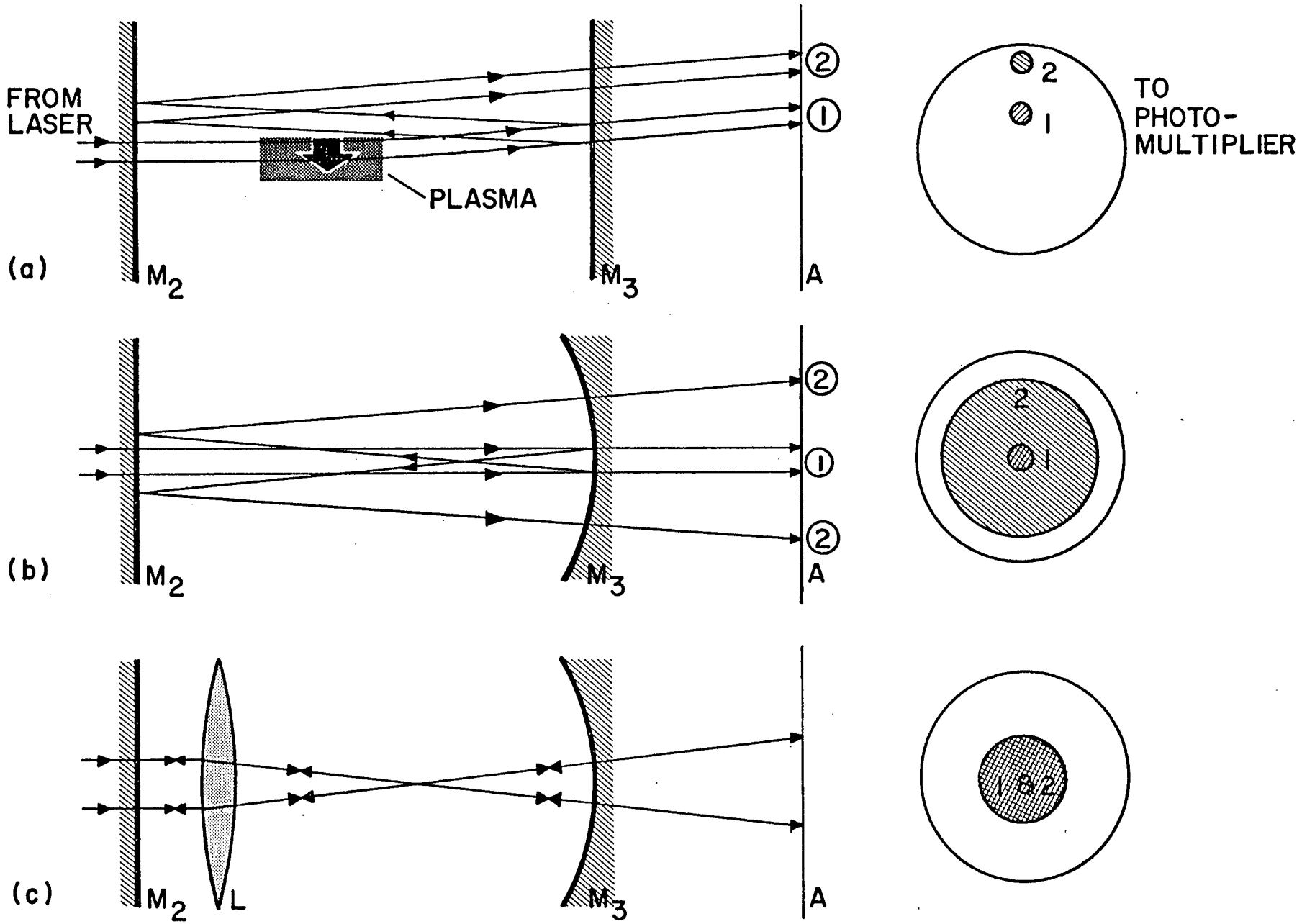
FROM
LASER
PLASMA
(a)
M_2
M_3
A
2
1
TO
PHOTO-
MULTIPLIER
(b)
(c)
L

which can clear the confining quartz tube will be normally incident on the exit mirror.

It now becomes important to insure that the centre of curvature of the exit mirror is located at the refraction point, for if it is not, the plane interferometer entrance mirror (M_2 in Fig. II-3) will accentuate any refractions that occur, since the beam will not return along its ingoing trajectory.

Although the use of a plano-spherical mirror system insures overlap of the emergent beams for larger angles of refraction, the quality of the interference produced is much less. Fig. II-4(b) shows the beam dimensions to be expected with such a resonator. Beam 2 is spread over a much larger area than beam 1, with the result that much of beam 2 is lost. The fluctuations in output intensity are therefore much smaller since this parameter is determined by the intensity of the weaker beam (beam 2).

Further stability can be achieved by making both M_2 and M_3 spherical mirrors with their centres of curvature at the centre of the plasma. M_2 is readily converted to a spherical mirror by mounting a long focal length converging lens in front of it. In this way, any ray which is moving off axis as it approaches M_2 will be bent back towards the axis. This condition could result, as discussed above, from a misalignment of the mirror M_3. The lens is placed with its focal point at the refraction point.

The use of the concentric mirror design has not only reduced the effect of transverse gradients in electron density, but it has also improved the degree of intensity modulation which can be achieved in the output beam. This is illustrated in Fig. II-4(c). In this configuration, good alignment will

result in complete overlap of beams one and two, at maximum possible energy density for each.

The use of quartz tubes, and the conversion to a concentric mirror system has offset the problems associated with transverse gradients in electron density.

The problem of the determination of the sign of dN_e/dt, and of the non-uniform dependence of the change in transmissivity of the resonator on changes of optical path length will be dealt with in the next chapter.

III Fractional Fringe Shift Interferometry

III.1 General Principles

As was outlined in Sec. II.3, attempts to measure directly the phase change produced by variations in electron density by observations of variations in transmitted intensity can be frustrated. This is because the change in transmission for a given change of phase depends on the unknown initial phase. Where the phase change produced by the plasma is many multiples of 2π, the percentage error due to the unknown initial phase is small. In this experiment this method of minimizing the problem is of very limited usefulness.

The reason for this is clear from the discussion of Sec. II.4. To increase the change in phase, the plasma length has to be increased, which increases the refraction of the laser beam. Even with a concentric resonator of the type discussed above, the permissible beam deflection is limited by the dimensions of the quartz tubes through which it must pass and by the dimensions of the mirror. It is important, therefore, to keep the plasma length small, and as a result, the number of 2π changes in phase is also small. We are therefore faced with the problem of measuring small changes in phase with a device which cannot readily resolve changes of phase smaller than 2π.

A similar problem has been overcome by those workers who construct interferograms or holograms of transparent objects[6]. The technique used involves the introduction of a second phase object (which will be defined as the reference object) into the system.

This reference object produces sufficiently large changes in phase to create many interference fringes in a regular pattern over the region where the test object (in this case, the plasma) produces only a few fringes. If an interferogram is taken with both objects in the interferometer the total phase change will be the sum of the phase changes due to each object. As a result, regular fringes produced by the reference object will be distorted. From the distortion, the phase shifts produced by the test object are easily deduced. Thus, changes in phase of $\pi/10$ can be measured with ease.

The problem in this experiment is similar, but the difference is also of interest. In this case, the objective is not the measurement of small changes in phase as a function of position, but rather as a function of time. The "reference object" in this case must be one which produces a regular pattern of interference fringes in time. The interference fringes are, of course, the oscillations of the transmissivity of the optical resonator at the laser wavelength. Therefore, a reference object is required which will produce a regular variation in the optical path length between the mirrors M_2 and M_3 (Fig. II-4 (c)) which constitute the resonator.

The simplest way to create such a reference object is to impose a relative motion on the two mirrors. The easiest way of doing this is to move the exit mirror of the resonator. Various workers[7,13] have mounted their return mirrors (M_3 in this experiment) on loudspeaker cones, on piezo-electric crystals, or on rotating tables. The method in use in this experiment is somewhat different, and it is believed, both neater and more efficient.

The procedure has been to introduce a quartz block into the resonator, and to rotate it about an axis normal to the resonator axis (see Fig. III-1). As the angle of incidence of the laser beam on the face of the quartz block (QB) changes, so too does the optical path length within the resonator. This produces the required rapid oscillations in the resonator transmissivity.

As the plasma (PL in Fig. III-1) enters the resonator, it will change the optical path length in the resonator, and the frequency of the oscillations of output intensity. Knowing the sign of the change in optical path length produced by the rotating quartz block, it is possible to deduce, from the sign of the change in output frequency, the sign of dN_e/dt.

So long as the oscillation frequency of the output due to the rotation of the quartz block exceeds that produced by the changing electron density, there is no ambiguity in assigning changes in fringe spacing (or period) to the influence of the variations in electron density.

Fig. III-1 Concentric Resonator with Reference Object

QB	-	quartz block
$L_{1,2}$	-	converging lenses with focal points at R.P.
R.P.	-	Refraction point
QT	-	Quartz tubes
PL	-	Plasma column
I	-	Interference filter
PM	-	Photomultiplier
PD	-	Photodiode

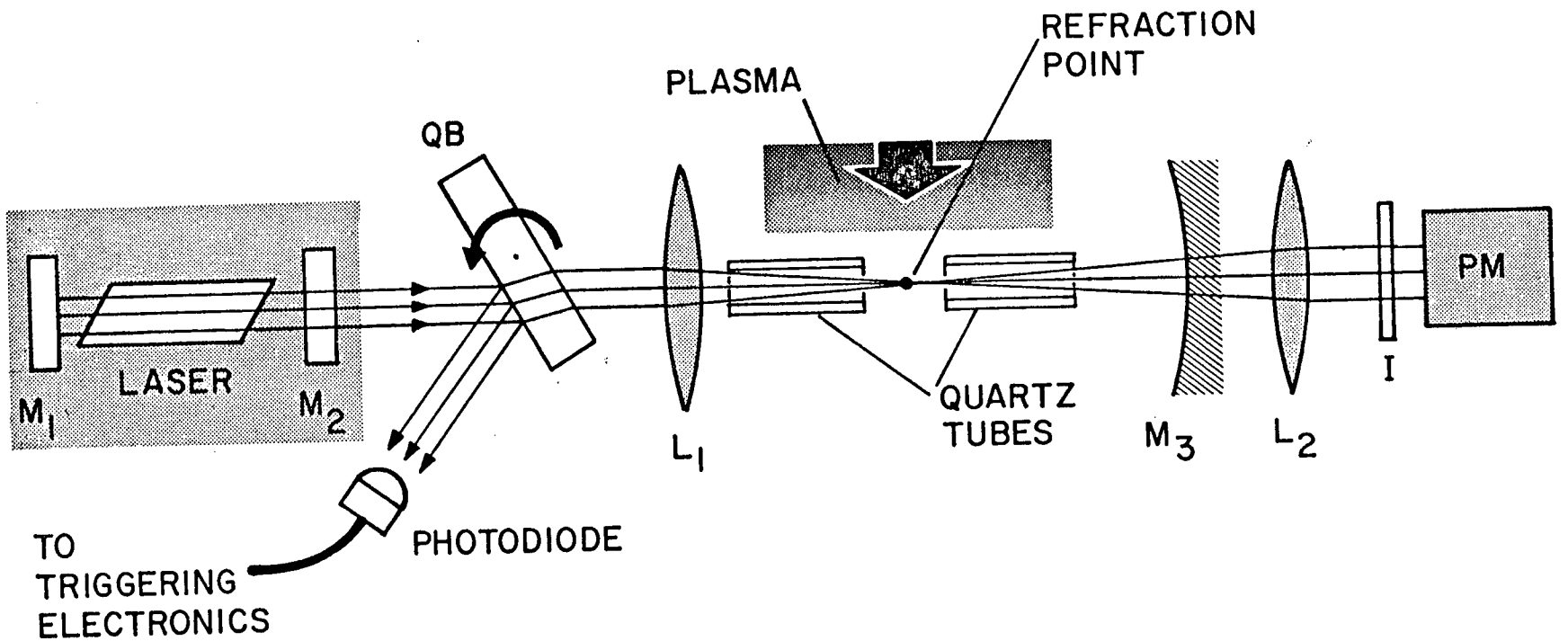
REFRACTION
POINT
PLASMA
QB
PM
LASER
M_1
M_2
L_1
QUARTZ
TUBES
M_3
L_2
I
PHOTODIODE
TO
TRIGGERING
ELECTRONICS

III.2 Characteristics of the Reference Object

In the preceding section we have outlined the techniques of fractional fringe shift interferometry in the time domain. This section will deal with the calculation of the rate of change of optical path length to be expected from the reference object, the rotating quartz block.

The quartz block is mounted in the resonator between the laser exit mirror (M_2) and the converging lens (L_1) which together constitute a spherical mirror (Fig. III-1). Since the resonator axis is horizontal, the axis of rotation of the quartz block has also been made horizontal, to facilitate alignment.

Rotation of the quartz block will result in a vertical displacement of the laser beam (illustrated in Fig. III-1). This does not affect the resonator, however, as the converging lens (L_1) corrects for this displacement. In order to be sure that no horizontal deflection occurs (which would result in the laser beam moving from one radial position to another as it moved through the plasma), the portion of laser light reflected from the front surface of the quartz block (seen striking the photodiode in Fig. III-1) is made to pass through the laser exit spot on M_2 as the block is rotated.

The above discussion assumes that the faces of the quartz block through which the beam passes are accurately plane and parallel. The characteristics of the quartz block used are:

Material:	Fused Quartz
Dimensions:	1.25 cm. x 2.50 cm. x 3.00 cm.
Planarity:	large faces plane to $\lambda/20$
Parallelism:	large faces parallel to 1".

The change in optical path length due to rotation of the quartz block can be easily calculated (see Fig. III-2).

The optical path length (L) between points A_1 and A_2 is given by:

$$L = n_1 A_1 A_2 - n_1 B_1 C_1 + n_2 B_1 B_2 \tag{3.1}$$

where n_1 = refractive index of air

and n_2 = refractive index of fused quartz.

As is standard, let n be the index of refraction of quartz relative to air ($n_1 = 1.000$) which gives:

$$L = A_1 A_2 - B_1 C_1 + n B_1 B_2 \tag{3.1a}$$

where $B_1 B_2 = \dfrac{D}{\cos\beta}$

and $B_1 C_1 = \dfrac{D\cos(\alpha-\beta)}{\cos\beta}$ (see Fig. III-2)

Substituting for $B_1 B_2$ and $B_1 C_1$ into (3.1a), we get:

$$L = A_1 A_2 - \frac{D\cos(\alpha-\beta)}{\cos\beta} + \frac{nD}{\cos\beta} \tag{3.1b}$$

Expanding cos $(\alpha-\beta)$ and differentiating with respect to α leads to the expression:

$$\frac{dL}{d\alpha} = \frac{nD\sin\beta}{\cos^2\beta}\frac{d\beta}{d\alpha} + D\sin\alpha - D\sin\alpha\frac{d\beta}{d\alpha} - \frac{D\sin\beta\cos\alpha}{\cos\beta} - \frac{D\sin\alpha\sin^2\beta}{\cos^2\beta}\frac{d\beta}{d\alpha} \tag{3.2}$$

From Snell's Law, we have:

$$\sin\alpha = n\sin\beta \tag{3.3}$$

which, after some manipulation, yields:

$$\cos\beta = \frac{1}{n}(n^2 - \sin^2\alpha)^{\frac{1}{2}} \tag{3.3a}$$

$$\sin\beta = \frac{1}{n}\sin\alpha \tag{3.3b}$$

Fig. III-2 <u>Quartz Block Ray Diagram</u>

$B_{1,2}$ - Beam entrance and exit points on quartz block faces

α - beam angle of incidence

D - quartz block thickness

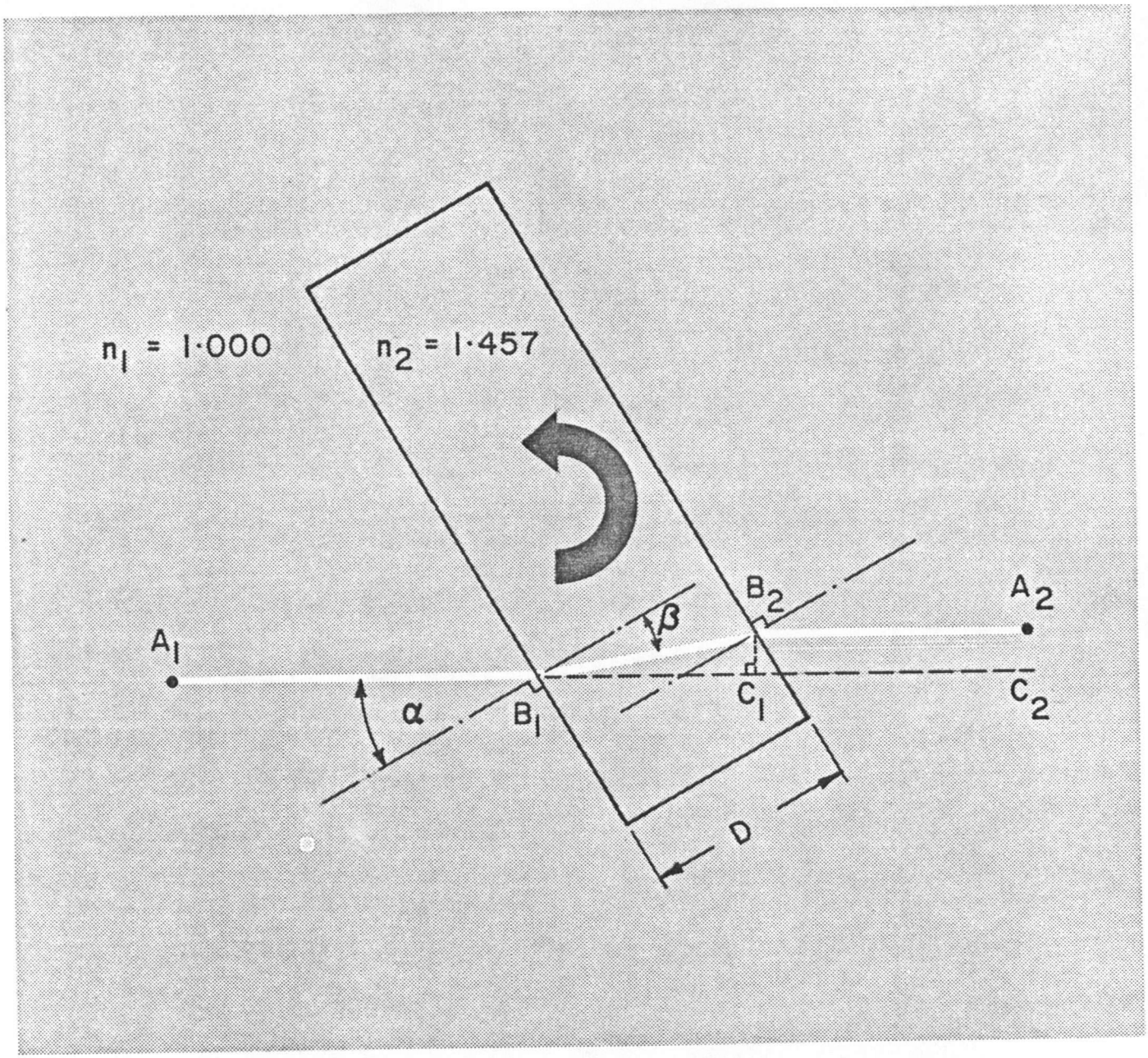
$n_1 = 1{\cdot}000$
$n_2 = 1{\cdot}457$
A_1
A_2
B_1
B_2
C_1
C_2
α
β
D

and after differentiation with respect to α gives:

$$\frac{d\beta}{d\alpha} = \frac{\cos\alpha}{n\cos\beta} \tag{3.3c}$$

Substituting (3.3a) into (3.3c) we get:

$$\frac{d\beta}{d\alpha} = \frac{\cos\alpha}{(n^2 - \sin^2\alpha)^{\frac{1}{2}}} \tag{3.3d}$$

Substitution of (3.3a), (3.3b) and (3.3d) into (3.2) gives:

$$\frac{dL}{d\alpha} = \frac{n^2 D\sin\alpha\cos\alpha}{(n^2 - \sin^2\alpha)^{\frac{3}{2}}} + D\sin\alpha \tag{3.4}$$

Equation (3.4) reduces to:

$$\frac{dL}{d\alpha} = D\sin\alpha\left\{1 - \frac{\cos\alpha}{(n^2 - \sin^2\alpha)^{\frac{1}{2}}}\right\} \tag{3.5}$$

To determine the frequency at which the output of the optical resonator will oscillate, recall that an increase in the length of a double transit of the resonator (i.e. M_2 to M_3 to M_2 in Fig. III-1) of λ will produce a complete cycle of the output. A change of $\lambda/2$ in L is equivalent. The number of cycles dN through which the output oscillates for an angular rotation $d\alpha$ is, therefore:

$$\frac{dN}{d\alpha} = \frac{2}{\lambda}\frac{dL}{d\alpha} = \frac{2D\sin\alpha}{\lambda}\left\{1 - \frac{\cos\alpha}{(n^2 - \sin^2\alpha)^{\frac{1}{2}}}\right\} \tag{3.6}$$

Finally, the oscillation frequency will be, from the chain rule of differentiation:

$$f_o = \frac{2}{\lambda}\frac{dL}{d\alpha}\frac{d\alpha}{dt} \tag{3.7}$$

Since the period of rotation (T) of the quartz block is that observable most easily measured, we substitute:

$$\frac{d\alpha}{dt} = \frac{2\pi}{T} \tag{3.8}$$

into (3.7) to get:

$$f_o = \frac{4\pi D\sin\alpha}{\lambda T}\left\{1 - \frac{\cos\alpha}{(n^2 - \sin^2\alpha)^{\frac{1}{2}}}\right\} \tag{3.9}$$

It should be noted that the distance B_2C_1 in Fig. III-2 can be written as:

$$B_2C_1 \equiv R = \frac{D\sin(\alpha-\beta)}{\cos\beta}$$

$$R = D\sin\alpha - \frac{D\sin\beta\cos\alpha}{\cos\beta} \tag{3.10}$$

Substituting for $\sin\beta$ (eqn. (3.3b)) and $\cos\beta$ (eqn.(3.3a)) we get:

$$R = D\sin\alpha\left\{1 - \frac{\cos\alpha}{(n^2 - \sin^2\alpha)^{\frac{1}{2}}}\right\} \tag{3.11}$$

Comparison with equation (3.9) gives:

$$f_o = \frac{4\pi R}{\lambda T} \tag{3.12}$$

This way of expressing the relation between the observed frequency (f_o) and the quartz block angular position (α) and velocity ($2\pi/T$) is useful because it gives an easy way to calculate the magnitude of the frequency to be expected. With a block thickness (D) of 1.25 cm. it is possible to get a vertical deflection (R) on the order of 0.8 cm. for $\alpha \cong 70^o$. The quartz block is driven by a motor which gives $T = 5 \times 10^{-3}$ sec., yielding an oscillation frequency in excess of 30 MHz.

A similar modulation frequency could be produced by displacing one of the resonator mirrors along the resonator axis at a velocity of 10 m. sec^{-1}. Some of the disadvantages

of such apparently simpler methods of producing reference fringes are discussed in Sec. III.5.

III.3 Fringe Shift Analysis

In Sec. III.1 the principles of fractional fringe shift interferometry in the time domain have been discussed. In Sec. III.2 it was shown that the output of the interferometer which includes a rotating quartz block consists of a train of high frequency oscillations. In view of the rate at which the resonant cavity length is being modulated, these oscillations are nearly sinusoidal[4 5].

Discharge of the Z-pinch during such a burst of oscillations produces a changing electron density in the resonator volume which modulates the oscillation frequency. The temporal development of the electron density can be determined by measuring the change in oscillation frequency.

This is done as follows:
The rate of oscillation of the output of the interferometer (f) is given by:

$$f = \frac{2}{\lambda}\frac{dL}{dt} \tag{3.13}$$

where L is tht total optical length of the resonator, and $\lambda = 6328$ Å. The length L is made up of two parts, the first of which is the "geometric" length L_1, which is the geometric distance between the resonator mirrors, and the additional optical path through the quartz block. If the geometric inter-mirror distance is considered to be constant (see Sec. III.2a), then the only time-dependent length in L_1 is the path through the quartz block.

The second part, L_2, of L is the departure from the "geometric" length due to fluctuations in refractive index of the plasma in the resonator. Let the geometric length of the plasma be Z, which gives:

$$L_2 = (n-1)Z \tag{3.14}$$

and

$$f = \frac{2}{\lambda}\frac{d}{dt}(L_1 + (n-1)Z) \tag{3.15}$$

But $\frac{dL_1}{dt}$ has been calculated in Sec. III.2 and is given by eqn. (3.9) whence:

$$f_o \equiv \frac{2}{\lambda}\frac{dL_1}{dt} = \frac{4\pi D\sin\alpha}{\lambda T}\left\{1 - \frac{\cos\alpha}{(n^2 - \sin^2\alpha)^{\frac{1}{2}}}\right\} \tag{3.16}$$

In addition, Z is fixed by the spacing of the quartz tubes, and (3.15) reduces to:

$$f = f_o + \frac{2Z}{\lambda}\frac{d}{dt}(n-1) \tag{3.17}$$

The dependence of refractive index on electron density is well-known[14] and is given by:

$$n^2 = 1 - \frac{e^2 N_e}{m_e \varepsilon_o \omega^2} \tag{3.18}$$

where n is the refractive index, m_e is the electronic mass, e is the electronic charge, ε_o is the dielectric permittivity of free space, ω is the frequency of the probing radiation, and N_e is the electron density. For $N_e = 10^{18}$ cm^{-3}, a value much higher than any achieved in this experiment, and for $\omega = 2.99 \times 10^{15}$ sec.$^{-1}$, the quantity

$$K = \frac{e^2}{m_e \varepsilon_o \omega^2} = 3.5 \times 10^{-22} \text{ cm.}^3$$

which makes $KN_e = 3.56 \times 10^{-4}$. This quantity is sufficiently small that we may do a binomial expansion of

$$n = (1 - KN_e)^{\frac{1}{2}}$$

and ignore all but the first-order terms.

Thus,

$$n = 1 - \tfrac{1}{2}KN_e \tag{3.19}$$

and

$$\frac{d}{dt}(n-1) = -\tfrac{1}{2}K\frac{dN_e}{dt} \tag{3.20}$$

Substitution of (3.20) into (3.17) gives:

$$f = f_o + \frac{2z}{\lambda}\left(\frac{-K}{2}\right)\frac{dN_e}{dt} \tag{3.21}$$

and, solving for $\frac{dN_e}{dt}$, we get:

$$\frac{dN_e}{dt} = (f_o - f)\frac{\lambda}{KZ} \tag{3.21a}$$

Let $C = \lambda/K = 17.62 \times 10^{16}$ cm.$^{-2}$. Then,

$$\frac{dN_e}{dt} = \frac{C}{Z}(f_o - f) \tag{3.21b}$$

Integrating (3.21b) with respect to time we get:

$$N_e(t) = \frac{C}{Z}\int_o^t (f_o - f)\,d\tau + C_o \tag{3.22}$$

which can be stated as: the instantaneous value of the electron density is proportional to the total phase discrepancy between the perceived oscillation and that which could be expected in the absence of a plasma. The constant C_o is set equal to zero by setting the origin of time at the instant when the voltage is applied to the discharge tube. The electron density at $t = o$ is zero.

III.4 The Integrating Frequency Modulation Detector

Equation (3.22) can be rewritten as:

$$N_e(t) = \frac{C}{Z}\int_o^t f_o(\tau)\,d\tau - \frac{C}{Z}\int_o^t f(\tau)\,d\tau \qquad (3.23)$$

The electron density can be computed if it is possible to make a continuous comparison of the phase of the observed signal with the phase of the signal due to the reference object alone. Since these two signals are not simultaneously available from the same resonator, it was decided to construct a circuit to perform integration of $f(\tau)$, and to then manufacture the integral of $f_o(\tau)$ electronically, assuming $f_o(\tau)$ to be constant.

The electronic device constructed to perform this function is described in detail in Appendix I. A functional block diagram appears in Fig. III-3. The input signal is the high-frequency, quasi-sinusoidal oscillation denoted by $f(\tau)$ in (3.23). This signal is amplified and an identical signal of opposite phase is generated. These two signals are used to trigger separate bistable multivibrators or "flip-flops". These flip-flops are turned "ON" by a positive-going zero-crossing in the input voltage, and are turned "OFF" by the next positive-going zero-crossing. Thus the two flip-flops are oscillating at half the frequency of the input signal, and their outputs differ in phase by $\pi/4$. The signal conditioning process is graphically illustrated in Fig. III-4.

Each flip-flop has two antiphase outputs. The four signals thus available are used to trigger four separate monostable multi-vibrations, or "one-shots". The reason for this choice of logic circuitry lies in the fact that only the amplifiers are required to function at the full input frequency; all other components need work at only half the input

Fig. III-3 Integrating Frequency Modulation Detector.

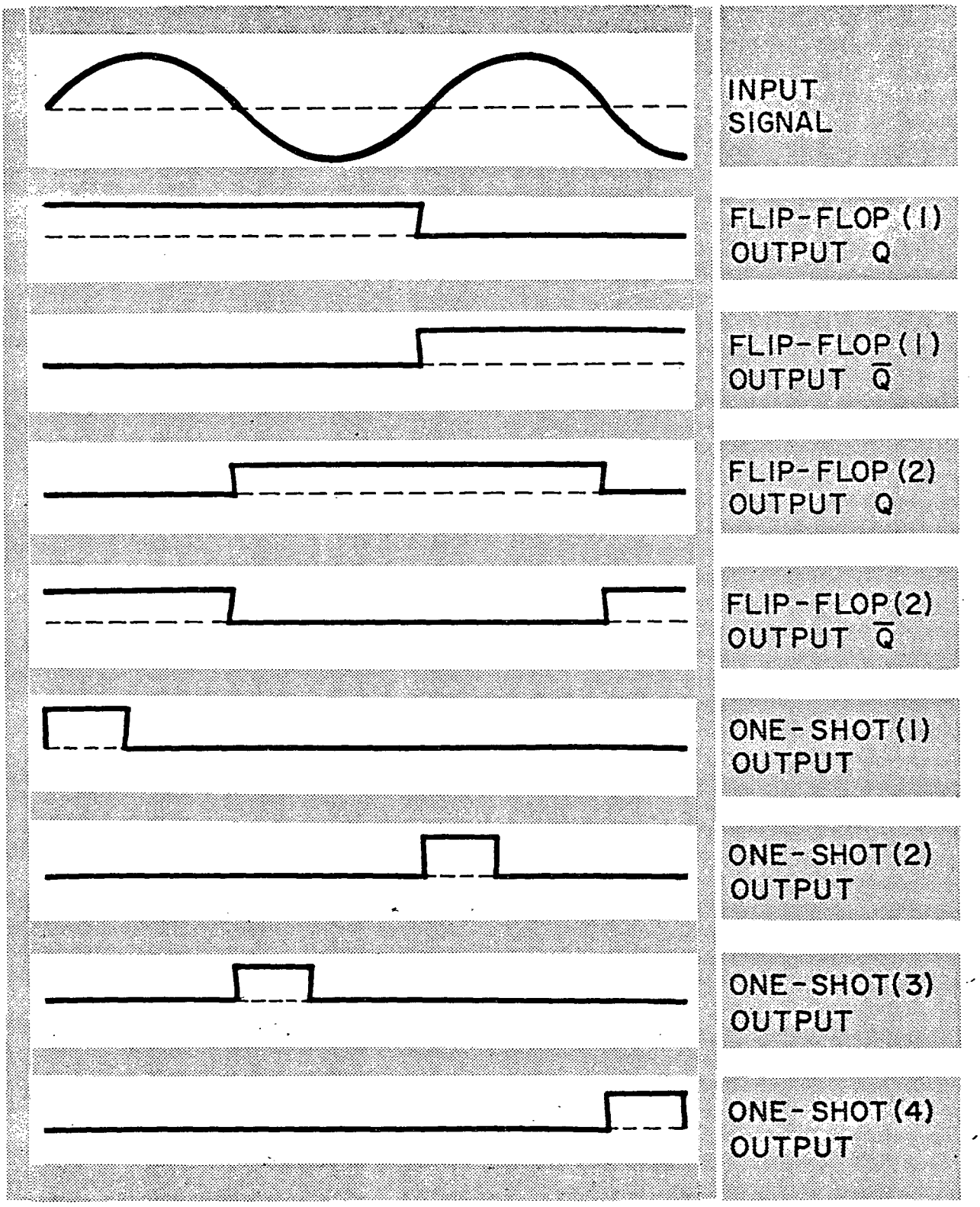
INPUT SIGNAL
FLIP-FLOP (1) OUTPUT Q
FLIP-FLOP (1) OUTPUT $\overline{Q}$
FLIP-FLOP (2) OUTPUT Q
FLIP-FLOP (2) OUTPUT $\overline{Q}$
ONE-SHOT (1) OUTPUT
ONE-SHOT (2) OUTPUT
ONE-SHOT (3) OUTPUT
ONE-SHOT (4) OUTPUT

Fig. III-4 Signal Conditioning

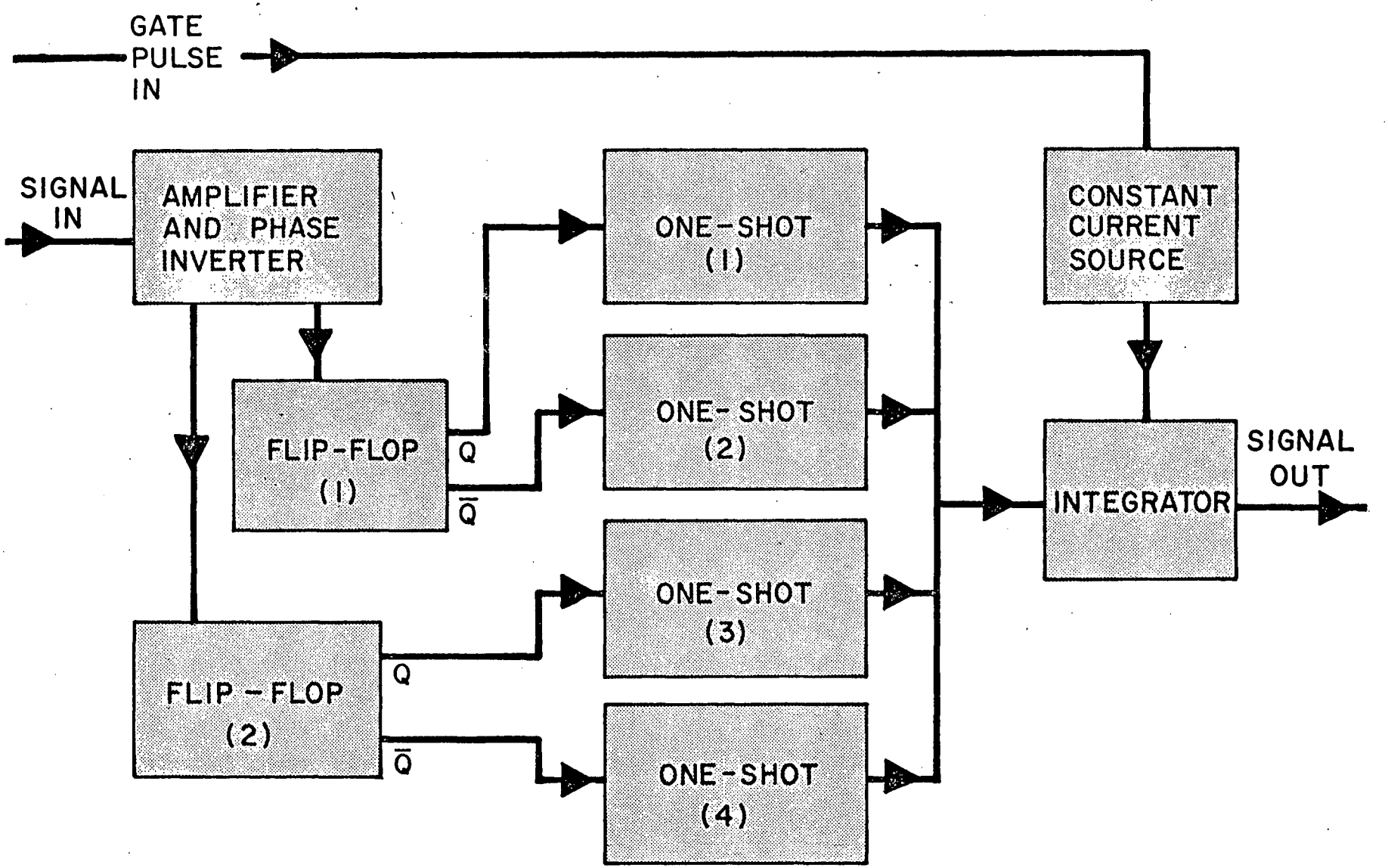
GATE
PULSE
IN
SIGNAL
IN
AMPLIFIER
AND PHASE
INVERTER
FLIP-FLOP
(1)
Q
$\bar{Q}$
FLIP-FLOP
(2)
Q
$\bar{Q}$
ONE-SHOT
(1)
ONE-SHOT
(2)
ONE-SHOT
(3)
ONE-SHOT
(4)
CONSTANT
CURRENT
SOURCE
INTEGRATOR
SIGNAL
OUT

frequency. The system therefore can handle high frequency data using relatively low-frequency components. The outputs of the four one-shots are found to be independent of triggering rate up to 1.8×10^7 pulses per second. This corresponds to an input frequency of 36 MHz., much higher than any used in practice. The one-shot outputs are inverted and fed into the integrator. It should be noted that one of the four one-shots fires for each zero-crossing of the input signal.

The integrator design is the creation of D.M. Camm, a fellow graduate student. The principle behind the design is that each one-shot pulse can be used to draw the same quantity of charge from a charged capacitor. Thus, if the input frequency is constant, the current being drawn from the capacitor will be constant. If, at the same time, the same constant current is being fed onto the capacitor from another source, the voltage on the capacitor will be constant.

Should the input frequency (f) decrease, the capacitor will begin to accumulate charge. If f increases, the capacitor will begin to lose charge. The charge on the capacitor will continue to change as long as f differs from that value which is required to balance the current input from the constant current source. If this frequency is defined as the base frequency (f_b), then it is clear that the current flowing onto the capacitor will be proportional to the difference, $f_b - f$. Further, the change of voltage across the capacitor over a time interval Δt will be proportional to the total change in phase between f_b and f during the time interval Δt.

The electronic device performs the integration:

$$V(t_2) - V(t_1) \equiv \Delta v = C_1 \int_{t_1}^{t_2} (f_b - f)\, d\tau \qquad (3.24)$$

Equation (3.24) is identical to equation (3.22), except for the substitution of f_b for f_o. The value of f_b, determined by the magnitude of the constant current fed onto the integrating capacitor, is time-independent. The value of f_o, determined by the angular position and frequency of rotation of the quartz block is a time-dependent quantity. The value of $N_e(t)$ can be calculated from equations (3.22) and (3.24) as follows:

From equation (3.24):

$$-\int_o^t f(\tau)\,d\tau = \frac{\Delta v(t)}{C_1} - \int_o^t (f_b(\tau)\,d\tau \tag{3.25}$$

which, on substitution into (3.22), yields:

$$N_e(t) = \frac{\Delta V(t)C}{C_1 Z} + \frac{C}{Z}\int_o^t (f_o(\tau) - f_b(\tau))\,d\tau \tag{3.26}$$

Thus, the electron density can be calculated exactly from the change in voltage in the case where f_b has been adjusted to be equal to f_o.

Since the second term on the right hand side of (3.26) is time dependent, it is necessary to show that it can be made small, and that it can be approximated.

$$\text{Let } \phi(t) = \int_o^t (f_o(\tau) - f_b(\tau))\,d\tau \tag{3.27}$$

The base frequency f_b is constant. Let it be assumed that f_b is set, so that

$$f_o(0) = f_b$$

$$\text{Then, } f_o(\tau) = f_b + \left[\frac{d}{d\alpha}(f_o(0))\right].\ \Delta\alpha$$

$$= f_b + \frac{2\pi\tau}{T}\,\frac{df_o(0)}{d\alpha} \tag{3.28}$$

Substituting (3.28) into (3.27), we get:

$$\phi(t) = \int_0^t \frac{df_o(0)}{d\alpha} \frac{2\pi\tau}{T} d\tau = \frac{df_o(0)}{d\alpha} \frac{\pi t^2}{T} \tag{3.29}$$

The quantity $\phi(t)$ is the number of complete cycles of f_o, which occur between $t = 0$ and $t = t$, which are not compensated for by f_b. The number of uncompensated current pulses drawn from the integrating capacitor is therefore $2\phi(t)$ in the same time interval. These uncompensated pulses are distributed uniformly over the time interval, and if $N_e(\tau) \equiv 0$, the signal will be a smoothly varying voltage which starts at $V_1(0)$ and which has:

$$V_1(\tau) = V_1(0) + C_1\phi(\tau) \tag{3.30}$$

as its final value. The only thing which remains to be done is to show that the signal described by (3.30) varies slowly, compared to the fluctuations associated with variations of the electron density in the discharge.

Differentiating equation (3.9) with respect to α, we get:

$$\frac{df_o}{d\alpha} = \frac{4\pi D}{\lambda T} \left\{\cos\alpha \left[1 - \frac{\cos\alpha}{(n^2 - \sin^2\alpha)^{\frac{1}{2}}}\right] + \sin\alpha \left[\frac{n^2 - 1}{(n^2 - \sin^2\alpha)^{\frac{3}{2}}}\right]\right\} \tag{3.31}$$

The function $\phi(t)$ can now be evaluated, using typical experimental values for T ($T = 6$ msec.) and α ($40^\circ < \alpha < 75^\circ$). The value of t is established by the time over which the electron density is to be observed, and this is 20 μsec. for this experiment.

The values of $\phi(t)$ and the change in f_o as a function of α have been plotted in Fig. III-5. Notice that the total number of uncompensated oscillations observed over the viewing interval is never more than nine for values of α which are of experimental interest. This number is of the same order as the number of fringes to be expected from the changing electron density, but the latter will occur in a time interval one to two orders of magnitude smaller. The fluctuations in integrator voltage due to changing electron density are therefore readily distinguishable from the slowly and constantly varying baseline due to the time dependence of f_o.

The experimental results bear out the conclusions of these theoretical considerations. Figure III-6 is an enlargement of a typical oscilloscope trace. The upper waveform is the discharge current waveform, and the lower is the voltage output of the Integrating Frequency Modulation Detector. In this case, the assumption has been made that the electron density is zero at the point of observation during the first few microseconds of the discharge. The curvature of the voltage waveform is therefore entirely due to the fluctuations in the second term of the right-hand side of equation (3.26). This curve has been extrapolated, and the electron density is given by the vertical separation of the observed waveform and the extrapolated baseline.

It is clear that the integrating circuit cannot be left on constantly, as $f_b - f_o >> 0$, except when α, the angle of incidence of the laser beam on the quartz block, is close to the value required for making measurements. For this reason, it is convenient to switch on the constant current source just before the discharge is started. The details of how this is done are discussed in Sec. V.3.

Fig. III-5 <u>Phase Discrepancy</u>

Plot of $\phi(t)$ as a function of the angle of incidence (α) of the laser beam on the quartz block, showing the relation to the change in the oscillation rate due to the quartz block (Δf_o) during the course of one 20 μsec. observation.

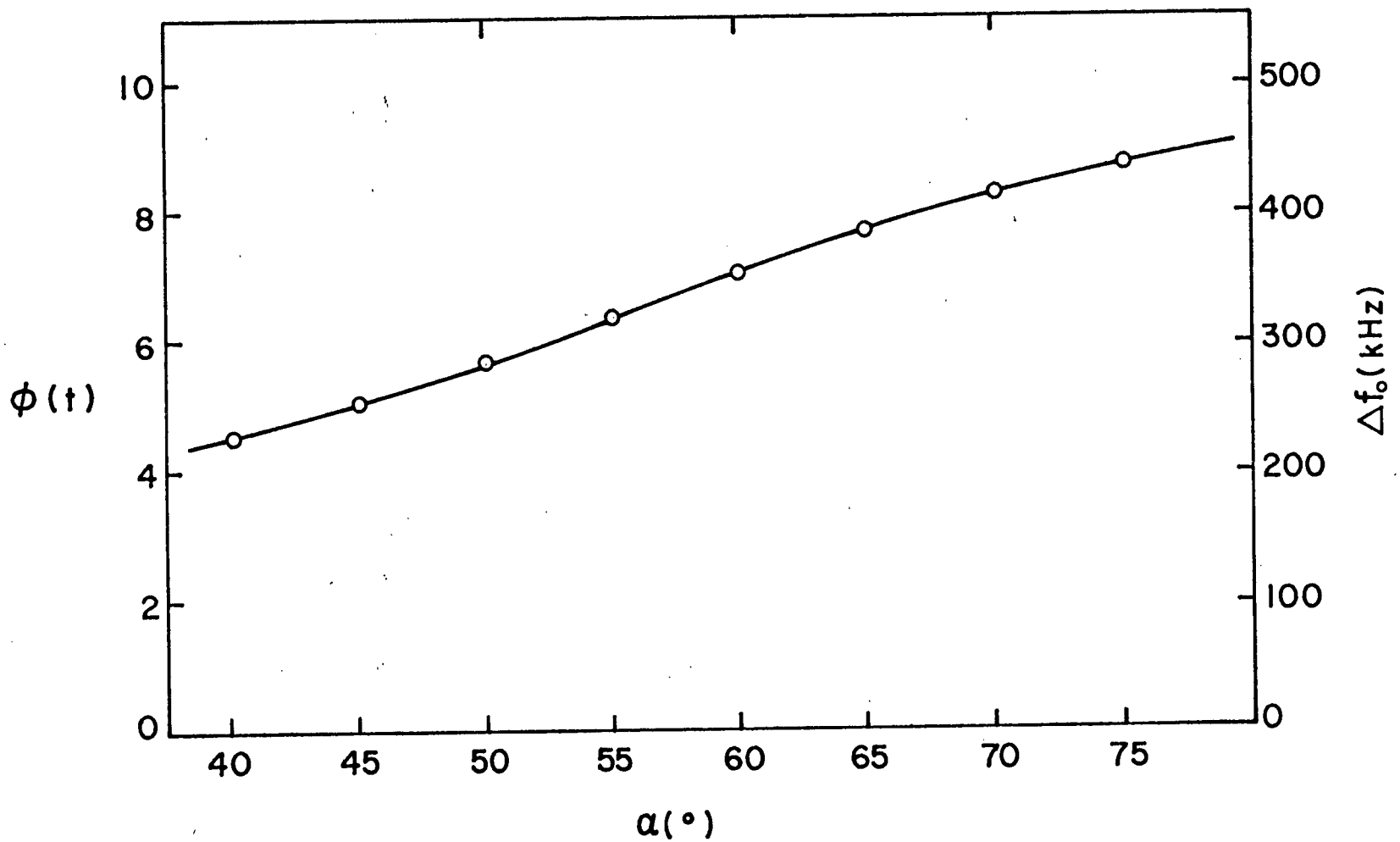
10
8
6
4
2
0
φ(t)
500
400
300
200
100
0
Δf₀(kHz)
40
45
50
55
60
65
70
75
α(°)

Fig. III-6 Typical Oscilloscope Trace

This figure is an enlargement of a typical oscilloscope trace. The upper waveform is the discharge current and the lower, the output voltage of the Integrating Frequency Modulation Detector.

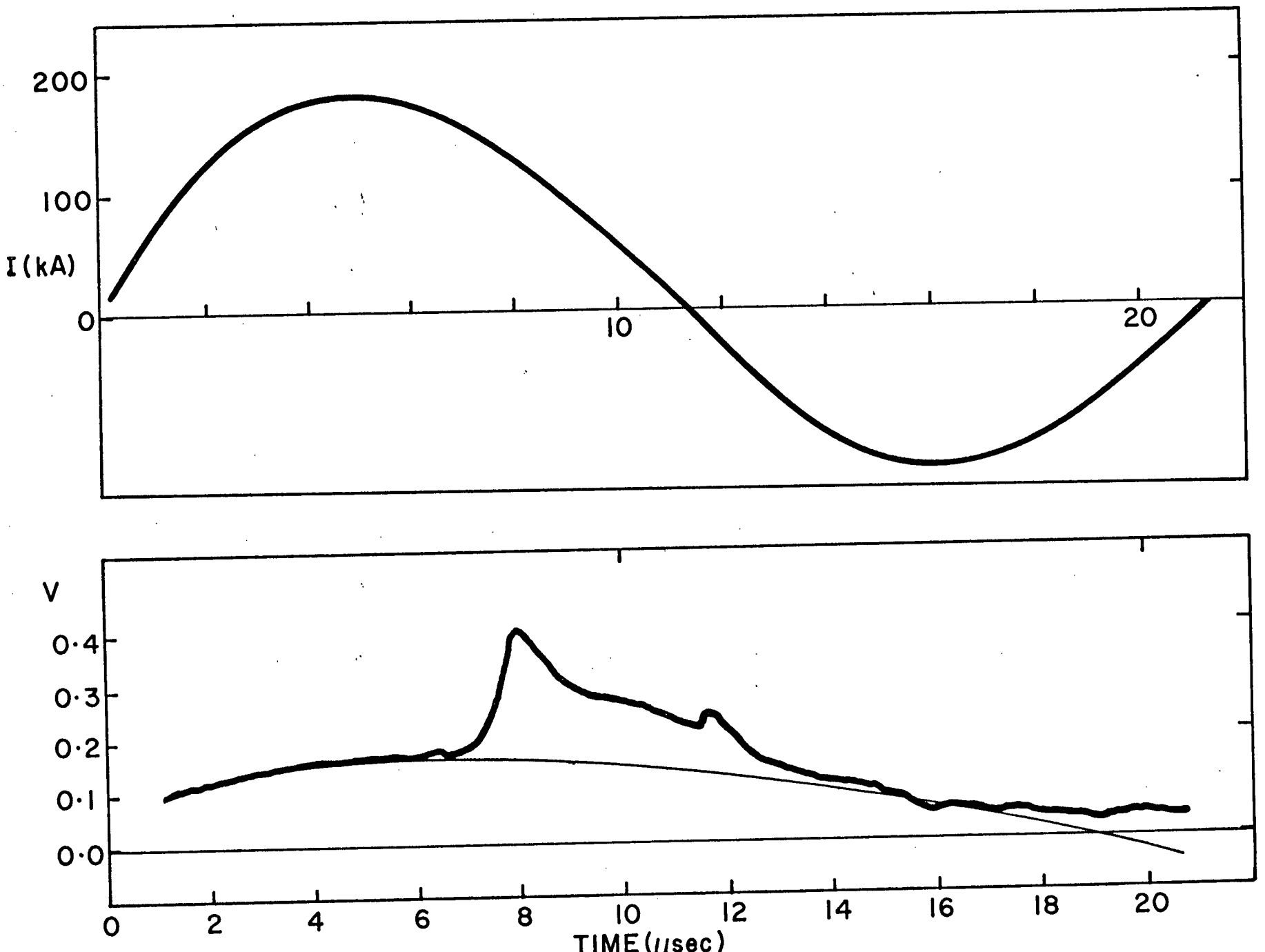
200
100
I (kA)
0
10
20
V
0·4
0·3
0·2
0·1
0·0
0
2
4
6
8
10
12
14
16
18
20
TIME (μsec)

III.5 Other Systems of Fractional Fringe Shift Interferometry

In comparing the rotating quartz block as a reference object with the other techniques which have been reported, the following will be used as criteria:

1) The degree to which good beam overlap can be maintained during the course of the measurement. (For a discussion of beam overlap, see Sec. II.2).

2) The maximum frequency reported for the system.

The first system to be considered is that reported by Baker and co-workers[7]. In this system (see Fig. III-7(a)) the resonator end mirror is plane, and mounted so that it can be rotated.

It is immediately obvious that beam overlap in this device will be sufficient to produce good interference and good fringe amplitude over only a very small range of angular positions. If we use as a criterion of good beam overlap, that the area in which the beams overlap is 1/3 of the cross-sectional area of one beam, then such a system has good beam overlap for only that time interval when the beam centres are displaced by one radius or less. For a 1 m. long resonator and a 2 mm. diameter beam, this condition of good beam overlap will exist over only 1 mrad. of the cycle. The quartz block system as outlined above will achieve good beam overlap over nearly π radians, although the measurement window is usually only about 250 mrad. ($45^{\circ} > \alpha > 60^{\circ}$). Furthermore, the system of Baker, et al, is far more susceptible to vibrations, inasmuch as it involves direct movement of the mirror. Once again, if the normal to the mirror face diverges from the resonator axis at an angle in excess of 1 mrad., beam overlap is poor. Since the mirror itself is being moved, it is difficult to see how such vibrations can be suppressed.

Fig. III-7 Moving Mirror Reference Objects

(a)

PM	-	photodetector
M_1, M_2	-	laser cavity mirrors
R.M.	-	rotating plane mirror

(b)

ID	-	Infrared detector
M_1, M_2	-	laser cavity mirrors
M_3	-	corner mirror
M_4	-	plane mirror
A	-	rotatable table

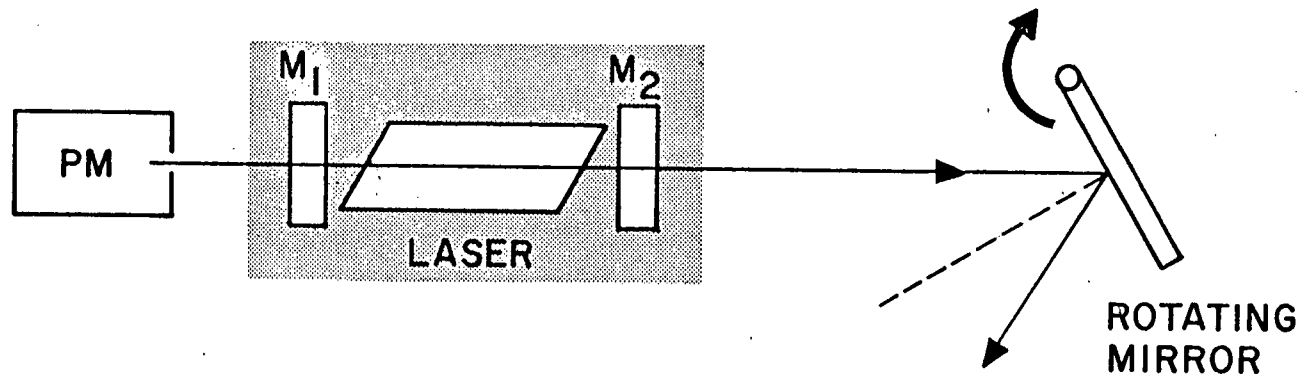

(a)

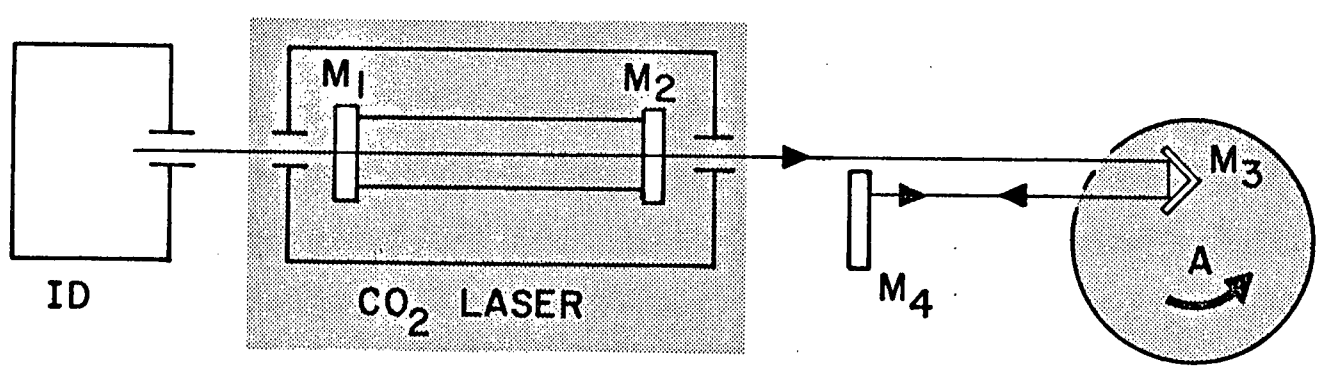

(b)

The frequency of oscillation achieved in this system is only 1 MHz. The low oscillation frequency is due to the detection technique, but even with improvements in this area, the changes of optical path length are taking place in air rather than in quartz.

Another system is that which has the interferometer end mirror (M_3 in Fig. II-3) mounted on a loudspeaker cone[10 11]. Since this system moves the mirror in a straight line, it ought to be feasible to maintain beam overlap for an indefinite period. However, the fact that the mirror is being rapidly moved must cause vibrations and if these vibrations cause rotation of the normal to the mirror by as little as 1 mrad. (for the same conditions as in the previous system), beam overlap will be poor. Such problems were reported.

The frequency reported for this system when used as a plasma diagnostic tool[11] was 90 KHz. This was achieved at a speaker driving frequency of 50 Hz. and a mirror displacement of approximately 1 mm. It can be used therefore on very tenuous or very slowly varying plasmas. Frequencies of up to 5 MHz. have been reported[10 15] but in these cases the total mirror displacement was much less than λ, the wavelength of the laser radiation. Such systems no longer correspond to the rotating quartz block system, and further comparison is pointless.

Similar considerations may be applied to the systems which mount the mirror on a piezo-electric crystal[9 12 13]. The maximum fringing rate reported is orders of magnitude less than that achieved with the rotating quartz block.

The system which comes closest to equalling the performance of the rotating quartz block is the rotating corner mirror of Herold and Jahoda[9]. It is illustrated in Fig. III-7(b).

This system has excellent beam overlap stability, both to rotation of the table (A) and to vibration. In addition, the frequencies which could be achieved with such a device are at least as good as those achieved with a rotating quartz block.

The chief drawback of the system is that it requires a large, carefully balanced table which can be spun at relatively high speeds. In this respect, the quartz block system is superior because of its mechanical simplicity.

A variant on the fractional fringe technique has been devised[4,26], by which both the sign and magnitude of $^{dNe}/dt$ can be determined. The method involves comparison of two fringe patterns produced by beams with a known phase difference. A 1/8 - wave plate is inserted into the interferometer with the plane of polarization of the laser beam (linearly polarized) bisecting the angle between the fast and slow axes of the plate. In this way, two beams of equal intensity, orthogonal polarization and $\pi/2$ phase difference are produced. The interference fringes produced for each polarization are measured by photomultipliers behind suitably oriented polarizers. The disadvantage of this configuration lies in the duplication of detection equipment and the data reduction which must be done to obtain profiles of N_e from the fringe patterns. For these reasons, it is felt that rotating block technique is to be preferred.

IV The Z-Pinch

IV.1 General Description

The Z-pinch discharge under study in this experiment is of conventional design[1], with minor modifications to accommodate the interferometer (see Fig. IV-1). The specifications of the components can be found in Table I.

The brass electrodes (A) have been provided with 3/8" wide slots (I), cut along a diameter of the electrode to within 1/16" of the circumference, to permit insertion of the quartz tubes (H), and to allow these tubes to be moved from one radial position to another[2]. In addition, the quartz tube mountings have been modified to allow adjustment in both radial and axial directions without opening the vacuum system.

The vacuum feedthroughs for adjusting the quartz tubes are shown in Fig. IV-2. Notice the square slots cut into the centres of the brass inserts to accommodate the mechanical connection to the quartz tube mounts. This mechanical connection is achieved using flexible steel cable, of the type used in speedometers.

The radial adjustment of the quartz tubes is accomplished by means of the rack and pinion arrangement shown in Fig. IV-3. The end of the drive cable is inserted directly into the centre of the gear (A in Fig. IV-3). Rotation of the externally accessible part of the mechanical feedthrough (Fig. IV-2, A) causes the gear to move along the rack, and the quartz tube to move along a radius.

Fig. IV-1 The Z-Pinch Discharge Schematic

A. Electrodes

B. Pyrex Discharge Tube Walls

C. High Voltage Power Supply

D. Main Capacitor Bank

E. Main Spark Gap Switch

F. Quartz Envelope of Ultraviolet Source

G. Return Conductor (Brass Gauze)

H. Quartz Tubes

I. Diametral Slot

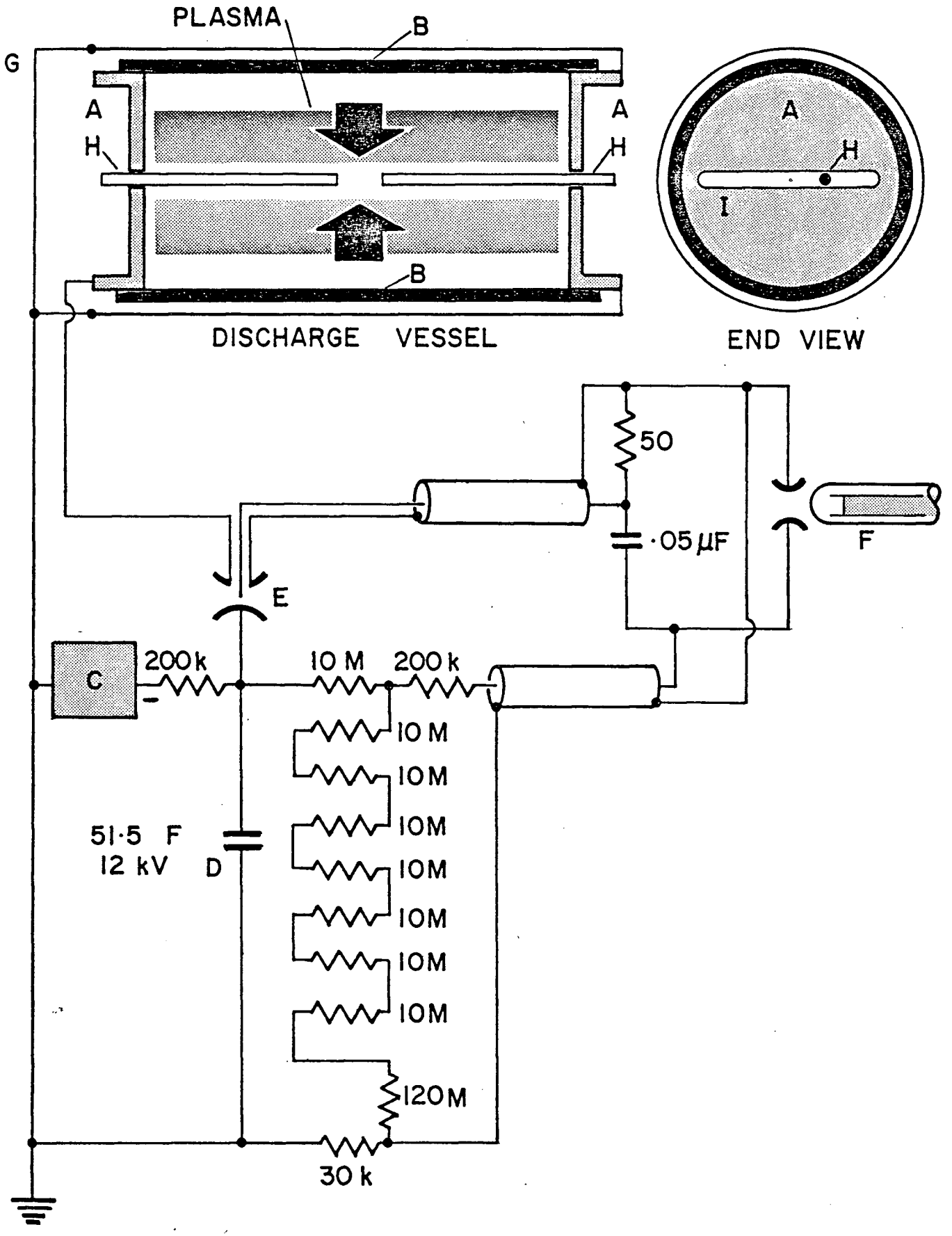
PLASMA
B
G
A
H
A
H
B
DISCHARGE VESSEL
A
H
I
END VIEW
50
·05 μF
F
E
C
200k
10 M
200 k
10 M
10M
10M
10M
10M
10M
10M
51·5 F
12 kV
D
120M
30 k

Table I - Z-Pinch Components

Discharge Tube

Material:	Pyrex
Length:	76.2 cm.
Inner Diameter:	15.0 cm.
Outer Diameter:	17.0 cm.
Interelectrode Length:	61.6 cm.

Vacuum System

Mechanical Pump:	Cenco - HYVAC 14
Diffusion Pump:	Oil - Type 17 Balzer
Vacuum Gauges:	2 Vacustat McLoed 1 at 0-1 Torr. 1 at 0-10 Torr. CVC - Pirani Type GP-110
Base Pressure:	1 μHg.
Leak Rate:	5 μHg./min.

Electrical

Power Supply:	Sorenson Model 1020-30 (0-20 kV; 0-30 mA.)
Capacitors:	5 NRG Type 203 Total capacity 51.5 μF.
Leads:	1/16" x 10 cm. x 1.3 m. (copper)
Electrodes:	Brass
Return Conductor:	Brass Gauze
Voltage Measurement:	Simpson microammeter in series with precision 500 MΩ resistor.

Fig. IV-2 Vacuum Feedthroughs in End Windows

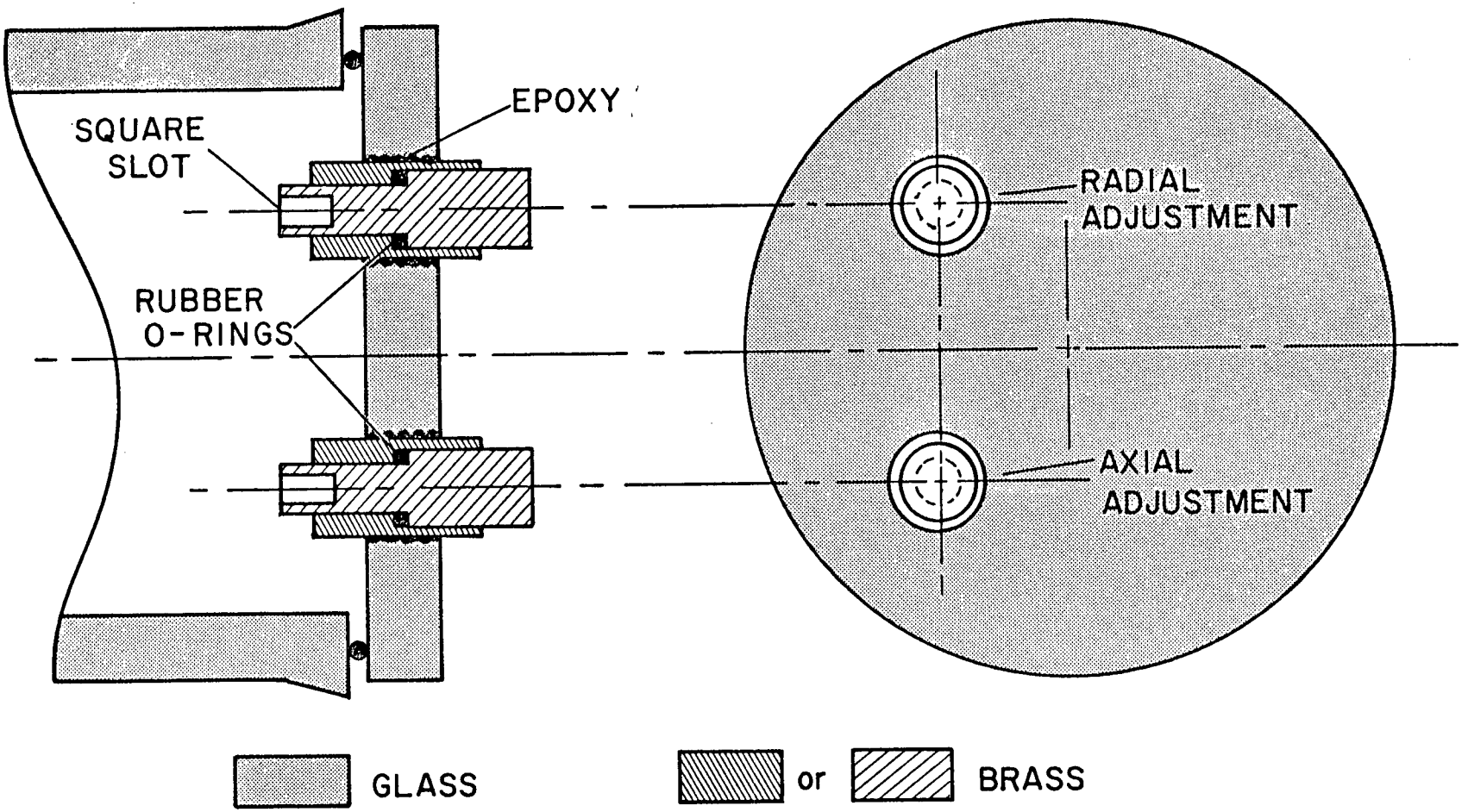
EPOXY
SQUARE SLOT
RUBBER O-RINGS
RADIAL ADJUSTMENT
AXIAL ADJUSTMENT
GLASS
or
BRASS

Fig. IV-3 Quartz Tube Mounts

The mechanisms (A) are designed to hold the quartz tube mounts in place inside the discharge electrodes.

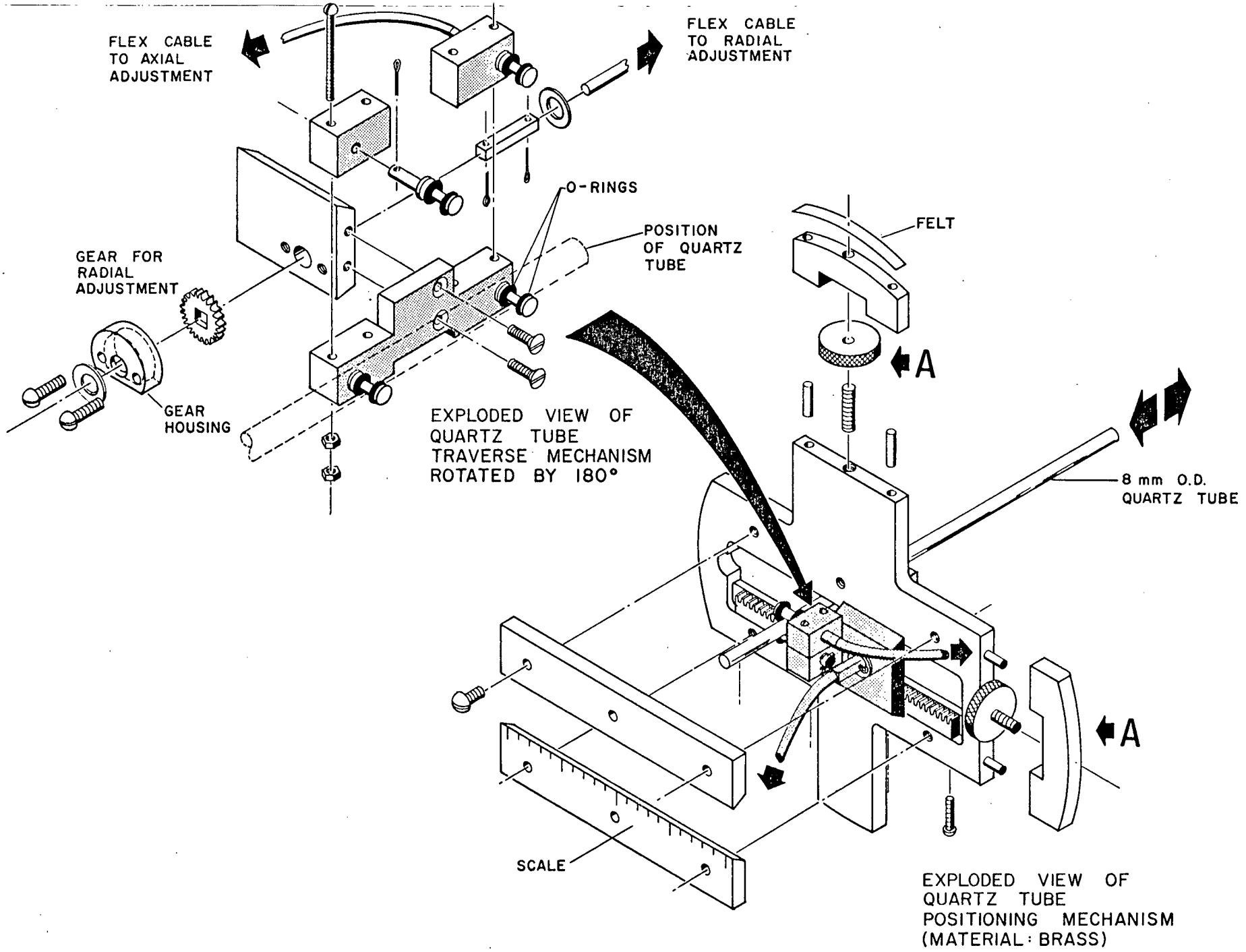
FLEX CABLE TO AXIAL ADJUSTMENT
FLEX CABLE TO RADIAL ADJUSTMENT
O-RINGS
POSITION OF QUARTZ TUBE
GEAR FOR RADIAL ADJUSTMENT
GEAR HOUSING
EXPLODED VIEW OF QUARTZ TUBE TRAVERSE MECHANISM ROTATED BY 180°
FELT
A
8 mm O.D. QUARTZ TUBE
A
SCALE
EXPLODED VIEW OF QUARTZ TUBE POSITIONING MECHANISM (MATERIAL: BRASS)

The quartz tube is held in place between four "O"-ring rollers (see Fig. IV-3). Axial movement can then be achieved by rotation of these rollers. One roller on each assembly, designated as the "drive roller" in Fig. IV-3, is lengthened, to accept the square end of the flexible drive cable.

The drive cables are fixed firmly into the drive roller and radial adjustment gear, but are only inserted into their respective slots on the vacuum feedthroughs, in order not to hamper disassembly and reassembly by the vacuum system.

IV.2 Discharge Characteristics

All measurements were done on the plasma created when a charging voltage of 12 kV. (±0.05 kV.) and a filling pressure of 4 Torr. of helium were used. Under these conditions the current oscillation had a period of 22.4 μsec., and a peak value of 175 kA.

The discharge current was measured with a Rogowski coil consisting of a 12 cm. length of RG63-A/U delay line with the outer conductor removed. This coil is inserted between the leads carrying the discharge current, with the coil axis normal to the direction of current flow. The coil output was integrated using a passive RC integrator (time constant = 1.1 msec.) to give a signal proportional to the discharge current. This signal was then calibrated by manual integration of the current waveform, using the relation:

$$\int I dt = Q \tag{4.1}$$

where I is the current flowing in the discharge, and Q is the total charge stored on the capacitors at the initiation of the discharge.

It was found to be helpful to move the photomultiplier and recording oscilloscopes away from the discharge tube, to reduce the effect of the radio-frequency noise generated by the discharge. In addition, ferrite isolators were used on all coaxial cables connected to these oscilloscopes to break up R.F. ground loops. Additional ferrite isolators were placed in the mains connections to the oscilloscopes and photomultiplier power supply.

The ferrite isolators are constructed by wrapping the cables around a ferrite ring. In the case of coaxial cable, the outer sheath is inductively linked to the ferrite, and has a correspondingly high inductance. The centre conductor is shielded from the ferrite by the outer sheath. In the case of the mains connection, of course, all the mains lines have a high inductance. Thus, high frequency signals propagating along the ground connection or on the mains are attenuated.

IV.3 Experimental Objectives

As has been previously mentioned the breakdown of a Z-pinch is characterized by a preferential current flow at the walls of the discharge vessel. Once breakdown has occurred the axial current $\underline{j}$ grows rapidly and interacts with its own

azimuthal magnetic field, $\underline{B}$. The resulting $\underline{j} \times \underline{B}$ force drives the current shell radially inward. Associated with the radial collapse of the current shell is the development of ionization.

The ionized gas carries some of the axial current and is trapped by the magnetic field. In this way, the gas in the discharge vessel is heated, ionized, trapped and compressed by the collapsing current shell.

To understand the dynamics of the collapse, it is necessary to know both the distribution of mass and the distribution of current in the discharge, in order to calculate the forces acting on the gas.

The distribution of current has been measured accurately by J. Pachner of this laboratory, using a three-coil probe[3]. This probe has a spatial resolution which is a factor of four better than the conventional single coil probe.

The current measurements were not made on the same Z-pinch as the laser interferometric measurements of electron density. The two discharge systems were, however, effectively identical, in electrical as well as geometric characteristics.

It was with the intention of determining the mass distribution in the discharge, that laser interferometric measurements have been made. The laser interferometer is most sensitive when used as a detector of electron density. Since plasmas are quasi-neutral, however, the measurement of the electron distribution gives that of the ions as well, and hence the distribution of mass directly affected by Lorentz forces.

V Experimental Procedures

V.1 Introduction

This chapter will deal with the details of the experimental procedures. The first section describes the way in which the interferometer is aligned. This procedure has two facets: first, the alignment of the laser beam parallel to the discharge tube axis, and second, the alignment of the resonator mirrors to produce beam overlap and good resonance. The next section describes the triggering electronics used to ensure that the discharge breakdown occurs when the resonator configuration is appropriate for measurement. The third section presents details of the measurements, with sample data and graphical reductions from this data. The chapter closes with a discussion of errors.

V.2 Resonator Alignment

The Fabry-Perot interferometer measures the integrated electron density along the resonator axis. To deduce the electron density from Fabry-Perot fringe patterns, it is necessary that something be known about the distribution along the resonator axis. In the Z-pinch, this means aligning the resonator axis parallel to the discharge tube axis, as, along any such line, the electron density is constant.

The resonator axis is made parallel to the discharge tube axis as follows: The lens L_1 (see Fig. V-1) is removed, and the graduated steel rods (R in Fig. V-1, ruled every 0.025") are inserted into the discharge tube through the ports (A) in the discharge vessel. The ports are 1/4" I.D. and are located 22 cm. on either side of the discharge tube centre. As Fig. V-1 shows,

Fig. V-1 Discharge Tube and Interferometer

The view is a horizontal, diametral cross-section, illustrating the alignment procedure.

PM2	-	alignment photomultiplier
PM1	-	resonator monitoring photomultiplier
M_1, M_2	-	laser cavity mirrors
M_2, M_3	-	resonant cavity mirrors
QB	-	quartz block (seen from above)
L_1, L_2	-	lenses
E	-	discharge electrodes
G	-	pyrex discharge vessel
R,R	-	graduated rods
A,A	-	tube ports

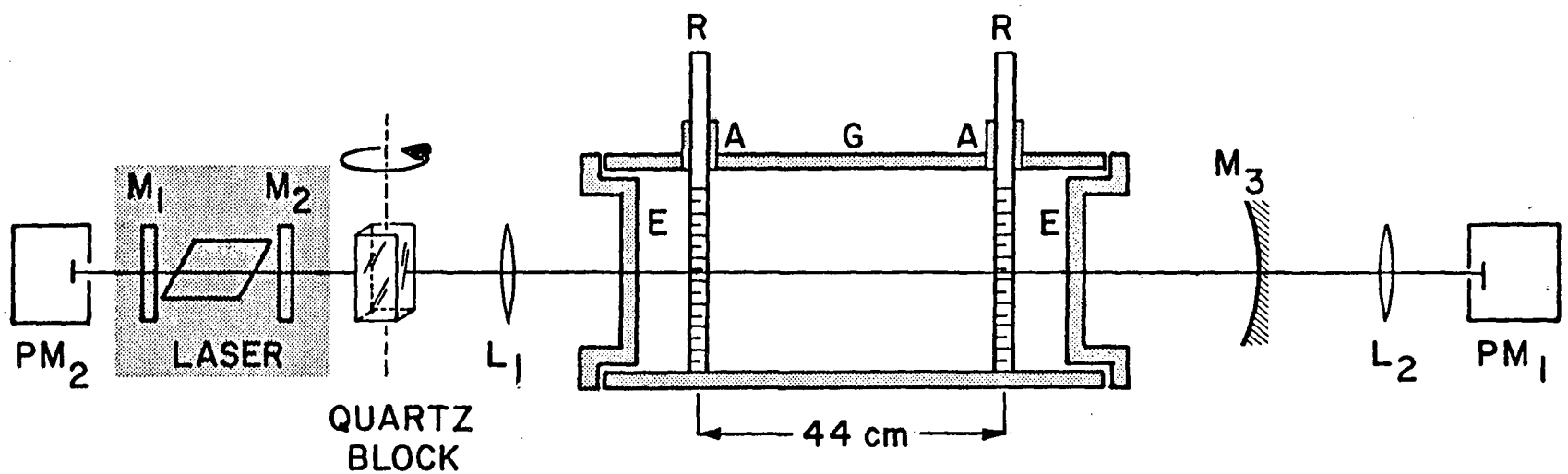
R
R
A
G
A
M1
M2
E
E
M3
PM2
LASER
L1
QUARTZ
BLOCK
44 cm
L2
PM1

the rods are in the same horizontal plane. The rods are pushed into the vessel until their ends abut on the opposing wall.

The points at which the laser beam strikes the rods are noted. The resonator axis is then adjusted until these points are the same distance from the discharge tube wall. The resonator axis is then parallel to the discharge tube axis.

From the known inner diameter of the discharge vessel, and the distance of the resonator axis from the tube wall, the location of the resonator axis, relative to the discharge tube axis, is easily deduced. The optical bench which supports the resonator and laser may be moved laterally with respect to the table on which it stands. The position of the optical bench for which the resonator and discharge axes would be coincident is noted, and henceforth the radial position of the resonator axis is determined by its distance from the discharge axis point.

Once this procedure is completed, the rods are removed and the side ports sealed up. Mirror M_3 (see Fig. V-1) is now adjusted to send the laser beam back on itself. The accuracy of this alignment is easily monitored with PM2. The better the alignment, the better the beam overlap, and the better the coupling from the external resonator to the laser. The mechanical vibrations of the external resonator mirrors produce changes in the phase of the radiation being fed back, and these vibrations are sufficiently slow that the feedback variations produce variations in laser power.

Once the amplitude of the oscillations observed by PM2 have been maximized by the adjustment of M_3, lens L_1 is reinserted into the system. This lens is then adjusted to remaximize the laser power fluctuations. This new maximum is

larger than the previous one, as the presence of L_1 converts the resonator into a concentric one with correspondingly better beam overlap. This procedure ensures that L_1 does not produce a small divergence between the resonator axis and the discharge tube axis.

The quartz tubes are now rolled into position so as to enclose the laser beam; a suitable spacing between their ends is chosen, and the resonator alignment is complete. Final alignment consists of directing the transmitted beam to the face of photomultiplier PM1, using lens L_2 (Fig. V-1) to keep the beam from diverging. It is necessary that L_2 have a focal length such that the centre of curvature of mirror M_3, located at the refraction point, be focussed on the photomultiplier surface.

The specifications of the interferometer components are found in Table II, on the following page.

In the course of the experiment, it became apparent that better interference conditions, and hence greater amplitude of the resonator output oscillations, could be obtained when the resonator length (the distance between mirrors M_2 and M_3, Fig. V-1, typically 5m.) was an integral multiple of the 35.5 cm. laser cavity length.

This effect has been observed by others[16], and has been attributed to the excitation of more than one axial mode in the laser cavity.

V.3 Triggering Circuitry

The previous section has described the alignment of the resonator and the introduction of the reference object. This reference object, the quartz block, must be in such a position that the resonator is aligned when the discharge is to be

TABLE II - Interferometer Components

Laser:	Spectra-Physics Model 130C
	Continuous He-Ne (6328Å)
	Beam Power: 1.0 mW.
	Beam Diameter (at e^{-2} points): 1.4 mm.
	Beam Divergence: 0.7 mrad.
Lenses:	L_1 : focal length = + 1.27 m.
	L_2 : focal length = + 2.5 m.
Interference Filter:	Baird-Atomic; 43 Å bandpass
	about 6330 Å; Maximum transmission 60%
Photomultiplier:	Phillips 150 CVP, Risetime: 8 nsec.
	Fluke Model 412B high voltage power supply
Oscilloscopes:	Tektronix Type 551 Dual Beam

External Mirrors (M_3):

Type	Spherical
Substrate	Fused quartz
Surface Coating	Multi-layer dielectric
Radius of Curvature	1.0 or 2.0 meters
Diameter	3.8 cm.
Reflectivity at 6328 Å	60%

This configuration produces 30 MHz oscillations with an amplitude of 10% of the background beam intensity.

triggered. The angular position and frequency of rotation of the quartz block must also be such as to provide a resonator output oscillation frequency, f_o, approximately equal to f_b, as defined in Sec. IV.4. This section will describe the way in which this is done.

The basic triggering circuitry is shown in Fig. V-2. The triggering source is a photodiode, set up to intercept the light reflected from the front face of the quartz block. As the quartz block is rotated, the beam is swept over the photodiode, producing one pulse per cycle of block rotation. (The rotating assembly includes a geometrically similar opaque block as a counterbalance.) These pulses are shaped, and then fed into an interval recognition detector (IRD) which produces an output pulse as soon as the pulse interval, T, is equal to or less than some preset value. Figure V-3 shows a block diagram of the IRD, and a detailed circuit diagram is given in Appendix II. Coincidence between an input pulse and the one-shot pulse is recognized by the NAND gate. The coincidence output triggers the one-shot which provides the output pulse.

To allow the quartz block to rotate through a small angle before the discharge is triggered, the IRD output pulse can be delayed by the delay unit shown in Figure V-2. This configuration allows the small adjustments necessary to ensure that $f_o = f_b$ when the discharge is triggered (see Section IV.4).

The operating procedure requires that the quartz block driving motor be turned on when all other preparations have been made to fire the discharge (i.e., the filling pressure has been reached, capacitors fully charged, and oscilloscope camera shutters opened). As the quartz block angular velocity increases, the pulse repetition rate from the photodiode increases, until it is sufficient to trigger the IRD.

Fig. V-2 <u>Triggering Circuitry</u>

M_1, M_2	-	laser cavity mirrors
M_2, M_3	-	resonator mirrors
L_1, L_2	-	lenses
PD	-	photodiode (FPT-100)
IF	-	interference filter
PM	-	photomultiplier

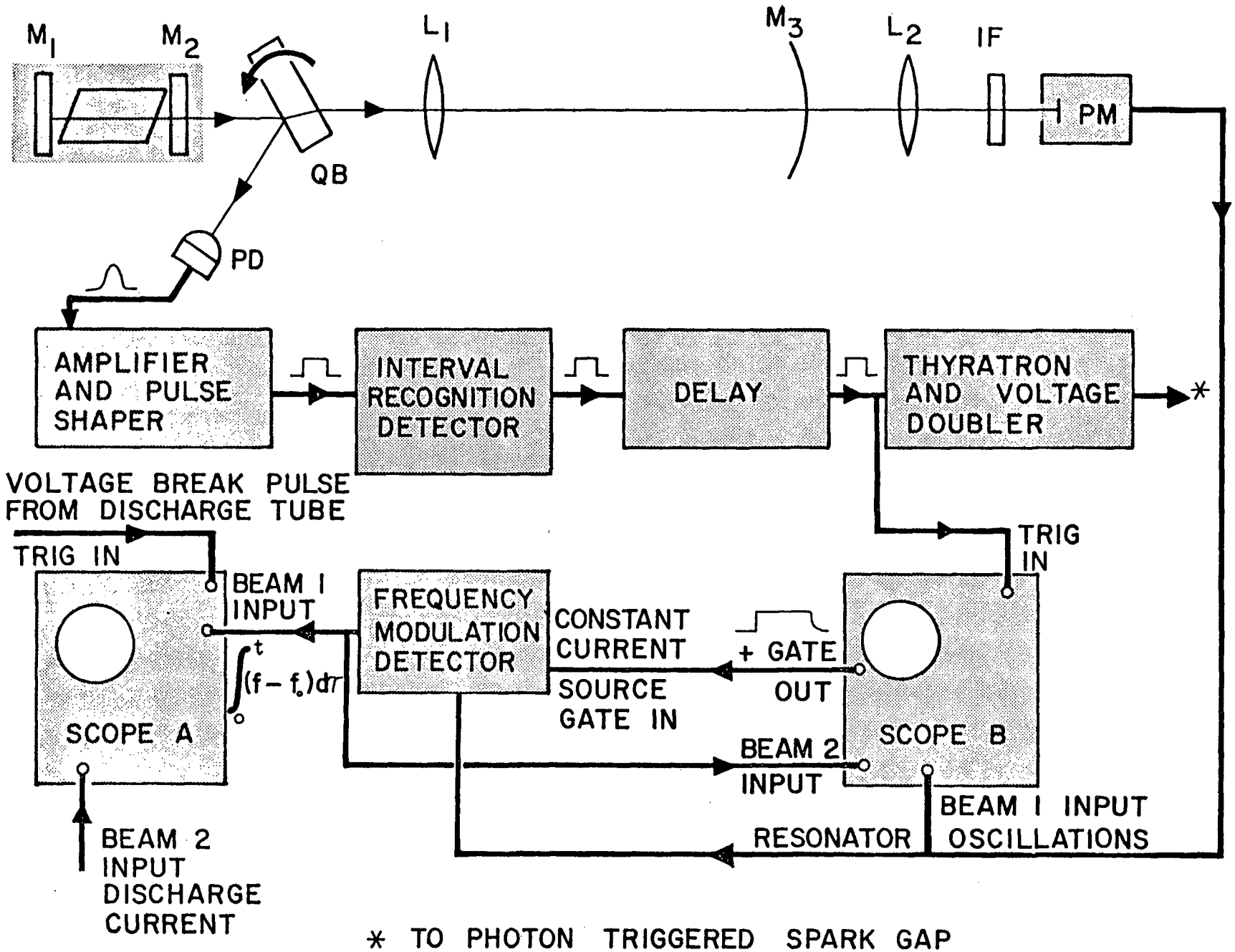

* TO PHOTON TRIGGERED SPARK GAP

Interval Recognition Detector

Fig. V-3 (a) Block Diagram

Fig. V-3 (b) Pulse Sequence

R - external variable resistor which determines T, the interval recognized.

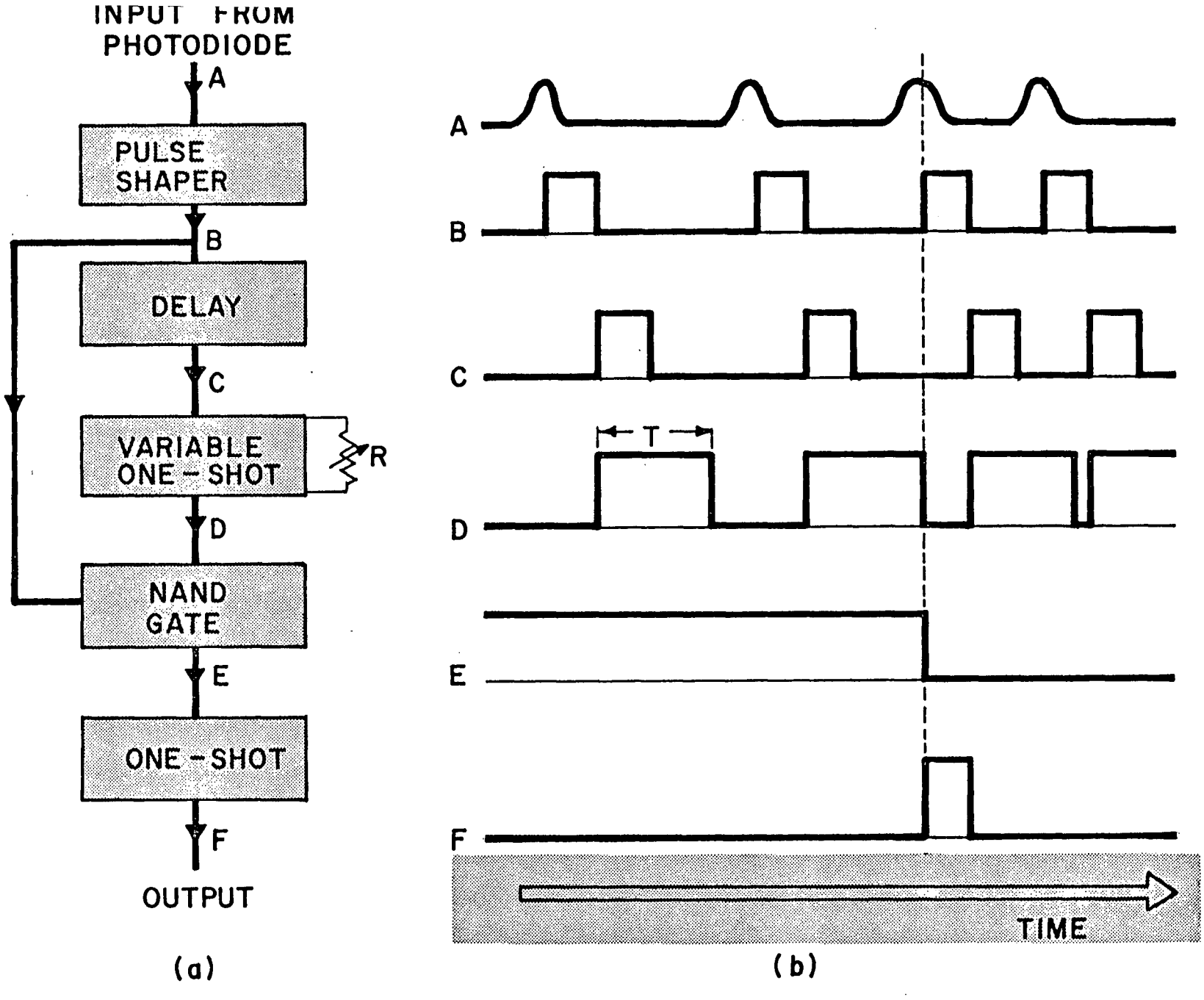
INPUT FROM PHOTODIODE
A
PULSE SHAPER
B
DELAY
C
VARIABLE ONE-SHOT
R
D
NAND GATE
E
ONE-SHOT
F
OUTPUT
(a)
A
B
C
T
D
E
F
TIME
(b)

The delayed IRD output goes to the thyratron unit and voltage doubler, which delivers a voltage pulse to the spark light source of a photon-triggered pulse generator (see Fig. II-1). Ultraviolet photons from the light source pass through an enclosing quartz bulb and illuminate the electrodes of the air spark in the trigger pulse generator.[22]. The output of this generator fires the main spark gap switch.

Using an ultraviolet light source to fire the trigger pulse generator ensures that low voltage triggering and measuring electronics are completely decoupled electrically from the high power discharge circuit, which reduces the noise picked up by the measuring circuits. The ultraviolet light source cannot be used to trigger the main gap directly for two reasons. First, the technique will only trigger gaps which are operated at a few hundred volts below the breakdown voltage. This requires accurate electrode placement which is impossible in the main gap because of electrode erosion. Second, the quartz bulb could not withstand the temperatures generated in the main spark gap.

The final triggering sequence is shown in Fig. V-4. The delayed IRD pulse (Fig. V-4(a)) goes to the thyratron and voltage doubler, by which it triggers the discharge, and to the trigger input of scope "B" (for triggering circuitry block diagram, see Fig. V-2). As a result, scope "B" begins to sweep immediately, and after a short delay through the triggering spark gaps (t_f in Fig. V-4), the discharge breaks down. The + GATE output of scope "B" is used to turn on the constant current source in the IFMD (see Fig. IV-3). The delay t_f is sufficient to ensure that the IFMD is functioning by the time the discharge fires. The IFMD stays on as long as scope "B" continues to sweep. This sweep time must be greater than t_f (approximately 4 μsec.) plus the

Fig. V-4 Triggering Sequence

The delayed IRD pulse triggers oscilloscope "B", and the voltage spike "A" triggers oscilloscope "A". The photograph is of the "A" trace.

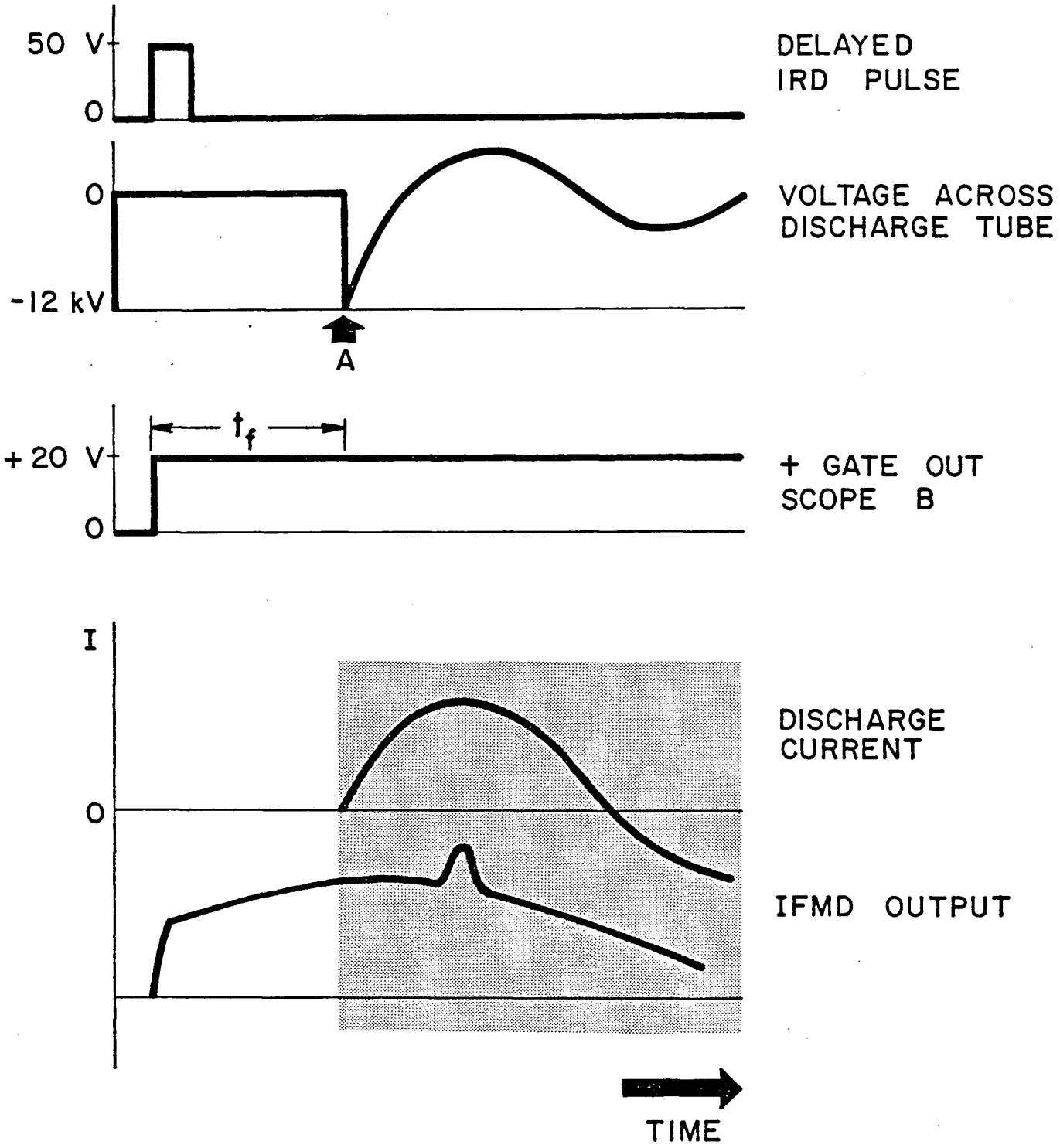

SHADED AREA CONSTITUTES
PHOTOGRAPHIC RECORD

duration of the observation (set by the duration of "A" scope (see Fig. V-4) sweep, usually 20 μsec. The breakdown of the main trigger spark gap puts the full capacitor voltage across the discharge electrodes. This voltage pulse (A in Fig. V-4(b)) is used to trigger scope "A", on which is displayed the discharge current and the electron density at the observation point. This display is photographed, and appears as shown in Fig. V-4(d,e).

V.4 Temporal and Radial Profiles

The techniques by which the temporal profiles of electron density are obtained from photographic records, produced as in Sec. V.2, have been discussed in Sec. III.4. Temporal profiles have been obtained at twelve radial positions: at r = 0.75 cm., and at 0.5 cm. intervals from r = 1.00 cm. to r = 6.00 cm. The results are shown in Fig. V-5, which is a perspective view of the temporal profiles arranged in proper sequence. Each temporal profile represents an average over several shots done under identical conditions.

Figures V-6 and V-7 show the temporal profiles generated at two radial positions. These have been included to illustrate the plasma features, whose dynamics are discussed in Chapter VI, and to illustrate the accuracy and reproducibility of the results. The solid lines represent individual shots, and the circles show the average over these individual shots. The interesting features which have been labelled are the precursor, the main peak and the reflection peak.

The other feature of interest is the very large "axial spike", which appears on the axis of the discharge at the time when the precursor arrives on axis. As can be seen in Fig. V-5, this feature is expanding out from the axis.

Fig. V-5. Electron Density Distribution in the Discharge.

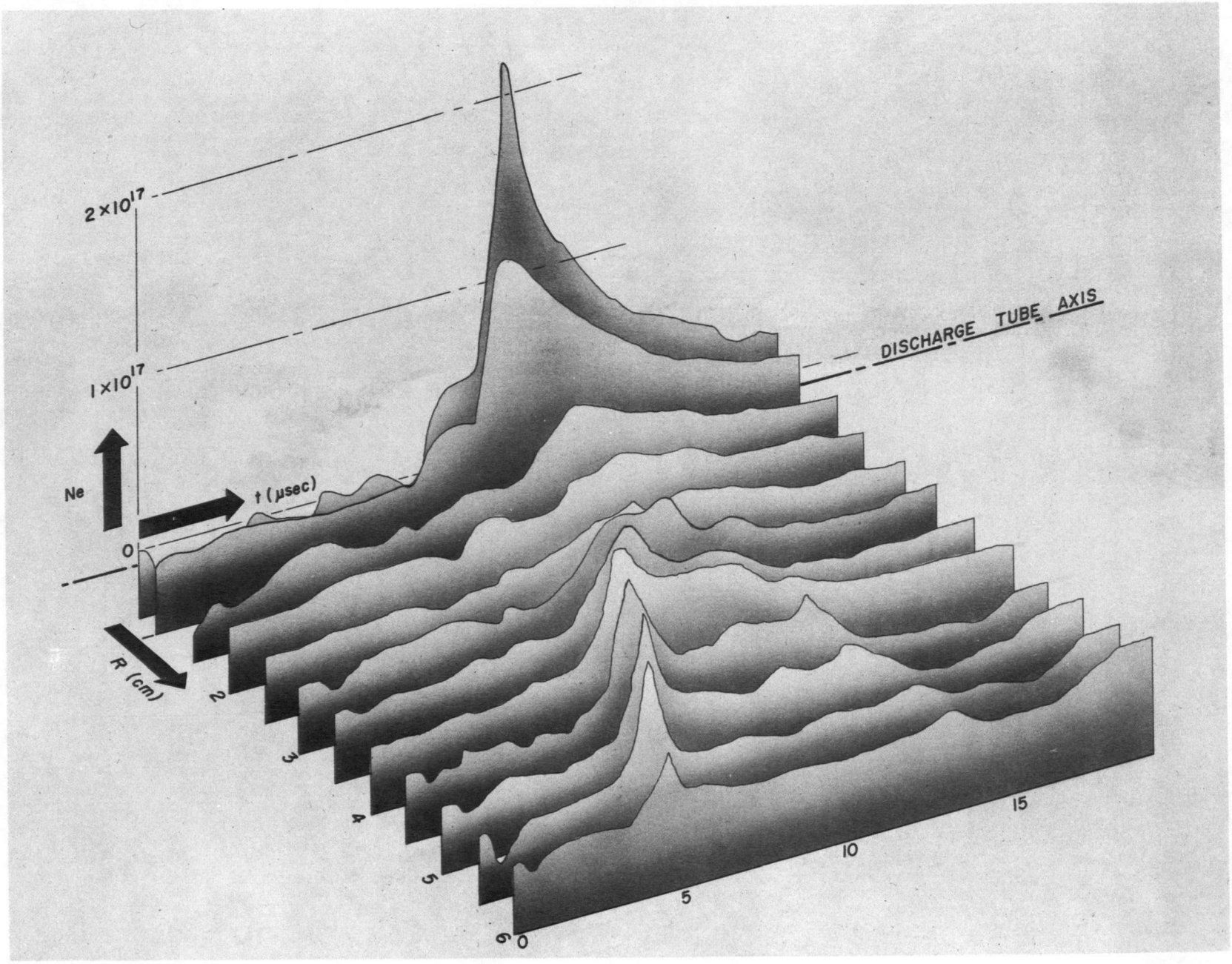
2×10^17
1×10^17
0
Ne
t (μsec)
R (cm)
2
3
4
5
6
0
5
10
15
DISCHARGE TUBE AXIS

Electron Density Temporal Profiles

Fig. V-6: at r = 3.00 cm.

Fig. V-7: at r = 4.00 cm.

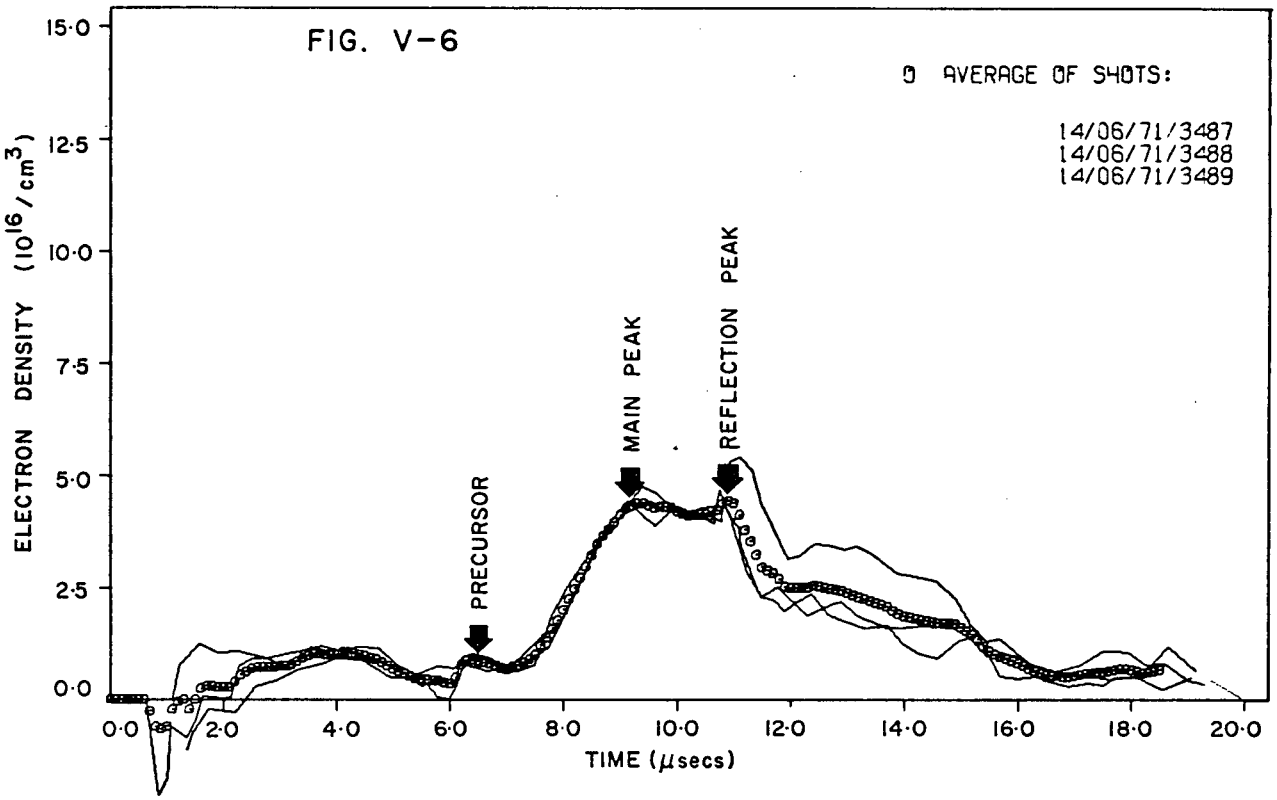
FIG. V-6
AVERAGE OF SHOTS:
14/06/71/3487
14/06/71/3488
14/06/71/3489
PRECURSOR
MAIN PEAK
REFLECTION PEAK
ELECTRON DENSITY ($10^{16}/cm^3$)
TIME (μsecs)
15·0
12·5
10·0
7·5
5·0
2·5
0·0
0·0
2·0
4·0
6·0
8·0
10·0
12·0
14·0
16·0
18·0
20·0

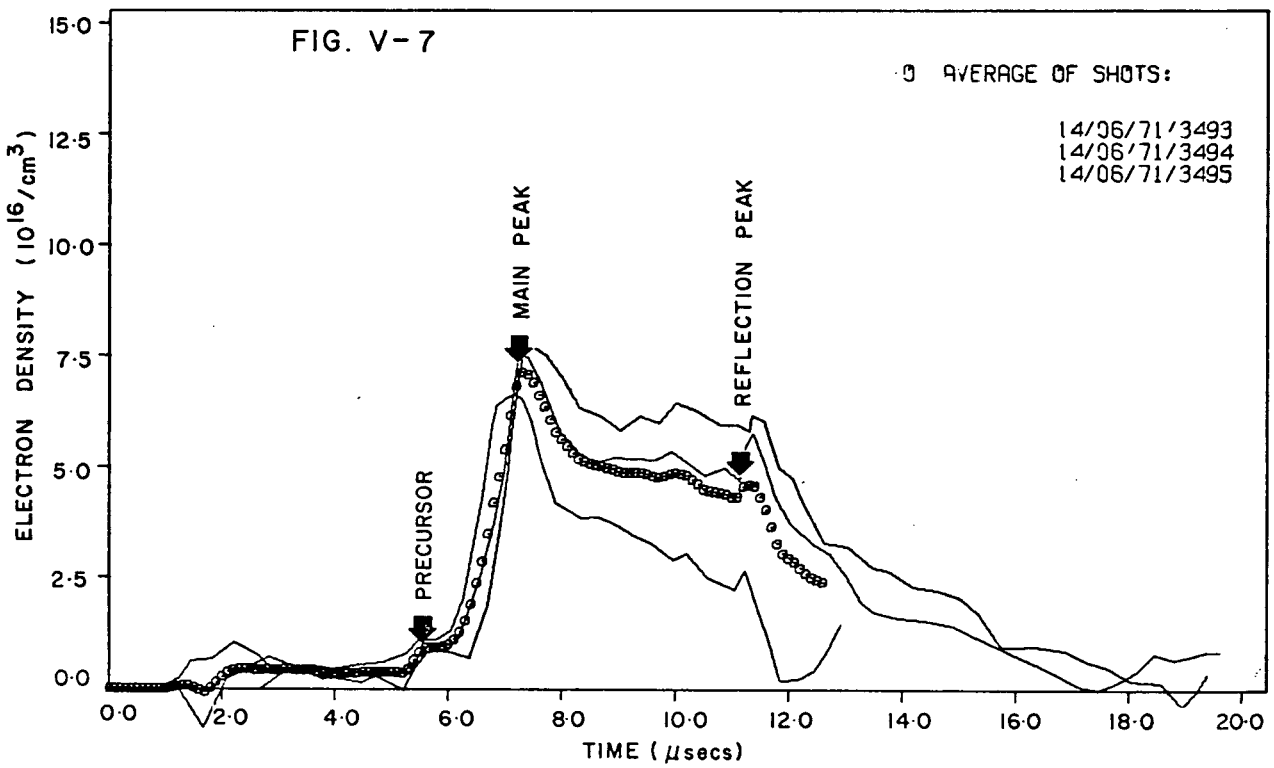
FIG. V-7
AVERAGE OF SHOTS:
14/06/71/3493
14/06/71/3494
14/06/71/3495
PRECURSOR
MAIN PEAK
REFLECTION PEAK
ELECTRON DENSITY ($10^{16}/cm^3$)
TIME (μsecs)
15·0
12·5
10·0
7·5
5·0
2·5
0·0
0·0
2·0
4·0
6·0
8·0
10·0
12·0
14·0
16·0
18·0
20·0

Radial profiles are now obtained by taking a cross-section of the surface of Fig. V-5 at selected times. This technique has been used to generate the radial profiles presented in Figs. V-8, 9, 10.

Figure V-11 shows the trajectories of the four features pointed out on Figs. V-5, 6, 7. In addition, the trajectories of the current peak (obtained from the measurements made by J. Pachner) and of the leading edge of the precursor are plotted.

The current and magnetic field measurements made by Mr. Pachner which are used in the course of this thesis are found in the following figures. Figure V-12 gives the radial current distribution, Figs. V-13, 14, 15 give the radial magnetic field distribution, Fig. V-16 shows the maximum value of j x B observed as a function of time, and Fig. V-17 shows a typical force profile at t = 7.0 μsec.

V.5 Discussion of Error and Reproducibility

The greatest source of error in the absolute values of electron density generated in this experiment is the measurement of the photographs. The large number of photographs to be reduced and the large number of data points on each photo precluded measurement by hand. Instead, the curves in the photos were traced out on an electronic digitizer, and the co-ordinates of the curve were recorded on punched cards which were later analyzed on the IBM 360/67 at the U.B.C. Computing Centre. The limiting factor in the precision of this process is the accuracy with which the digitizer operator can accurately follow the curves on the photos.

Radial Electron Density Profiles

Fig. V-8	t = 1.0 μsec. to t = 5.0 μsec.
Fig. V-9	t = 6.0 μsec. to t = 10.0 μsec.
Fig. V-10	t = 11.0 μsec. to t = 15.0 μsec.

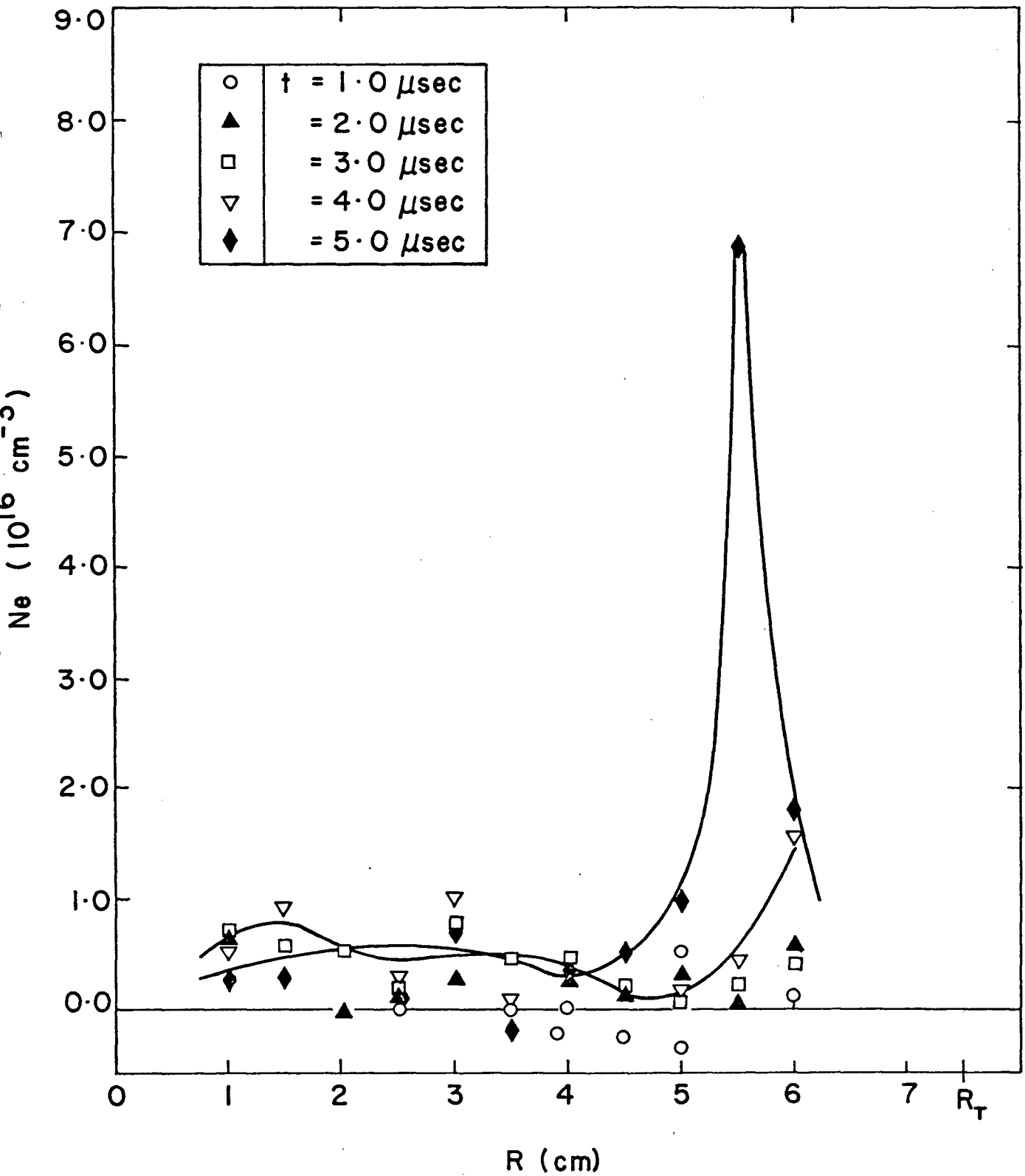
t = 1·0 μsec
= 2·0 μsec
= 3·0 μsec
= 4·0 μsec
= 5·0 μsec
9·0
8·0
7·0
6·0
5·0
4·0
3·0
2·0
1·0
0·0
Ne (10^16 cm^-3)
0
1
2
3
4
5
6
7
R_T
R (cm)

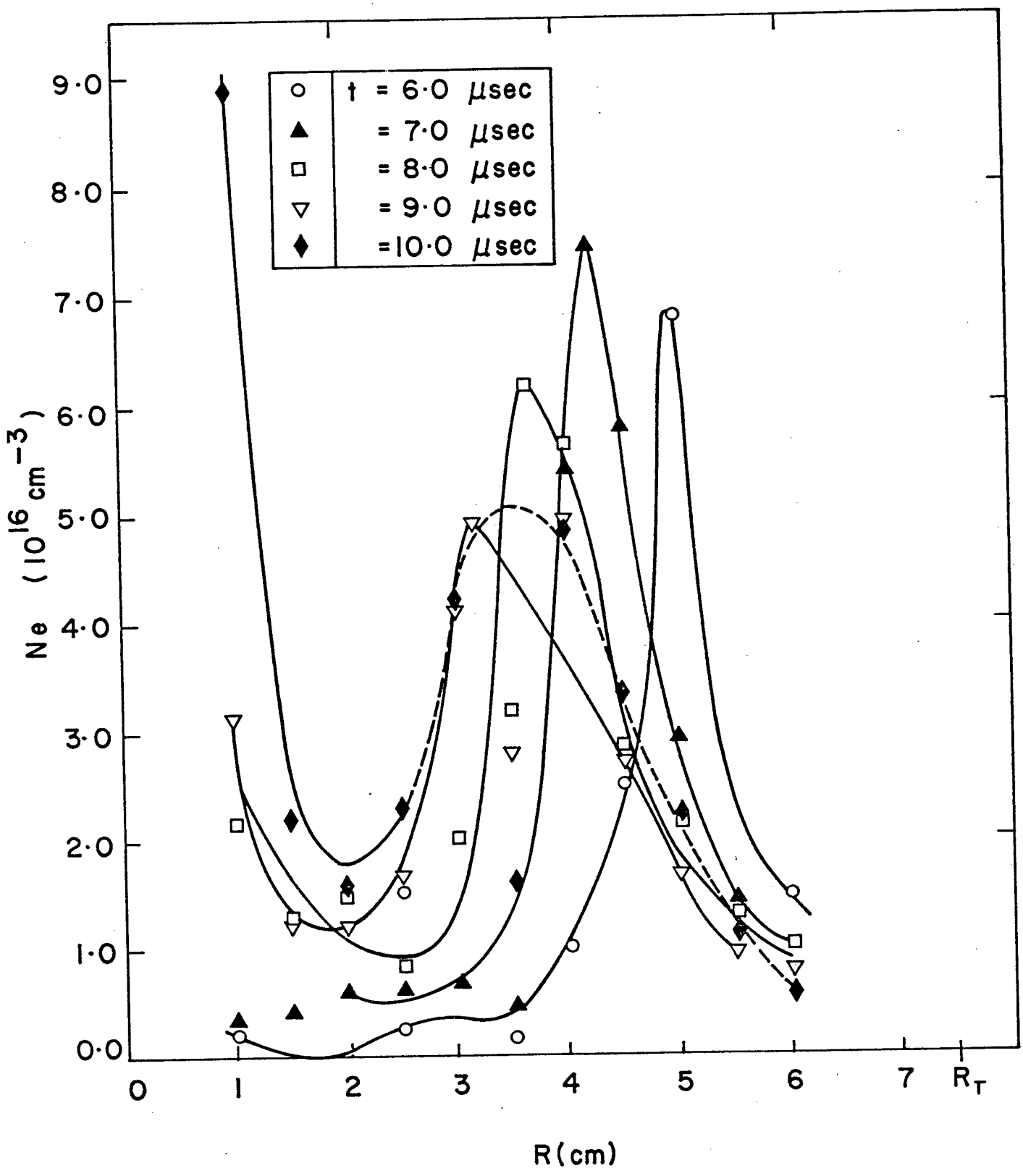
t = 6·0 μsec
= 7·0 μsec
= 8·0 μsec
= 9·0 μsec
=10·0 μsec
9·0
8·0
7·0
6·0
5·0
4·0
3·0
2·0
1·0
0·0
Ne (10^16 cm^-3)
0
1
2
3
4
5
6
7
R_T
R(cm)

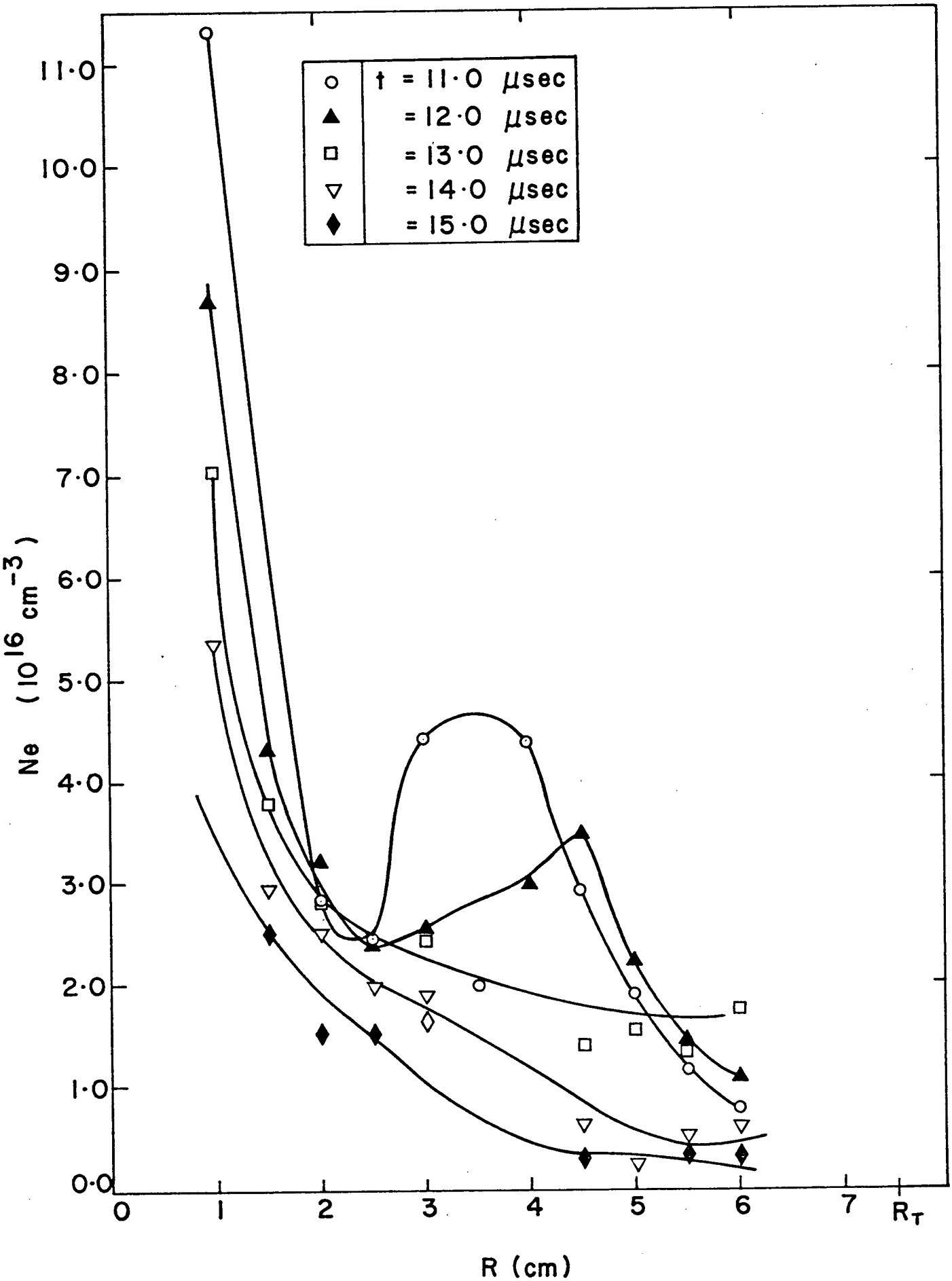
t = 11·0 μsec
= 12·0 μsec
= 13·0 μsec
= 14·0 μsec
= 15·0 μsec
Ne (10^16 cm^-3)
11·0
10·0
9·0
8·0
7·0
6·0
5·0
4·0
3·0
2·0
1·0
0·0
0
1
2
3
4
5
6
7
R_T
R (cm)

Fig. V-11 Radius vs. Time Diagram for Current and Density Features

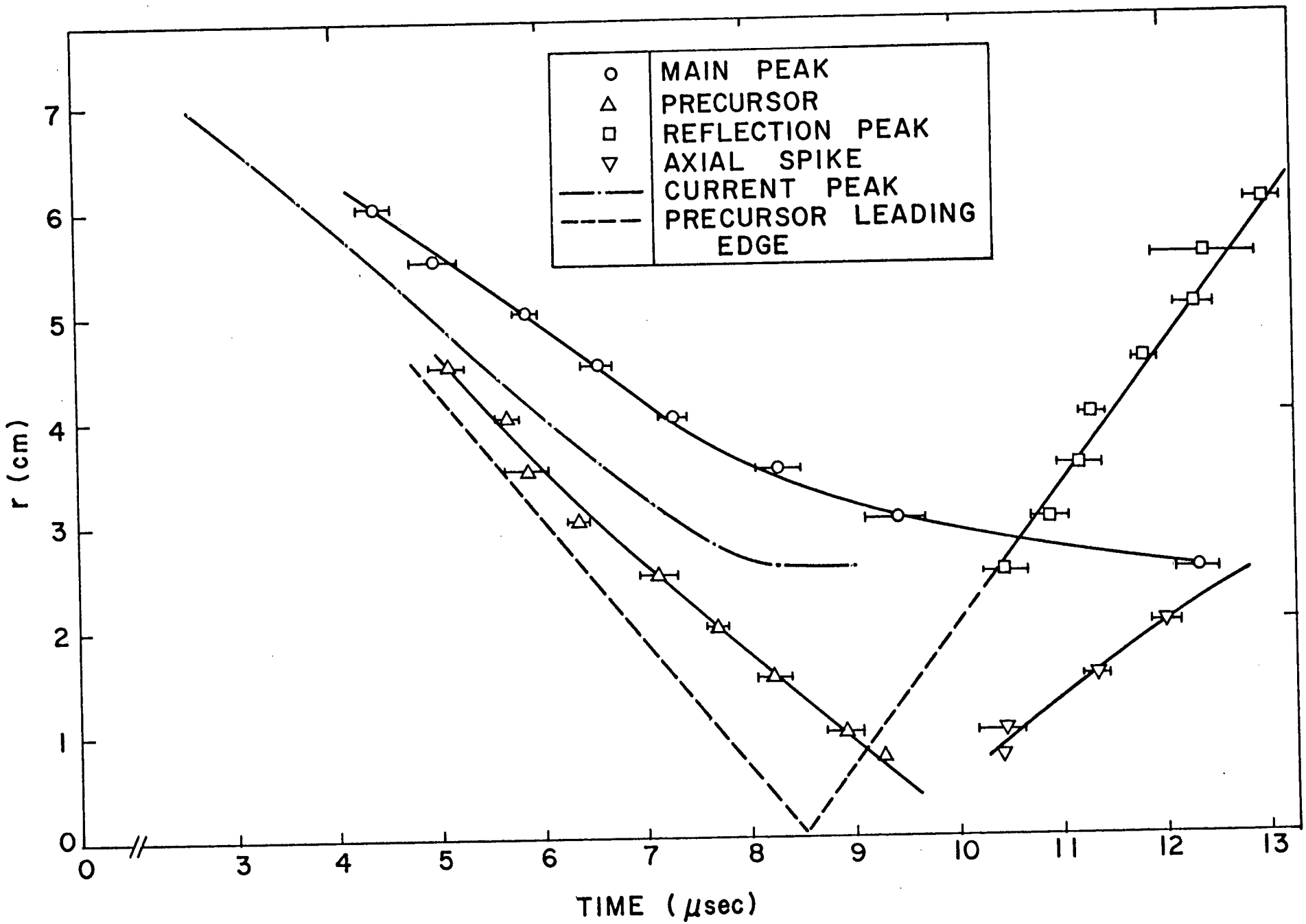
MAIN PEAK
PRECURSOR
REFLECTION PEAK
AXIAL SPIKE
CURRENT PEAK
PRECURSOR LEADING EDGE
r (cm)
TIME (μsec)
0
1
2
3
4
5
6
7
0
3
4
5
6
7
8
9
10
11
12
13

Fig. V-12 Radial Current Distribution

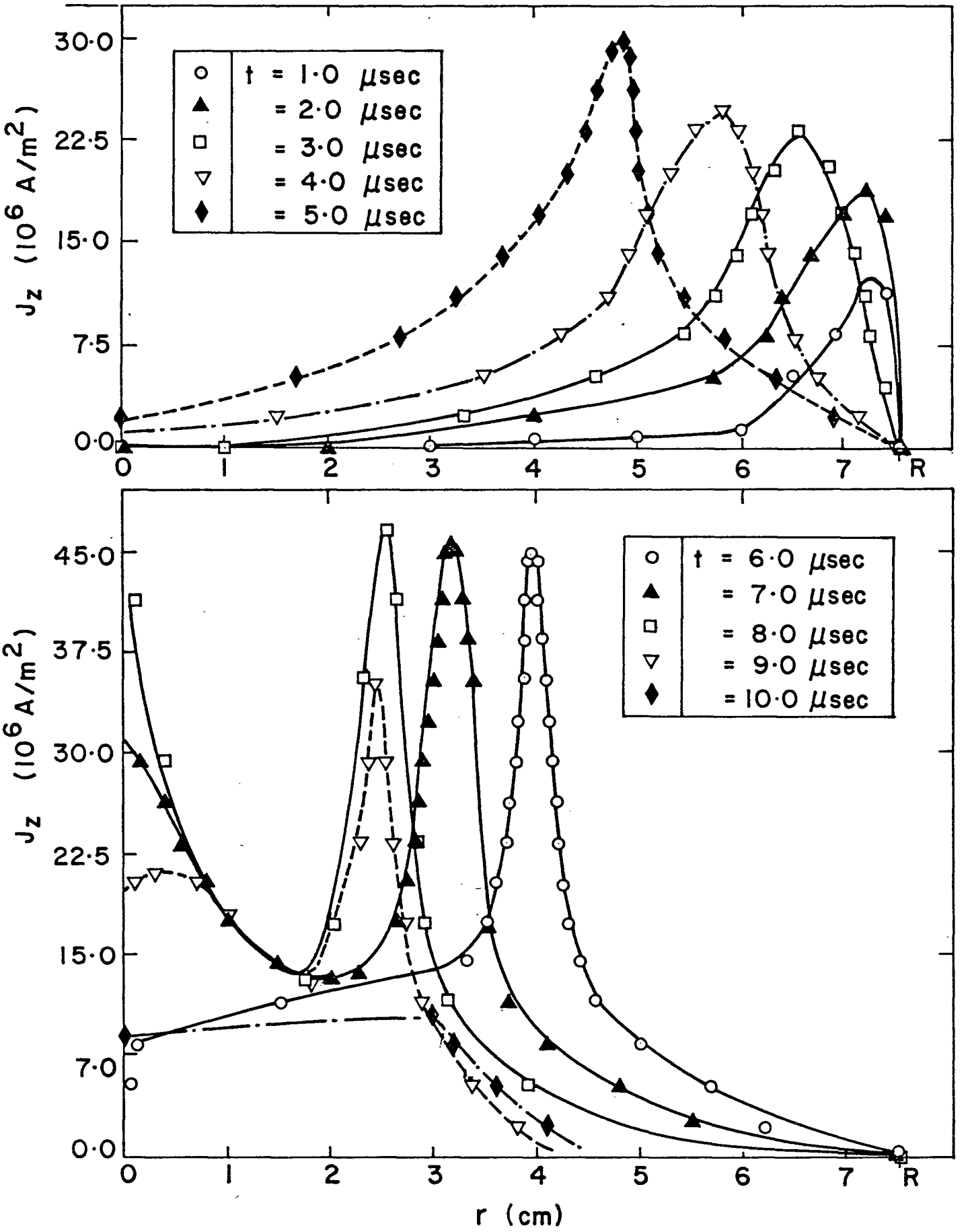
t = 1·0 μsec
= 2·0 μsec
= 3·0 μsec
= 4·0 μsec
= 5·0 μsec
t = 6·0 μsec
= 7·0 μsec
= 8·0 μsec
= 9·0 μsec
= 10·0 μsec
J_z (10^6 A/m^2)
r (cm)
R

Magnetic Field Distributions

Fig. V-13	t = 1.0 μsec. to t = 5.0 μsec.
Fig. V-14	t = 6.0 μsec. to t = 7.0 μsec.
Fig. V-15	t = 8.0 μsec. to t = 10.0 μsec.

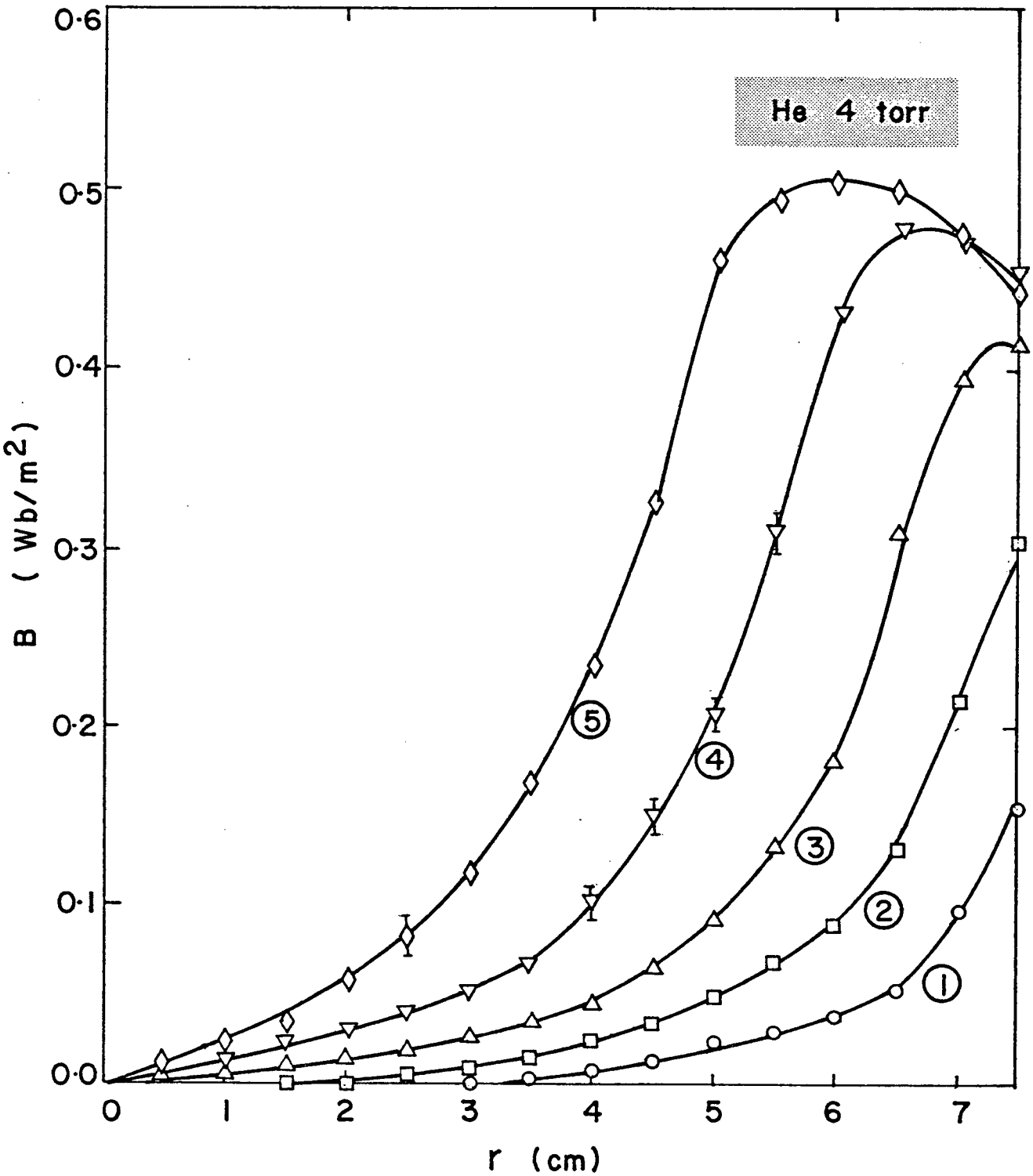
He 4 torr
0·6
0·5
0·4
0·3
0·2
0·1
0·0
B (Wb/m2)
0
1
2
3
4
5
6
7
r (cm)
5
4
3
2
1

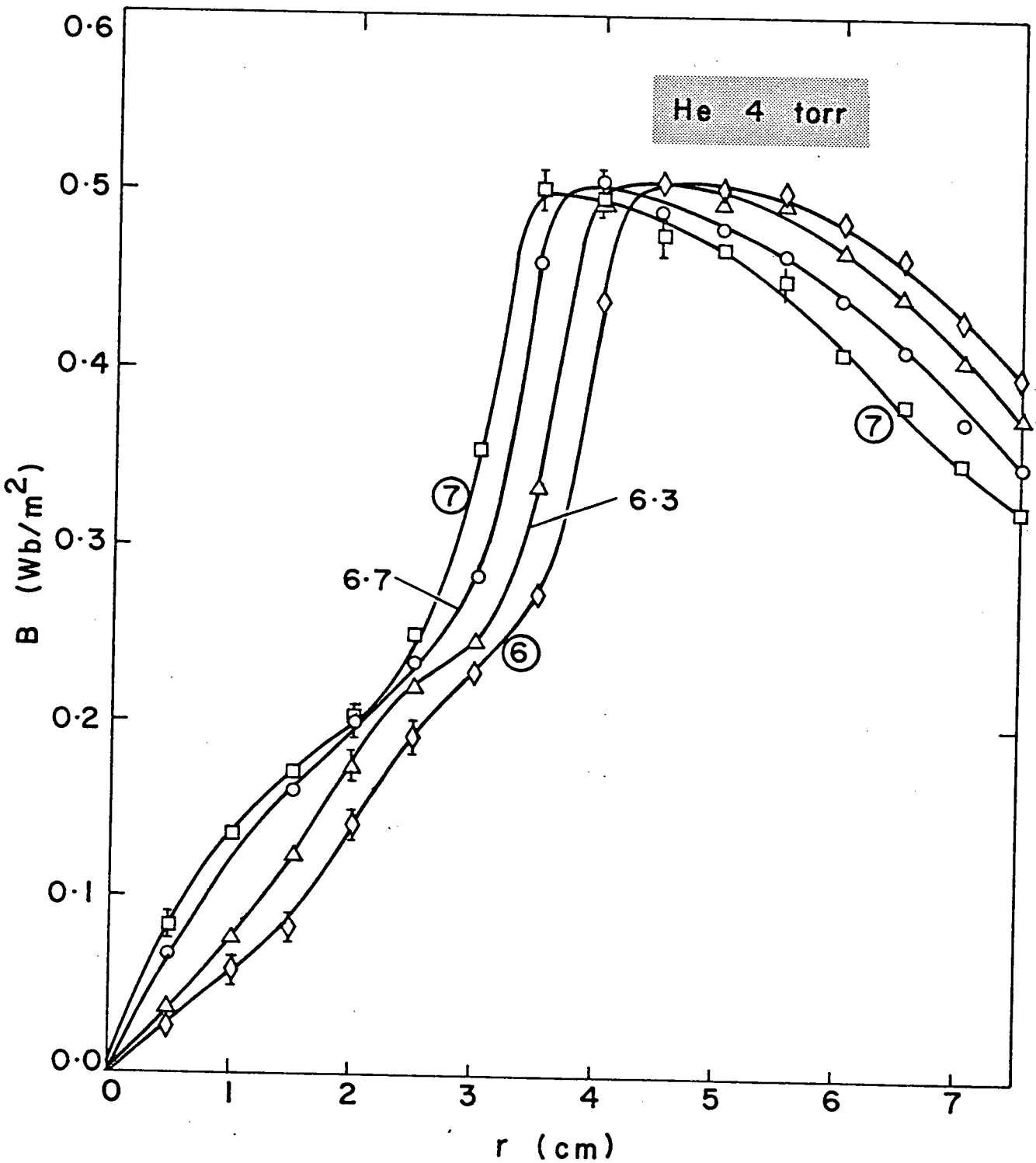
He 4 torr
0·6
0·5
0·4
0·3
0·2
0·1
0·0
B (Wb/m²)
0
1
2
3
4
5
6
7
r (cm)
7
6·7
6·3
6
7

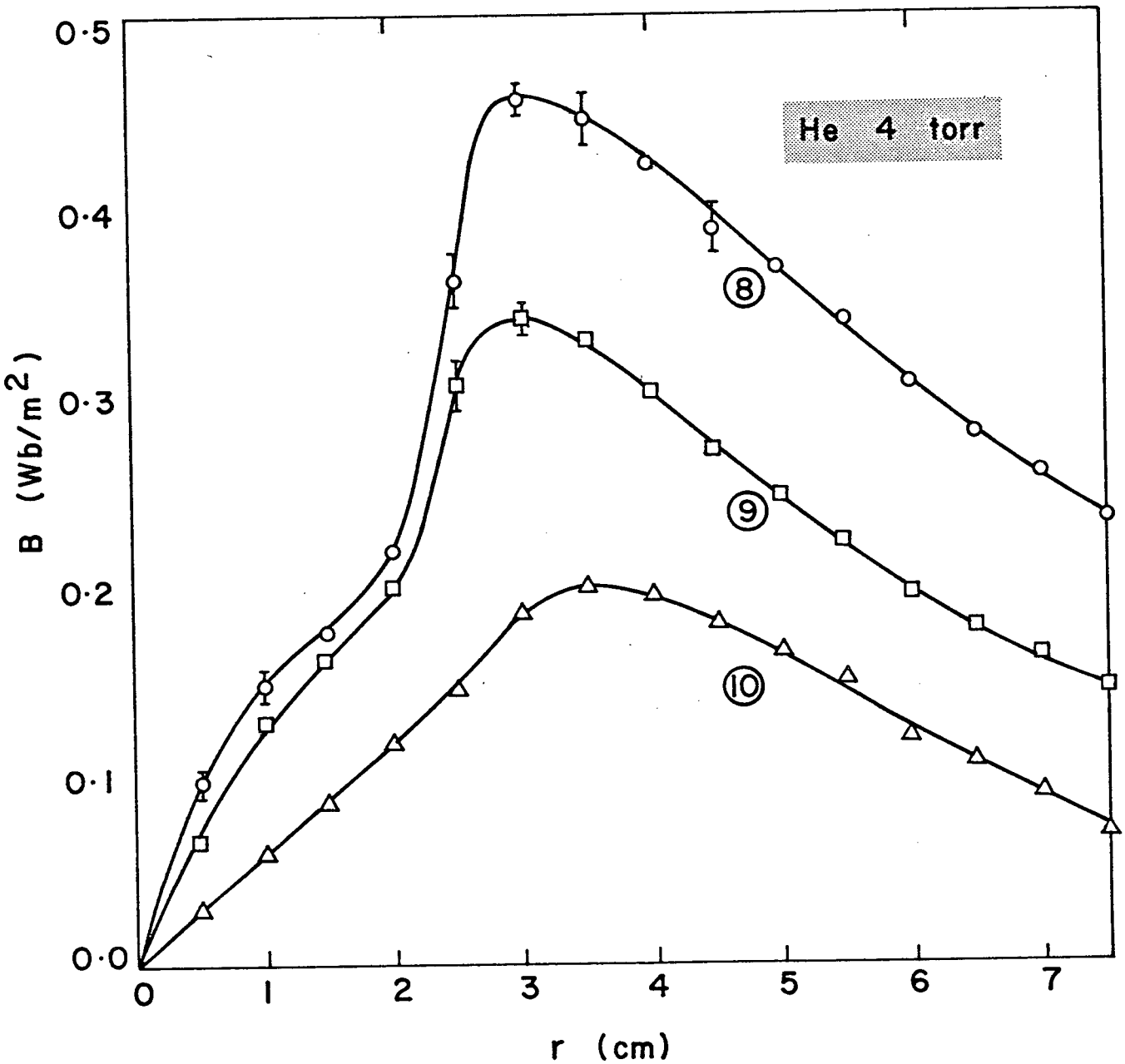
He 4 torr
8
9
10
B (Wb/m²)
0·0
0·1
0·2
0·3
0·4
0·5
0
1
2
3
4
5
6
7
r (cm)

Fig. V-16 Maximum $\underline{j} \times \underline{B}$ vs time

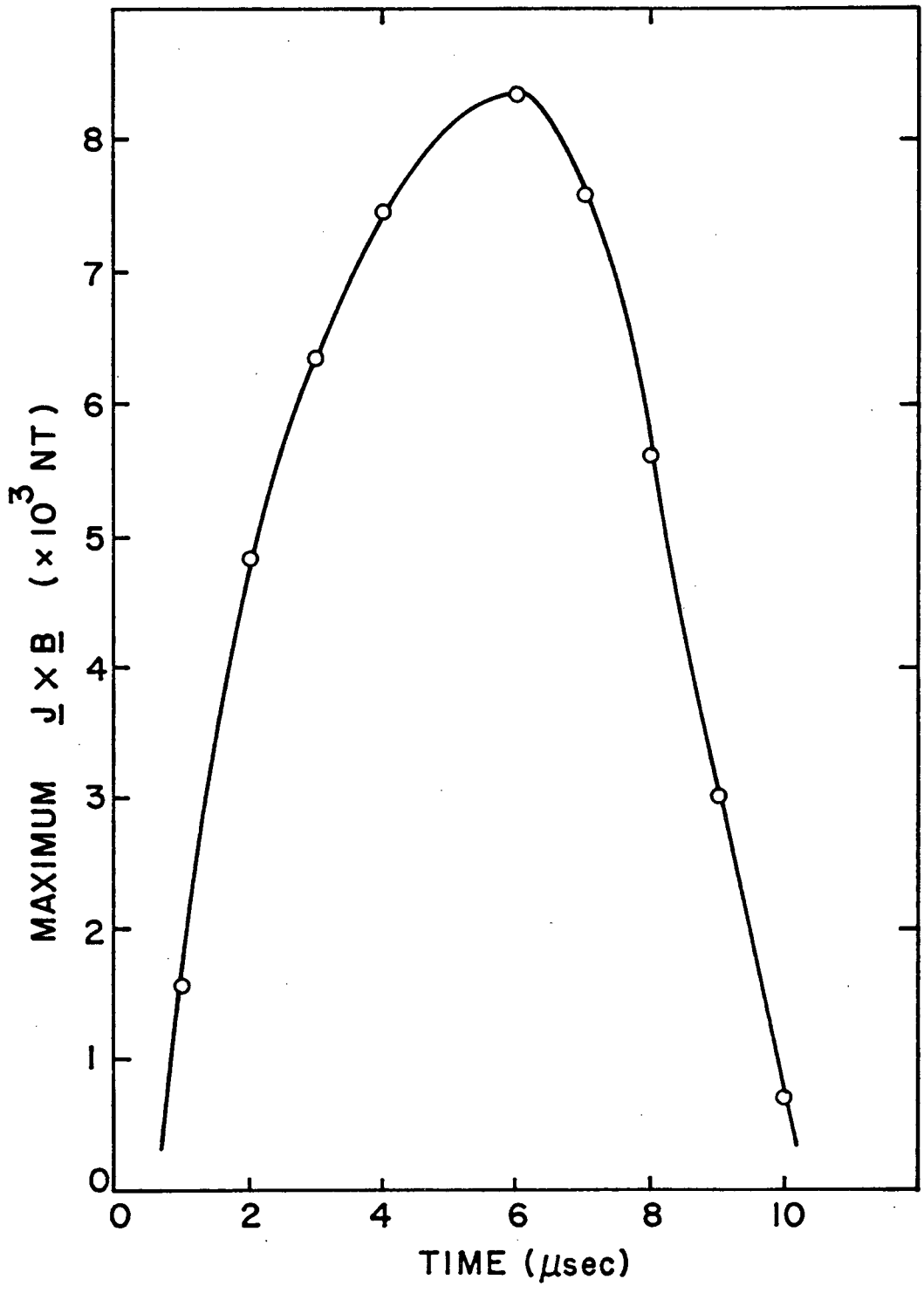
MAXIMUM J × B (×10^3 NT)
0
1
2
3
4
5
6
7
8
0
2
4
6
8
10
TIME (μsec)

Fig. V-17 Force on Current Shell Element vs. Radial Position: t = 7.0 μsec.

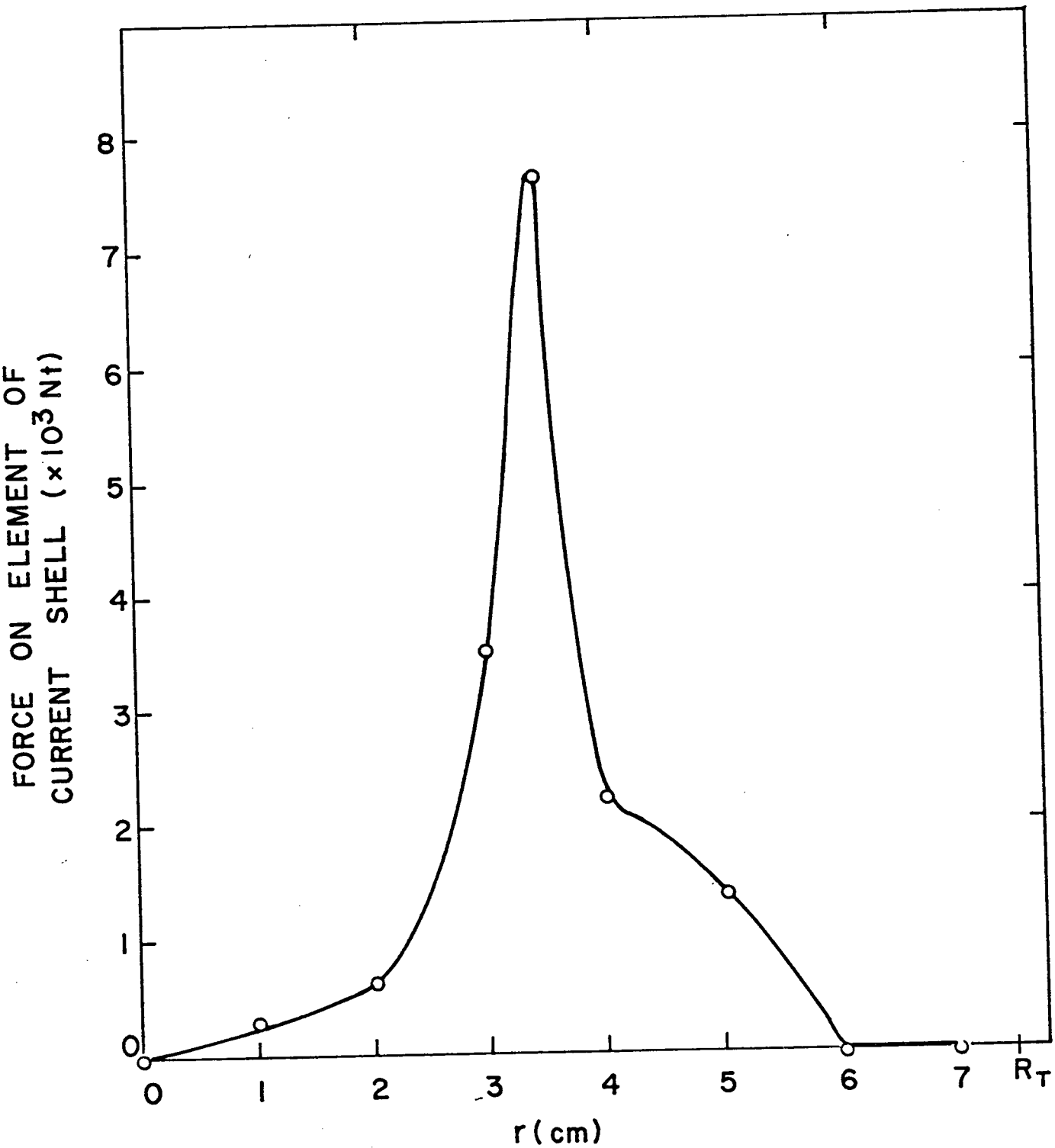
FORCE ON ELEMENT OF CURRENT SHELL (×10³ Nt)
8
7
6
5
4
3
2
1
0
0
1
2
3
4
5
6
7
R_T
r (cm)

In addition, the baseline for each curve must be drawn in by hand, as discussed in Section III.4. This introduces an additional uncertainty, but only for the value of N_e at later times. The value of the main peak density should be quite accurate. It is quite difficult to assign, a priori, a value to the error to be expected from these sources, but it is certain to be less than 10%.

It is also difficult to estimate the measuring accuracy by comparing runs done under identical conditions. Some properties of the plasma are sensitive to the initial discharge conditions, and the accuracy with which the filling pressure could be set was only about ±10%. This may alter the plasma temperature slightly, which will produce much larger fluctuations in the electron density (N_e has an exponential dependence on temperature). For this reason, fluctuations in calculated temporal profiles from shot to shot (see Fig. V-6, 7) are attributed to a lack of shot-to-shot plasma reproducibility rather than to measuring inaccuracies.

The measurement of time from the photographs is much more accurate. This measurement is limited in accuracy by the linearity of the oscilloscope time-base (less than ±100 nsec. over the central 80% of the screen as measured with a calibrated, crystal-controlled oscillator).

As will be seen in the ensuing chapter, the data analysis will be concerned almost entirely with the velocities of the significant features indicated in Figs. V-6, 7, and very little with their amplitudes.

Furthermore, the errors associated with the absolute electron density values do not figure so prominently in the measurement of relative changes in N_e during a run. Thus, if the electron density is said to be slowly varying for several

microseconds, the absolute density is accurate to ±10%, but the slope of dN_e/dt is much more accurately known.

VI Results

VI.1 Introduction

This chapter begins with a presentation of the significant features of the data presented in Sec. V.4. It contains a model which can be used to account for the observed features. It concludes with an example of how the dynamics of the discharge can be used to reveal the characteristics of the plasma in which they move.

VI.2 Summary of Results

Examination of the electron density distribution as a function of time and radial position, illustrated in Fig. V-5, brings to the attention four features of importance.

First is the result that the radial electron density distribution is divided into two distinct regions. The division occurs at r = 2.50 cm. In the region of r greater than this value, an ionized layer implodes toward the discharge axis, as one would expect in a conventional Z-pinch. For r less than 2.50 cm., there is no evidence of this collapsing shell. It has been brought completely to rest, and only a small fraction penetrates to the inner zone.

The second feature is that the degree of ionization, with the exception of the "axial spike" region, is low. At room temperature, the number density at 4 Torr. is:

$$1.33 \times 10^{17} \text{ cm.}^{-3}.$$

Nowhere in the outer region does the density exceed 8×10^{16} cm.$^{-3}$ (i.e. 60% of the filling density).

Third, it can be seen that, in the outer regions of the plasma, following the passage of the ionization shell, the electron density at a given radius remains constant for periods of several microseconds. (see Figs. V-6, 7 in the interval between main and reflection peaks).

Finally, there is the "precursor". It can be seen fully separated from the "main peak" at t = 5.1 μsec. and r = 4.50 cm., and thereafter propagates in to the axis at a constant velocity. The tremendous burst of ionization in the "axial spike" is associated with the arrival on axis of this precursor.

Further details of the collapsing ionization shells are evident in Fig. V-11. First, it is seen that the "main peak" velocity is constant, at 7.3 Km/sec., from the first observation at r = 6.0 cm to r = 4.0 cm., at which point it begins to decelerate, and the current peak decelerates simultaneously.

However, it is easy to see from Fig. V-11, that the "main peak" is outside the current peak, and that the spacing between them increases from 5 mm. to 9 mm. in the time interval 4.5 μsec. to 8.0 μsec. Furthermore, less than 10% of the ionized gas is actually coincident with 75% of the current.

Although both current peak and "main peak" are brought to rest, the ionization feature stops at r = 3.0 cm. while the current peak stops at r = 2.50 cm. In addition, although deceleration begins simultaneously for the two peaks, the ionization peak stops more gradually than the current peak, reducing the separation of the two from 9 mm. at 8.0 μsec to 5 mm. at 9.5 μsec.

The ionization trajectories indicate that the "precursor" leading edge arrives on axis at approximately 8.5 μsec., and that the "reflection peak" originates on axis at this time.

Finally, the radial current profiles indicate the presence of large axial current densities at t = 7.0 μsec., at which time the radial electron density profiles show no significant axial ionization. Ionization on the discharge axis does not become significant until the arrival of the precursor, a microsecond later.

To recapitulate, the important facts which the model must explain are:

1) the development of the precursor
2) the constant velocities of the current and ionization shells
3) the abrupt arrest of these two features, and
4) the low percentage ionization.

VI.3 The Model

This model is put forward to explain the observed dynamics of the Z-pinch discharge in 4 Torr. helium. It consists of a shock wave driven by the collapsing current sheet. The characteristics of the shock front are dictated by the requirement that the kinetic pressure of the shock-heated gas ahead of the current sheet equal the magnetic pressure exerted on the current sheet by Lorentz forces.

The model outlined in the preceding paragraph is capable of explaining the state of dynamic equilibrium which appears in the discharge during the collapse phase, and which is revealed in the constancy of the current and ionization sheet velocities

over much of the collapse. It explains the generation and behaviour of the precursor. The reason for the abrupt halt of the current sheet can be deduced from the model, and it provides an explanation of the "reflection peak" mentioned above.

The shock front which is a leading feature of the model is identified with the leading edge of the "precursor". The "precursor" feature is first observed at r = 4.5 cm. The trajectory of the peak electron density in the "precursor", and of the leading edge of that feature have been plotted in Fig. V-11. The velocity of the front in the lab frame is constant and is measured to be 12 Km./sec.

The sound speed in room temperature helium is 1.0 Km./sec., which gives, for the shock wave, a Mach number, M, of 12. We apply the theory of steady, strong shocks in an ideal gas[18] to calculate the thermo-dynamic properties of the gas behind the shock.

$$\frac{p_2}{p_1} = \frac{2g}{g+1}(M^2-1) \tag{6.1}$$

$$\frac{v_2}{v_1} = \frac{g-1}{g+1} \tag{6.2}$$

$$\frac{T_2}{T_1} = \frac{1}{M^2}\left[1 + \frac{2g}{g+1}(M^2-1)\right]\left[1 + \frac{g-1}{g+1}(M^2-1)\right] \tag{6.3}$$

where p, v and T refer to the gas pressure, mean flow velocity relative to the shock, and temperature, respectively. The subscript 1 refers to conditions ahead of the shock, and the subscript 2, to conditions behind it. The parameter g is the ratio of specific heats, which is 1.67 for an ideal gas. The parameter M, as already defined, is the Mach number.

In our case:

$$p_1 = 4 \text{ Torr.} = 567 \text{ nt./m}^2$$
$$v_1 = 12 \text{ Km./sec.}$$
$$T_1 = 290^{\circ}\text{K.}$$

Application of 6.1, 2 and 3 yields

$$P_2 = 1.0 \times 10^5 \text{ nt./m}^2 = 710 \text{ Torr.}$$
$$V_2 = 3 \text{ Km./sec.}$$
$$T_2 = 13,300^{\circ}\text{K}$$

Calculation of the magnetic pressure, P, on the current sheet during the time interval when that sheet has a constant velocity (from 5.0 μsec. to 7.0 μsec.), gives, for a magnetic field of 0.51 W./m²:

$$P = \frac{B^2}{2\mu_0} = 1.04 \times 10^5 \text{ nt./m}^2.$$

(The magnetic forces per unit volume can be written as grad $(B^2/2\,\mu_0)$ provided that $\underline{j} \times \underline{B}$ is large only in a thin shell. Figure V-17 shows this assumption to be valid).

It is evident that $P = p_2$, so that we impose on the model the requirement that the gas kinetic pressure ahead of the current sheet be balanced by the magnetic pressure acting on it from the rear.

As a result of the cylindrical geometry, we expect that the balance between gas kinetic pressure and magnetic pressure must soon be destroyed, since the gas flow is everywhere radially inward. The flow compresses the gas and increases its pressure. The maximum internal pressure which the current sheet can provide is $B^2/2\,\mu_0$, which is essentially controlled by the discharge circuit. The measurements clearly indicate that the velocity

of the current shell is constant. Hence, gas must be flowing out through the piston, to keep the gas pressure equal to the magnetic pressure.

It is instructive at this point to make an analogy between a shock wave being driven by a leaky piston, and a water wave supported by the movement of a sieve. The viscous drag of the water flowing through the sieve determines the sieve velocity for a given applied force. It also determines the height to which water will pile up ahead of the sieve.

In the Z-pinch, the force is applied on the ions, through the electrons. A constant velocity of the current sheet will be achieved when the "viscous drag" on the ions, from collisions with neutrals, is equal to $\underline{j} \times \underline{B}$, the applied force. Similarly, the viscous drag on the neutrals determines the pressure gradient that will be established. Mathematically,

$$\underline{j} \times \underline{B} = \text{grad } p.$$

It can be seen, however, that the piston is not "leaky" for the electrons whose presence we detect in the precursor. This can be shown, if we assume that the number of ions and electrons between the piston and the shock front is not changed (e.g. by recombination, Joule heating, shock ionization, etc.). Then N_e (precursor) is proportional to $1/V$, where V is the volume occupied by the electrons and ions.

The volume, V, is given by:

$$V = \pi (r_p^2 - r_s^2) \ell \tag{6.5}$$

where r_p is the radius of the cylindrical piston, r_s is the radius of the shock front, and ℓ is the discharge length. If N is the constant number of electrons trapped, then the density, N_e is:

$$N_e = \frac{N}{V} = \frac{N}{\pi(r_p^2 - r_s^2)\ell} \tag{6.6}$$

Let $r = \frac{r_p + r_s}{2}$, where we identify r with the measurement point, then:

$$N_e = \frac{N}{\ell}\frac{1}{4\pi r^2}\frac{1}{(1 - r_s/r_p)} \tag{6.7}$$

Figure VI-1 shows a log-log plot of $N_e \cdot (1 - r_s/r_p)$ versus r. The slope of the straight line drawn in Fig. VI-1 is -1.9, which supports the assertion that there is little leakage of electrons and ions through the current piston, so that the pressure equilibrium in the shock-heated gas is maintained by the leakage of neutrals.

It should be pointed out that the relative velocity of the shock front with respect to the shock heated gas means that the compressing gas, which is observed by monitoring the increase in peak electron density of the precursor, actually lies in a ring whose inner radius is greater than the shock front radius. Thus the value chosen for r_s in equation 6.7 should not be the shock front radius, but some slightly larger number. This will tend to decrease the slope of the graph of Fig. VI-1 towards -2.

The jump in N_e observed <u>at</u> the shock front is attributed to the compression of the small number of electrons already present in this volume. This does not materially affect the value of N (see equation 6.6) as the total number of electrons in a thin shell at r = 1.0 cm. is a factor of 50 less than the total number in a shell of the same density and thickness at r = 7.0 cm.

To review the features of the model thus far elucidated: an equilibrium is established in which the shock-heated gas pressure ahead of a leaky piston exactly balances the magnetic pressure behind it. This model is constructed on the basis of

Fig. VI-I $\quad$ Log $N_e \cdot (1 - r_s/r_p)$ vs. Log r

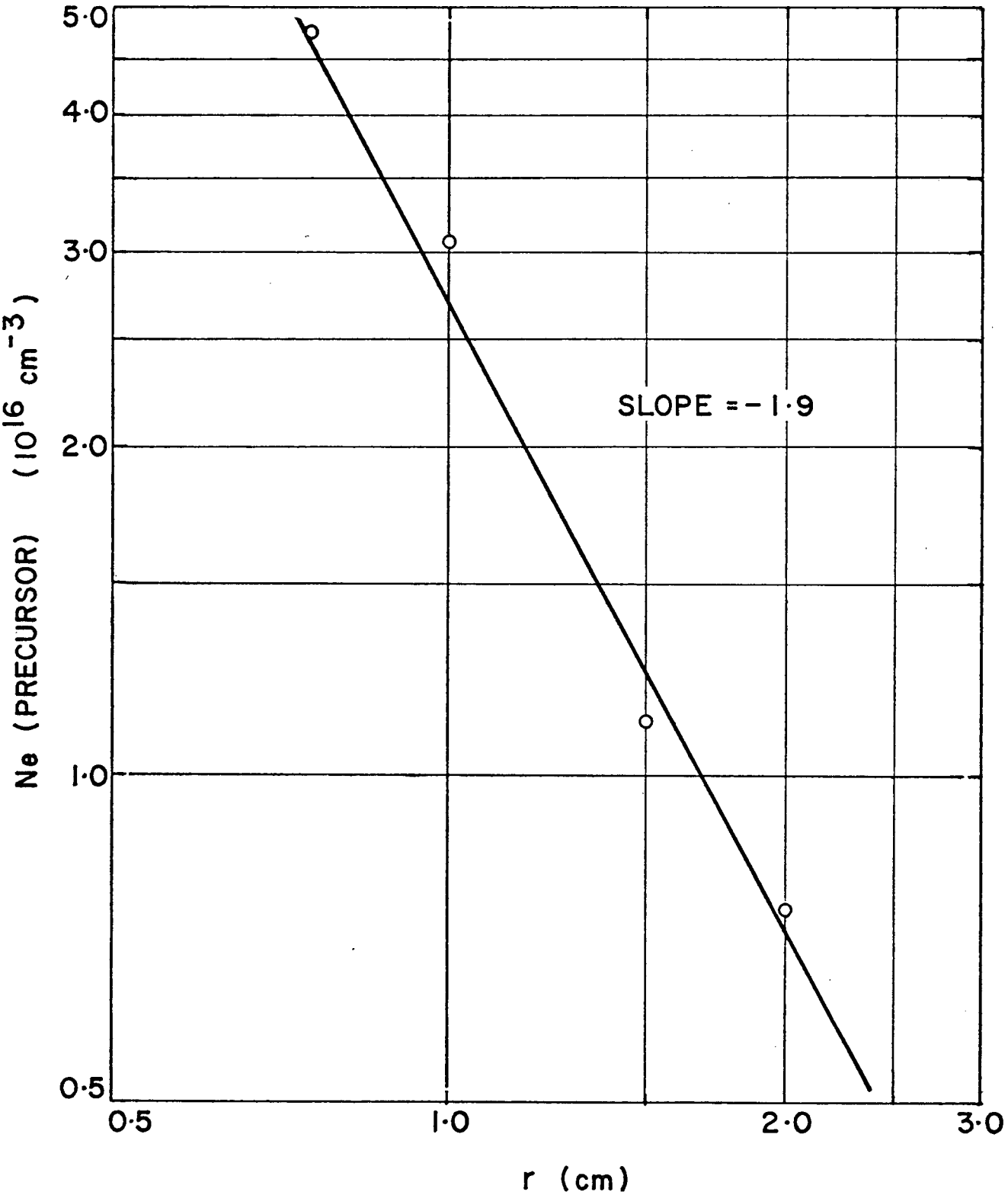
5·0
4·0
3·0
2·0
1·0
0·5
Ne (PRECURSOR) (10^{16} cm^{-3})
SLOPE = − 1·9
0·5
1·0
2·0
3·0
r (cm)

the constant current sheet and shock front velocities, and it is capable of explaining the generation of the precursor.

The state of dynamic equilibrium evidenced during the interval between five and seven microseconds is badly upset, however, during the next microsecond. The maximum $\underline{j} \times \underline{B}$ profile as a function of time (Fig. V-16) shows a substantial drop in the magnetic force in this time interval. The pressure gradient in the shock-heated gas is now greater than $\underline{j} \times \underline{B}$ and the neutral flow out through the piston is increased. This flow increases the viscous drag, which brings the current sheet to an abrupt halt.

The precursor shock carries on to the axis, where it reflects back into the shock-heated gas. This reflected shock cannot be detected between $r = 0$ and $r = 2.5$ cm. because it is moving through hot un-ionized gas. It is a weak shock and cannot produce ionization. (The shock velocity is 13 Km./sec., and the local sound speed 6.7 Km./sec.). For r greater than 2.5 cm. (see Fig. V-11) the reflected shock is moving in partially ionized gas, and the resulting compression can be detected as a jump in electron density. This is the "reflection peak".

The "reflection peak" whose trajectory is plotted in Figure V-11, is a promising diagnostic tool. It is possible to measure the density ratio across the shock, and its velocity in the lab frame. From this data, we may calculate some of the thermodynamic properties of the gas into which the shock is passing.

Since the shock is so weak, it cannot be producing significant ionization. Instead, the jump in N_e across the shock must reflect a compression of the gas as a whole, including the

electronic component, which can be observed. Further, the "main peak" into which the shock is passing has just come to rest, which allows us to equate the front velocity in the lab frame to that in the frame of the gas.

From the conservation equations for a weak shock (g, the ratio of specific heats, constant through the front), we have[17]:

$$\frac{p_1}{p_2} = 1 + \frac{2}{g+1}\,(M^{-2}-1) \tag{6.8}$$

where p_1 and p_2 are the densities of the gas ahead of and behind the shock, respectively, and M is the Mach number, defined as:

$$M = \frac{v}{c}\,. \tag{6.9}$$

The sound speed in the gas into which the shock is moving is c, and v is the front velocity. The value of c at an arbitrary temperature, T, can be related to the known speed of sound, c_o, at some other temperature T_o by:

$$\frac{c}{c_o} = \sqrt{\frac{T}{T_o}} \tag{6.10}$$

Solving 6.10 for c and substituting into 6.9 we get:

$$M = \frac{v}{c_o}\sqrt{\frac{T_o}{T}} \tag{6.11}$$

Substituting 6.11 into 6.8 and solving for T, we get:

$$T = T_o\left(\frac{v}{c_o}\right)^2\left[1 + \left(\frac{p_1}{p_2} - 1\right)\frac{g+1}{2}\right] \tag{6.12}$$

We choose $T_o = 290^{\circ}$K. and $c_o = 1.0$ Km./sec. Measurement of Fig. V-11, gives v = 13 Km./sec., and Fig. V-5 gives $p_1/p_2 = 0.7$. The gas is definitely ionized at this point and g is not 5/3.

However, substitution of $g = 5/3$ into 6.12 gives $T = 28{,}000^{\circ}K$, while setting $g = 1.1$ only raises the value of T to $33{,}000^{\circ}K$. Comparison with calculated values of g for a hot helium plasma[17] shows that for any temperature in excess of $16{,}000^{\circ}K$, g has a value between 1.1 and 1.2. In this way we estimate the temperature of the gas into which the shock is passing is $32{,}000^{\circ}K$.

This value is substantially higher than the gas temperature behind the imploding shock. However, the gas whose temperature has just been measured at $32{,}000^{\circ}K$ has been brought to rest from a radial velocity of 6-7 Km./sec. and the thermalization of this kinetic energy is thought to be responsible for the elevated temperature.

VII Conclusions

VII.1 Introduction

This chapter begins with a brief resumé of the important improvements made in the design of laser-excited Fabry-Perot interferometers for plasma diagnostics which have been made in the course of this experiment. Some suggestions are included for ways in which the device may be further improved.

The chapter closes with a brief review of the important observations which have been made on the collapse of a Z-pinch in 4 Torr. helium with the interferometer, and includes some remarks on the direction which future research could take.

VII.2 A Summary of Resonator Improvements

When the work which this thesis describes was begun, it was apparent, that in order to be able to elucidate the plasma characteristics in the Z-pinch collapse, a means of measuring electron density had to be developed which had a high frequency response, high temporal resolution, high sensitivity, and which was not too difficult to operate. Such a device is now available as a result of this work.

The starting point for the device was a conventional laser-excited Fabry-Perot interferometer. An analysis of the shortcomings of such an instrument was made, and work was begun to overcome them.

The first problem overcome was the problem of interferometry in the presence of transverse gradients in electron density. The use of quartz tubes to reduce the plasma length, pioneered by S. Medley[2], was adopted. The resonator geometry was modified from the unstable planoconcave to the stable

concentric form[22]. This improvement not only reduced the effect of the transverse gradients, but made alignment easier and improved beam overlap.

Next, the techniques of fractional fringe shift interferometry in the time domain were applied to the problem of measuring electron densities. The interferometer which included this improvement had a sensitivity and temporal resolution an order of magnitude better than the conventional interferometer at times when the electron density was rapidly varying, and several orders of magnitude better where the electron density was slowly varying or varying rapidly by small amounts. This improvement also permitted a unique determination of the sign of the change in optical path length to be made.

Finally, electronic circuitry was developed to enable the user of the interferometer to display directly on an oscilloscope the instantaneous value of the electron density.

Comparison of the modified, laser-excited Fabry-Perot interferometer, including the improvements discussed above, with competitive techniques for measuring electron densities in plasmas is instructive. The best competitive method is the technique of measuring line-broadening. In order to make line-broadening measurements, a very expensive, high dispersion spectrometer is required. For application to a pulsed, non-reproducible discharge, a multi-channel detection system would be essential. In spite of all this expensive equipment, the data analysis would be difficult and subject to many uncertainties (i.e. spatial inhomogeneities, nature of broadening mechanism). In the end, the system depends on measuring very small changes in the width of a line of probably uncertain shape.

The interferometric system, on the other hand, is simple, direct, and most important, provides a continuous and direct recording of the electron density. No integration over a number of shots is required, and only a minimum of analysis is necessary to get out the results.

As a final comparison of the two techniques, let it be noted that the reflected shock, which is measured with sufficient accuracy to allow its use as a diagnostic probe of the plasma, would never have been detected in a line-broadening measurement.

The laser interferometer is now a very accurate, high frequency, and straight-forward way of measuring the rapid changes in electron density observed in the collapse phase of a Z-pinch.

A further improvement of the system would be achieved if the output frequency of the resonator due to the rotating quartz block could be measured at all times, instead of being approximated electronically as at present. A second resonator, including the quartz block but not the plasma could achieve this. The second resonator would feed a second IFMD. Direct subtraction of the outputs of the two IFMD's would then provide exact correction for the instantaneous value of f_o, thus realizing the full accuracy of fractional fringe shift interferometry in the time domain. The same effect could be achieved by using the output of the plasma-free resonator to determine the magnitude of the current fed onto the IFMD integrating capacitor.

VII.3 Observation of the Z-Pinch

The claims for the improvement of the resonator have been substantiated in the course of measurements made for that purpose on the Z-pinch in 4 Torr. helium. This particular discharge was chosen because of its potential as a spectroscopic source, and because several other workers had observed peculiarities in the dynamics of the discharge which had not been noted in other discharges.

The abrupt arrest of the current sheet had been reported by Tam[20], and the separation of the current sheet and the ionization region was also reported, but no really good measurements on the collapsing ionization shell had been made.

We have observed the separation of current sheet and ionization sheet, and the halting of both some distance off axis. We have also observed a precursor shock front and the reflection of this shock off the axis and back out into the plasma. From the observed dynamics of the discharge the following model of the collapse process has been developed:

1) The current sheet acts as a leaky piston to drive a shock wave.
2) The resulting configuration is an equilibrium one, with neutral gas flow through the piston to maintain equilibrium pressure and density ahead of the piston in the cylindrical collapse.
3) The equilibrium configuration is established through the mechanism of ion-neutral "viscous drag". The $\underline{j} \times \underline{B}$ force on the ions balances the ion-neutral viscous drag. The neutral-ion viscous drag sustains the pressure gradient which drives the shock.

4) The current sheet comes to rest when the magnetic pressure declines and is no longer sufficient to balance the pressure gradient in the shock-heated gas.
5) The driven shock wave reflects from the axis. Passing through the ionized gas, it shows a temperature of 32,000^{o}K.

Observations of the ionization shell show less than 60% ionization if the total density in the shell is only equal to the filling density. It is possible that this ionization represents only a remnant of the original ionization produced by Joule heating at the walls, which has been swept up by the trailing edge of the magnetic field. Alternatively this ionization is due to an ionization mechanism coupled to the neutrals leaking out of the current piston. This cannot be decided from the data at hand and should be the object of further study.

Another object of further study should be the distribution of neutral atoms through the plasma. As has been discussed, the flow of neutral atoms determines the equilibrium attained between the current sheet and the shock-heated gas. One way in which the neutral distribution could be determined would be to measure the change in index of refraction of the plasma at two different wavelengths. The difference between the two measurements will give an indication of the effect of neutrals. The method discussed above is not very sensitive, and perhaps other superior methods could be found.

Finally, these measurements confirm the suitability of a Z-pinch as a spectroscopic source. The presence of a relatively quiescent plasma of 32,000^{o}K. provides a source for the

calibration of line-broadening measurements, particularly as the electron density and temperature are independently known. This provides an interesting prospect for future work. It would be of interest to see if variation of the initial filling pressure in the discharge vessel could be used to vary the temperature and density of this stable plasma.

Work has been done by Roberts[23] with a view to substantiating the Z-pinch as a spectroscopic source. He measured electron densities in a Z-pinch using laser interferometry, but in his case the resonator was aligned normally to the discharge axis. This necessitated Abel unfolding of the resulting fringe patterns, to find the electron density distribution. This is clearly less satisfactory than the present technique. Further, he did not utilize the techniques of fractional fringe shift interferometry in the time domain, and the accuracy of his measurements is correspondingly less.

BIBLIOGRAPHY

1. Medley, S.S., Curzon, F.L. and Daughney, C.C., Rev. Sci. Instr. 36, 713 (1965)

2. Medley, S.S., J. Appl. Physics 41, 142 (1970)

3. Curzon, F.L., Pachner, J. Jr., and Tam, Y.K.S., Can. J. Phys. 48, 1370 (1970)

4. Williamson, J.H. and Medley, S.S., Can. J. Phys. 47, 515 (1969)

5. Dangor, A.E. and Fielding, S.J., J. Phys. D. Appl. Phys. 3, 413 (1970)

6. Jahoda, F.C., et al. Appl. Opt. 6, 8 (1967)

7. Baker, D.A., Hammel, J.E. and Jahoda, F.C., Rev. Sci. Instr. 36, 395 (1965)

8. Sawyer, G.A., Finlayson, V.A., Jahoda, F.C. and Thomas, K.S., Phys. Fluids 10, 1564 (1967)

9. Herold, H. and Jahoda, F.C., Rev. Sci. Instr. 40, 145 (1969)

10. Thomas, K.S., Phys. Fluids 11, 1125 (1968)

11. Kricker, W.A. and Smith, W.I.B., Phys. Lett. 14, 102 (1965)

12. Witteman, W.J., Appl. Phys. Lett. 10, 347 (1967)

13. Gibson, A. and Reid, G.W., Appl. Phys. Lett. 5, 195 (1964)

14. Holt, E.H. and Haskell, R.E., 1965. Foundations of Plasma Dynamics (The Macmillan Company, New York).

15. Gerardo, J.B., Verdeyen, J.T. and Gusinow, M.A. J. Appl. Phys. 36, 2146 (1965)

16. Bolwejn, P.T., Peek, Th. H. and Alkemade, C. Th. J., Phys. Lett. 23, 88 (1966).

17. Ahlborn, B. and Salvat, M., Z. Fur Naturf. 22, 260 (1967).

18. Oswatitsch, K. 1956, Gas Dynamics (Academic Press, Inc., New York).

19. Dimoff, K. and Tam, Y.K.S., Can. J. Physics 48, 884 (1970).

20. Tam, Y.K.S., (1967) Doctoral Thesis, University of British Columbia.

21. Ashby, D.E.T.F. and Jephcott, D.F., J. Appl. Phys. 36 29 (1965).

22. Kogelnik, H. and Li, T., Appl. Opt. 5, 1550 (1966).

23. Roberts, T.E. (private communication). Submitted to Phys. Fluids for publication.

24. Griem, H.R. 1964. Plasma Spectroscopy (McGraw-Hill Book Company, New York).

25. Fork, R. L. and Bradley, L.C., Appl. Opt. 3, 137 (1964).

26. Rowley, P.D., Rev. Sci. Inst. 41, 313 (1970).

Appendix I - The Integrating Frequency Modulation Detector

The operating principles of the I.F.M.D. are found in Chapter IV.4, so they will not be elaborated upon here. Figure AI-1 shows the complete circuit diagram of the device.

Calibration

Calibration of the I.F.M.D. output in terms of N_e/V, or the number of electrons per cubic centimetre per volt of deflection, involves the determining of two constants in equation 4.26. These constants are C_1 and Z, where Z is the length of plasma which is being observed, and where C_1 depends on the amount of charge being removed from the integrator for each zero-crossing of the resonator output. The constant Z is equal to the quartz tube separation and is easily measured.

The value of C_1 is determined using equation 4.24, which is:

$$V(t_2) - V(t_1) \equiv \Delta V = C_1 \int_{t_1}^{t_2} (f_b(\tau) - f(\tau))\,d\tau \qquad (4.24)$$

where f_b, you will recall, is the constant base frequency at which I.F.M.D. is balanced. Consider the effect if $f(\tau)$ is replaced by a known constant frequency, f_1.

$$\Delta V_1 = C_1 \int_{t_1}^{t_2} f_b(\tau)\,d\tau - C_1 \int_{t_1}^{t_2} f_1(\tau)\,d\tau$$

$$= C_1 (f_b - f_1)(t_2 - t_1) \qquad (AI.1)$$

If a second, also known frequency, f_2, is now provided:

$$\Delta V_2 = C_1 (f_b - f_2)(t_2 - t_1) \qquad (AI.2)$$

In both cases, the voltage outputs are straight lines of constant slope.

If $S_1 = \Delta V_1/(t_2 - t_1)$ and $S_2 = \Delta V_2\ (t_2 - t_1)$, then;

$$S_1 - S_2 = C_1\ (f_b - f_1) - C_1\ (f_b - f_2) = C_1\ (f_2 - f_1) \qquad \text{(AI.3)}$$

If S_1 and S_2 are measured, C_1 is easily calculated from the known difference $f_2 - f_1$.

Figure AI-1 Integrating Frequency Modulation Detector Circuit Diagram

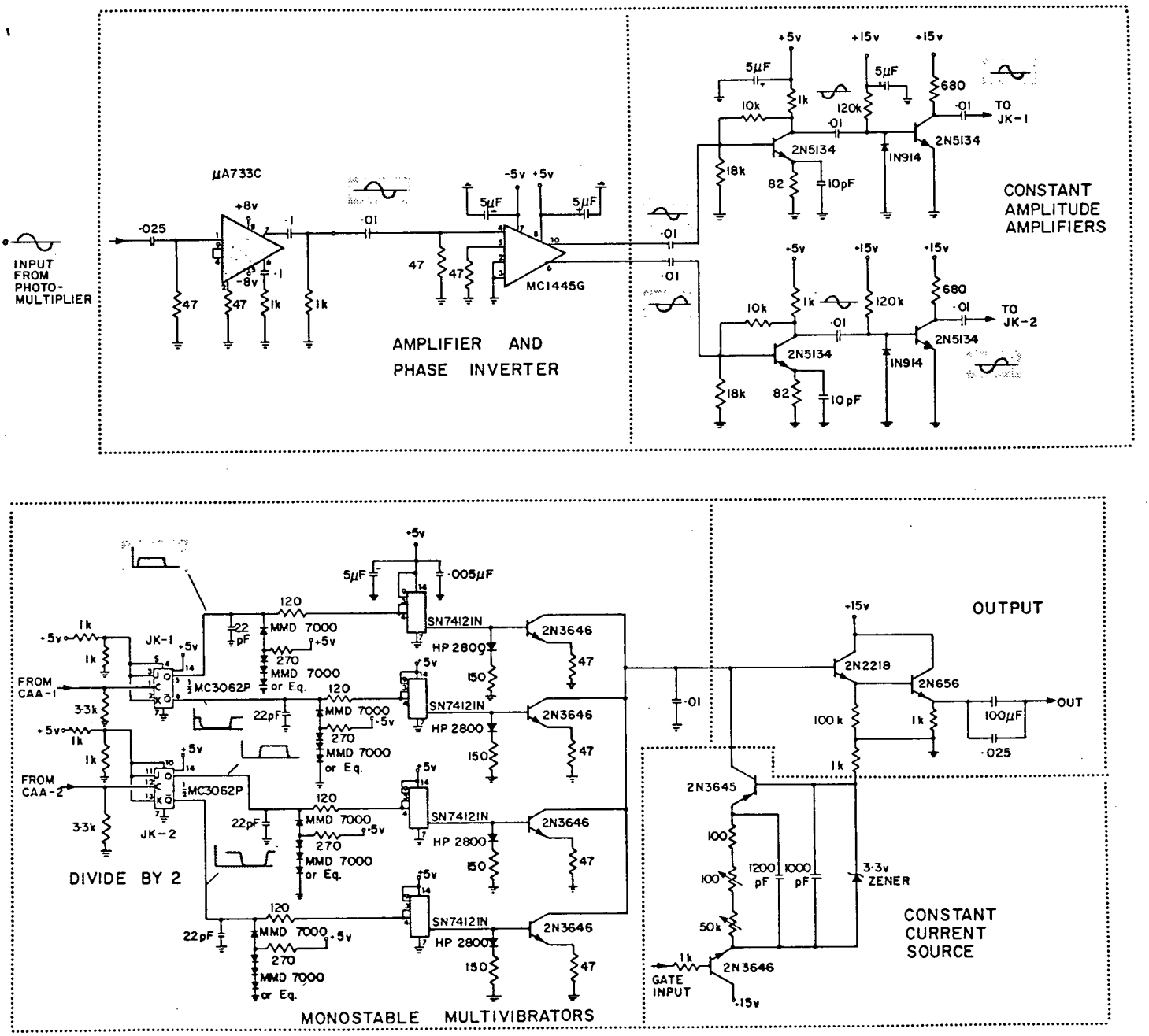

Appendix II - The Interval Recognition Detector

The basic functions of the IRD are given in Chapter V.3. The complete circuit diagram of the device is given in Figure AII-1.

Figure AII-1 Interval Recognition Detector Circuit Diagram

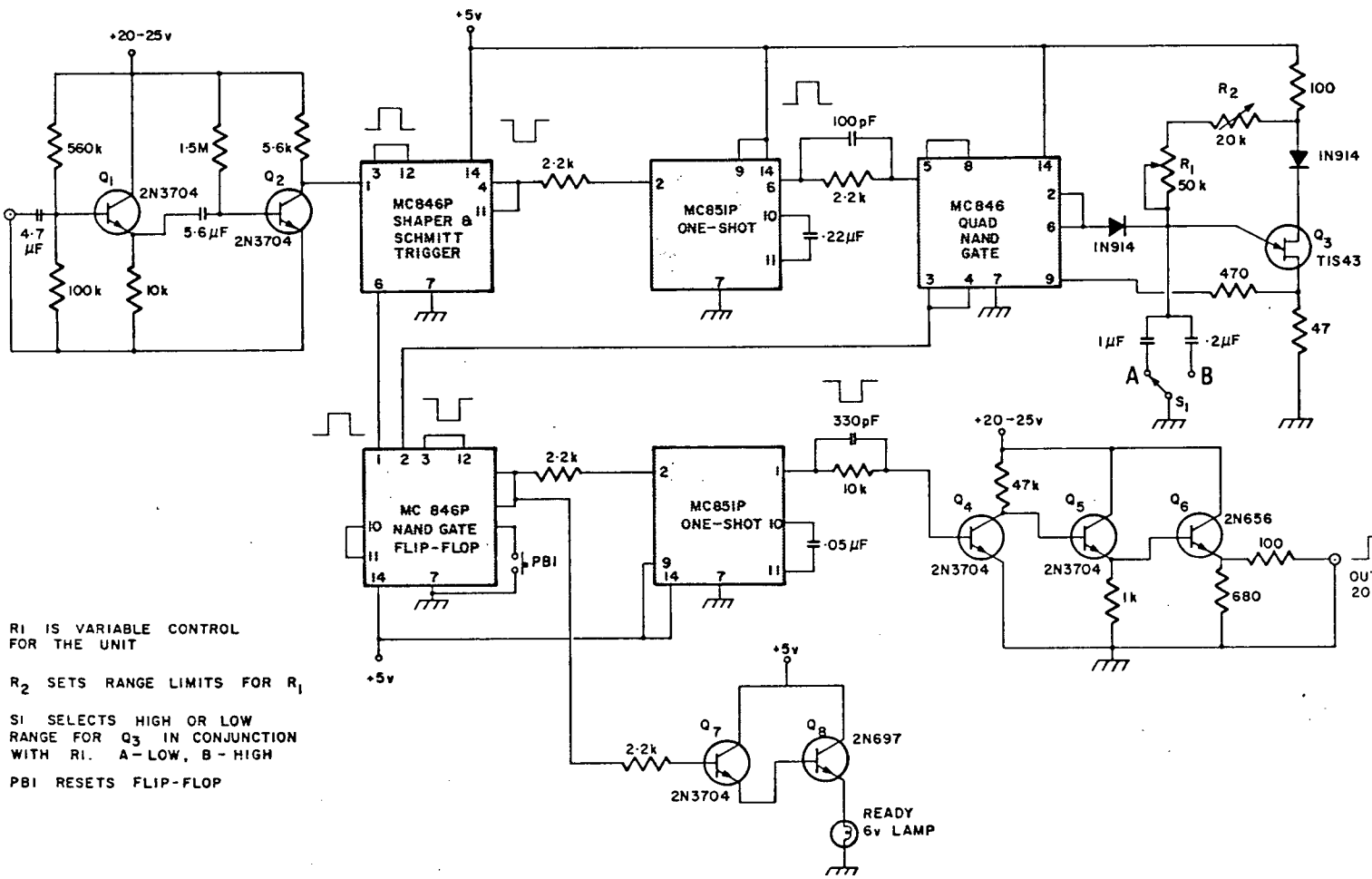

page 126 [illegible]

Appendix III - HeI Transitions and the Refractive Index

The plasma refractive index is given by[24]:

$$n-1 = \frac{-e^2}{2\varepsilon_o M_e} \sum_i \frac{N_i f_i}{(\omega^2-\omega_i^2)} \qquad \text{AIII.1}$$

where n is the refractive index, e is the electronic charge, M_e is the electronic mass, ω_i is the frequency of a radiative transition, N_i is the density of atoms in the ground state of the transition, f_i is the transition oscillator strength, and ω is the frequency of the laser radiation.

The plasma frequency (ω_p) is:

$$\omega_p^2 = \frac{e^2 N_e}{\varepsilon_o M_e} \qquad \text{AIII.2}$$

where N_e is the electron density. Substituting AIII.2 into AIII.1, we get:

$$n-1 = -\frac{1}{2} \sum_i \frac{\omega_p^2}{(\omega^2-\omega_i^2)} f_i \frac{N_i}{N_e} \qquad \text{AIII.3}$$

Since $\omega \approx \omega_i$,

$$\omega^2 - \omega_i^2 \approx 2\omega(\omega - \omega_i) \qquad \text{AIII.4}$$

which, on substitution into AIII.3, gives:

$$n - 1 = -\frac{1}{2} \sum_i \frac{\omega_p^2}{2\omega^2} \frac{\omega f_i}{\omega-\omega_i} \cdot \frac{N_i}{N_e} \qquad \text{AIII.5}$$

But $-\frac{\omega_p^2}{2\omega^2}$ is the contribution to the change in refractive index due to the electrons, which allows us to write:

$$(n-1)_{total} = \frac{1}{2}\,(n-1)_e \sum_i \frac{\omega f_i}{\omega-\omega_i}\,\frac{N_i}{N_e} \qquad \text{AIII.6}$$

Letting α_i be the ratio of the refractive index change due to the ith transition to that due to the electrons, we have

$$\alpha_i = \frac{1}{2}\,\frac{\omega f_i}{\omega-\omega_i}\,\frac{N_i}{N_e} \qquad \text{AIII.7}$$

It is now necessary to evaluate α_i for all HeI transitions (HeII transitions have been ignored because of the very high temperature required to excite them). A list of HeI transitions which have both large values of f_i and small values of $\omega-\omega_i$ is found in Table AI, which includes the value of $\frac{\omega f_i}{\omega-\omega_i}$ for each of these (from Griem[24], p. 363). Notice that the two lines with largest f_i are also those which are closest to 6328Å, the lasing transition. They dominate the refractive index contribution of the transitions of HeI.

The energies associated with the 2^1P level, the 2^3P level and the first ionization potential are 21.13 eV., 20.87 eV. and 24.46 eV., respectively. These three excited states are sufficiently close together that P.L.T.E may be considered to exist among them. Applying Saha's equation to the 2^3P and ionized states, we find:

$$\frac{N_e N_+}{N_3} = \frac{2g_+}{g_3}\left(\frac{2\pi m_e kT_e}{h^2}\right)^{3/2} e^{-(E_+-E_3)/kT_e} \qquad \text{AIII.8}$$

where N_+ is the ion density (equal to the electron density), N_3 is the density of atoms in the 2^3P state, g_+ ($g_+ = 2$) is the

TABLE AI

Transition	λ (Å)	f_i	$\frac{\omega f_i}{\omega - \omega_i}$
$2^1S - 3^1P$	5,015.7	0.17	-0.82
$2^1P - 3^1D$	6,678.1	0.73	13.2
$2^1P - 4^1D$	4,921.9	0.12	-0.54
$2^3P - 3^3D$	5,875.6	0.62	-8.6
$2^3P - 4^3D$	4,471.5	0.12	-0.41

statistical weight of the ionized state and g_3 ($g_3 = 9$) that of the 2^3P state, h is Planck's constant, k is Boltzmann's constant and $(E_+ - E_3)$ is the energy difference between the two states, giving:

$$\frac{N_3}{N_e^2} = 6.97 \times 10^{-21} \frac{e^{3.59/kT_e}}{(kT_e)^{3/2}} \qquad \text{AIII.9}$$

where kT_e is now expressed in eV., and the densities are measured in cm^{-3}.

The temperature of the plasma is not likely to be sufficient to produce L.T.E. between the 2^3P and ground states, which will tend to produce an overpopulation of the ground state relative to the 2^3P state. In this event:

$$N_3 < N_o \frac{g_3}{g_o} e^{-E_3/kT_e} \qquad \text{AIII.10}$$

where N_o and g_o are the density and statistical weight, respectively, of the ground state.

Combining AIII.10 with AIII.9, we get:

$$\left(\frac{N_3}{N_e}\right)^2 < 6.97 \times 10^{-21} \frac{g_3 N_o}{g_o} \frac{e^{-17.28/kT_e}}{(kT_e)^{3/2}} \qquad \text{AIII.11}$$

The function

$$\frac{e^{-17.28/kT_e}}{(kT_e)^{3/2}}$$

has a maximum value of 5.71×10^{-3} for:

$$kT_e = 11.5 \text{ eV.}$$

Thus,

$$\left(\frac{N_3}{N_e}\right)^2 < 3.98 \times 10^{-23} \frac{g_3 N_o}{g_o} \qquad \text{AIII.12}$$

For a filling pressure of 4 Torr., and a neutral compression ratio of four, we get, as the maximum value of N_o,

$$N_o < 4.8 \times 10^{17}\ cm^{-3}$$

Since $g_3 = 9$, $\frac{g_3}{g_o} < 10$, which gives

$$\frac{N_3}{N_e} < 4.4 \times 10^{-3} \qquad \text{AIII.13}$$

Thus, for the $2^3P - 3^3D$ transition,

$$\alpha_3 < 1.89 \times 10^{-2} \qquad \text{AIII.14}$$

A factor of three reduction in the statistical weight, partially offset by an increase in $\frac{\omega f_i}{\omega - \omega_i}$ of less than a factor of two, gives an α for the $2^1P - 3^1D$ transition which is about one half of that given in AIII.14.

Thus the maximum possible contribution of HeI transitions to the change in plasma refractive index is less than 2%. This "worst case" presumes an electron temperature at least a factor of five higher than is likely to exist in the Z-pinch, and the actual contribution is therefore so small as to be entirely negligible.